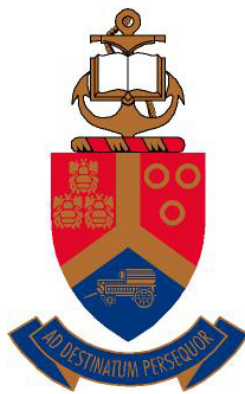


# Synthesis and characterization of transparent conducting oxides for Stark effect applications in single molecule spectroscopy

by

Abraham Johannes Cronje



Submitted in partial fulfilment of the requirements for the degree

Magister Scientiae

In the Faculty of Natural and Agricultural Science

Department of Physics

**University of Pretoria**

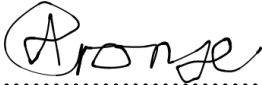
Supervisor: Professor M. Diale

Co-Supervisor: Professor T. Krüger

29 September 2019

## Declaration of Authorship

I, Abraham Johannes Cronje declare that this dissertation, which I hereby submit for the degree Magister Scientiae in Physics at the University of Pretoria, is my own work and has not been previously submitted by me for a degree at this or any other tertiary institution.

Signature:.....

Date:..... 2020-02-12

## Acknowledgements

### My sincere thanks to:

- Prof. Diale for her unwavering support, constant availability, understanding attitude, guidance in the project and her aid and advice in academic, personal and financial matters.
- Prof Krüger for including me in the Biophysics Research Group, all the advice and inspiration a student could need, and for caring so much about his job.
- My parents for always doing as much as possible for their children, no thanks could ever be enough.
- My fellow postgraduate students for their continuous support and their enthusiasm in helping me. In particular I would like to thank Mustafa, Shadrach and Ben for all the discussions and help throughout my Master's.
- The National Research Foundation (NRF) of South Africa for making this research project possible with their financial assistance.
- The University of Pretoria for a memorable student experience.

## Summary

The desire to study the characteristics of transparent conducting oxides (TCOs) for Stark application in single molecule spectroscopy (SMS) stemmed from our interest in the dark states of light harvesting complex II (LHCII) of plants. Investigation of this mechanism requires a Stark cell. The high optical quality required by the SMS procedure demands a very specific thickness microscope slide at the objective to sample interface. Since no commercial TCOs of this standard were available, we had to synthesize our own and spin-coat our SMS setup's stock microscope slides.

As a first attempt, fluorine doped tin oxide (FTO) thin films were synthesized at 0 to 3 percent atomic doping levels. The optical quality of the films were low, as they appeared almost burned (blackish). X-ray diffraction (XRD) confirmed the films to be FTO by the FTO powder diffraction file (PDF 00-041-1445). The average optical band gap achieved was 3.860 eV, in good agreement to literature. A minimum resistivity of  $0.37 \Omega.cm^{-1}$  was obtained for the 2% sample. Scanning electron microscopy revealed that the poor optical quality of the films was due to agglomeration of tin, most likely due to a too high tin concentration in the solution.

Due to availability and experience in the department with zinc oxide thin films, the following study was on the synthesis of aluminium doped zinc oxide (AZO). Thin films of atomic doping percentages ranging from 0 to 5 percent in steps of 1 percent were fabricated. A new deposition of layer procedure was also used, described in the next paragraph. AZO was successfully synthesized, confirmed by XRD correspondence to zinc oxide's PDF (00-036-1451) and the average optical band gap of 3.2873 eV agreement to literature. SEM revealed polycrystalline morphology in all films. All films had high transparency in the

visible, as showcased by ultraviolet to visible (UV-Vis) spectroscopy. A minimum resistivity of  $8.61 \Omega.cm^{-1}$  was obtained for the 2% sample.

From experience gained in the FTO study, we hypothesized that a different *Deposition of thin film layer* technique could have a significant impact on the quality of TCO films. Simply drying a layer before addition of a new layer would not solidify the layer in a significant way. Addition of new solution would then solubilize a good amount of dried particles of the previous layers. This would result in a new pseudo-solution of much higher concentration, resulting in aggregation and low reproducibility. Our results indicated that the *Deposition of thin film layer* technique had little impact on the optical quality of the films, however, the crystalline and electrical qualities were both significantly better for TCO application. This procedure was used for the AZO study.



# Contents

Introduction . . . . .	16
<b>1 Single Molecule Spectroscopy and Stark Effect</b>	<b>21</b>
1.1 Introduction . . . . .	21
1.2 Single Molecule Spectroscopy . . . . .	22
1.3 Stark Effect . . . . .	32
<b>2 Semiconductors</b>	<b>35</b>
2.1 Band Structure . . . . .	36
2.1.1 Drude Model . . . . .	36
2.1.2 Drude-Sommerfeld Model . . . . .	38
2.1.3 Nearly-Free Electron Model . . . . .	41
2.1.4 Tight-Binding Model . . . . .	43
2.2 Intrinsic and Extrinsic Semiconductors . . . . .	45
2.3 Fermi Level . . . . .	46
2.4 Defects . . . . .	48
2.4.1 Point Defects . . . . .	48
2.5 Doping . . . . .	50
<b>3 Transparent Conducting Oxides</b>	<b>53</b>

3.1	Introduction . . . . .	53
3.2	Optical Properties . . . . .	54
3.3	Electrical Properties . . . . .	56
3.4	Figure of Merit . . . . .	57
3.5	Tin Oxide . . . . .	58
3.5.1	Introduction . . . . .	58
3.5.2	Defects in SnO <sub>2</sub> . . . . .	59
3.5.3	Doping . . . . .	61
3.6	Zinc Oxide . . . . .	63
3.6.1	Introduction . . . . .	63
3.6.2	Defects in ZnO . . . . .	65
3.6.3	Doping . . . . .	67
<b>4</b>	<b>Experimental Work</b>	<b>69</b>
4.1	Synthesis of Fluorine-doped Tin Oxide . . . . .	69
4.1.1	Solution Preparation . . . . .	69
4.1.2	Substrate Cleaning . . . . .	70
4.1.3	Deposition of thin film layers . . . . .	70
4.2	Synthesis of Zinc Oxide . . . . .	71
4.2.1	Solution Preparation . . . . .	71
4.2.2	Substrate Cleaning . . . . .	72
4.2.3	Deposition of thin film layers . . . . .	72
4.3	Measurement Techniques . . . . .	73
4.3.1	X-ray Diffraction . . . . .	74
4.3.2	Four Point Probe . . . . .	76
4.3.3	UV-Vis Spectroscopy . . . . .	77



<i>CONTENTS</i>	9
4.3.4 Scanning Electron Microscopy . . . . .	79
<b>5 Results and Discussion</b>	<b>83</b>
5.1 Opto-Electronic Properties of Fluorine Doped Tin Oxide . . . . .	83
5.1.1 X-ray Diffraction . . . . .	83
5.1.2 Scanning Electron Microscopy . . . . .	86
5.1.3 Ultraviolet to Visible Spectroscopy . . . . .	87
5.1.4 Four Point Probe . . . . .	92
5.1.5 Conclusion . . . . .	93
5.2 Opto-Electronic Properties of Aluminium Doped Zinc Oxide . . . . .	94
5.2.1 X-ray Diffraction . . . . .	94
5.2.2 Scanning Electron Microscopy . . . . .	100
5.2.3 Ultraviolet to Visible Spectroscopy . . . . .	103
5.2.4 Four Point Probe . . . . .	105
5.2.5 Conclusion . . . . .	107
5.3 Deposition of Layer Procedure Effect on Zinc Oxide . . . . .	108
5.3.1 X-ray Diffraction . . . . .	108
5.3.2 Scanning Electron Microscopy . . . . .	110
5.3.3 Ultraviolet to Visible Spectroscopy . . . . .	112
5.3.4 Four Point Probe . . . . .	114
5.3.5 Conclusion . . . . .	115
<b>6 Conclusion</b>	<b>117</b>
<b>Appendix</b>	<b>121</b>
<b>Bibliography</b>	<b>125</b>



# List of Figures

1	Growth rate of World GDP, population, $CO_2$ emission, oil consumption and oil production as a function of time [1]. . . . .	16
2	Distribution of energy production for the year 2017 [2]. . . . .	17
1.1	Illustration of the Single Molecule Spectroscopy setup that was to be used, showing the internal workings of the technique [3]. . . . .	22
1.2	A supercontinuum spectrum that has been generated from an 800 nm laser pump in water [4]. . . . .	23
1.3	Two dimensional intensity pattern of light diffracted by a small circular aperture. The top right inset shows the different order maxima and minima with the Airy disk (first order maximum) in the center [5]. . . . .	25
1.4	Migration of holes and electrons across the p-n junction causing formation of a space-charge region (depletion region). . . . .	29
1.5	For a grating with facets separated by distance $d$ , the path length difference between two rays hitting subsequent facets are given by $d\sin\theta_i - d\sin\theta_d$ [6].	31
1.6	An atom in the presence of an applied electric field. . . . .	32
1.7	The splitting of helium transition at $438.8nm$ due to the Stark effect [7]. . . . .	33
2.1	Classification of a material as a conductor, semiconductor or insulator based on its band gap. . . . .	35

2.2	The energy of an electron as a function of its wave vector, the relation giving by $E = \frac{\hbar^2 k^2}{2m}$ . . . . .	39
2.3	The energy dispersion of a periodic lattice with period reciprocal lattice vectors $G$ , known as the repeated zone representation. . . . .	42
2.4	On the right are the bands that form due to energy dispersion relationships at the Brillouin zone center and one reciprocal lattice point away. The left image is without the effect of the small potential. . . . .	43
2.5	The atomic orbitals, $\psi_1$ and $\psi_2$ , of electrons tightly bound to ionic cores in their bonding and antibonding states [8]. . . . .	44
2.6	Energy of different electron states for increasing interatomic spacing, band overlap of bands for $3s$ and $3p$ orbitals at interatomic spacing $r_o$ , when it is reduced to $r'$ , there is band overlap for the $2s$ and $2p$ orbitals as well [9]. . . . .	45
2.7	On the left is the Fermi-Dirac distribution function and on the right the Fermi level in the band gap at states $T = 0$ K and $T > 0$ K . . . . .	47
2.8	Showcase of the appearance of different defects in a crystal lattice. . . . .	49
3.1	The optical band gap will increase with what is known as the Burstein-Moss shift as the Fermi level moves into the conduction band [10]. . . . .	55
3.2	The rutile structure where, in this case, tin is denoted by the gray circles and oxygen the red ones. . . . .	58
3.3	Formation energies of the different intrinsic defects in tin oxide as a function of the Fermi energy [11]. . . . .	60
3.4	The wurtzite crystal structure that zinc oxide exhibits, here yellow is depicting oxygen ions and gray zinc ions. . . . .	63
3.5	Formation energies of intrinsic defects in zinc oxide as a function of the Fermi level in <i>a)</i> a zinc rich and <i>b)</i> an oxygen rich growth environment [12].	66

<i>LIST OF FIGURES</i>	13
4.1 Representation of the four point probe setup. [13] . . . . .	76
4.2 Diagram of the ultraviolet to visible setup. . . . .	78
4.3 Diagram of the teardrop shaped interaction volume in SEM [14]. . . . .	80
4.4 Small cuttings of samples immobilized on metallic plates with conductive sticky tape in (a) surface imaging and (b) cross-sectional imaging configurations . . . . .	82
5.1 XRD of tin oxide at different doping levels, with the standard PDF of tin oxide (00-041-1445) at the bottom. The heights of the PDF peaks indicate the relative intensity . . . . .	84
5.2 SEM micrographs of 1% fluorine doped tin oxide at (a) $10\mu m$ and (b) $2\mu m$ scale. . . . .	86
5.3 SEM micrographs of tin oxide for the (a) undoped (b) 2% and (c) 3% doped samples at micrometer scale) . . . . .	88
5.4 SEM micrographs of tin oxide for the (a) undoped (b) 2% and (c) 3% doped samples at nanometer scale. . . . .	89
5.5 UV-Vis spectroscopy of tin oxide at different fluorine doping percentages( <i>at%</i> )	90
5.6 Tauc plots of tin oxide at 2% and 3% fluorine doping percentages . . . . .	91
5.7 Tauc plots of tin oxide at 0% and 1% fluorine doping percentages . . . . .	91
5.8 Four point probe of tin oxide at different doping levels . . . . .	92
5.9 XRD of zinc oxide at different atomic aluminium doping percentages, with the standard PDF peaks of zinc oxide included at the bottom. . . . .	95
5.10 XRD of pure zinc oxide, with the standard PDF peaks of zinc oxide included at the bottom. . . . .	96
5.11 Prominent peaks of XRD of zinc oxide at different doping levels . . . . .	97

5.12	Full width half maximum (FWHM) of the prominent peak [002] of zinc oxide at different doping levels . . . . .	99
5.13	Cross-section images of the (a) undoped, (b) 1% doped, (c) 3% doped and(d) 4% doped samples . . . . .	101
5.14	SEM micrographs of zinc oxide for the (a)undoped, (b)1% doped, (c) 2% doped, (d) 3% doped, (e) 4% doped and (f) 5% doped samples . . . . .	102
5.15	UV-Vis spectroscopy of zinc oxide at different aluminium doping percentages( <i>at%</i> )	103
5.16	Tauc plot of zinc oxide at different aluminium doping percentages( <i>at%</i> ) . .	104
5.17	Resistivity of zinc oxide at different aluminium doping percentages( <i>at%</i> ) .	106
5.18	Xrd of zinc oxide for samples made with the (a) procedure 1 and (b) procedure 2. . . . .	108
5.19	XRD of the prominent peaks for samples prepared with (a) <i>procedure 1</i> and (b) <i>procedure 2</i> . . . . .	109
5.20	SEM micrographs of samples obtained with the (a-c) procedure 1 and (d-f) procedure 2. . . . .	111
5.21	UV-Vis spectroscopy of zinc oxide at different aluminium doping percentages( <i>at%</i> )	112
5.22	Tauc plots of zinc oxide at different aluminium doping percentages( <i>at%</i> ) .	113

# List of Tables

5.1	XRD data of tin oxide at different doping percentages . . . . .	85
5.2	XRD characteristics of the [002] prominent peak of zinc oxide at different aluminium doping percentages . . . . .	97
5.3	Percentage crystallinity and average crystal size of zinc oxide at different aluminium doping percentages . . . . .	98
5.4	Optical band gap of zinc oxide at different atomic doping percentages . . .	105
5.5	Percentage crystallinity and average crystal size of zinc oxide at different aluminium doping percentages . . . . .	109
5.6	Optical band gap of zinc oxide for different fabrication techniques . . . . .	114

## Introduction

The global energy demand is anticipated to rise to at least double of what it is now by 2050. This should be expected as although the world's population doubles every 43 years, the trend for carbon dioxide emission is on an even steeper path, as the graph in figure 1 shows. We observe that oil production, oil consumption, carbon dioxide emissions and the population is increasing linearly, with the gradient of  $CO_2$  emission increasing in the last 15 years. The world's gross domestic product (GDP) is increasing at an exponential rate.

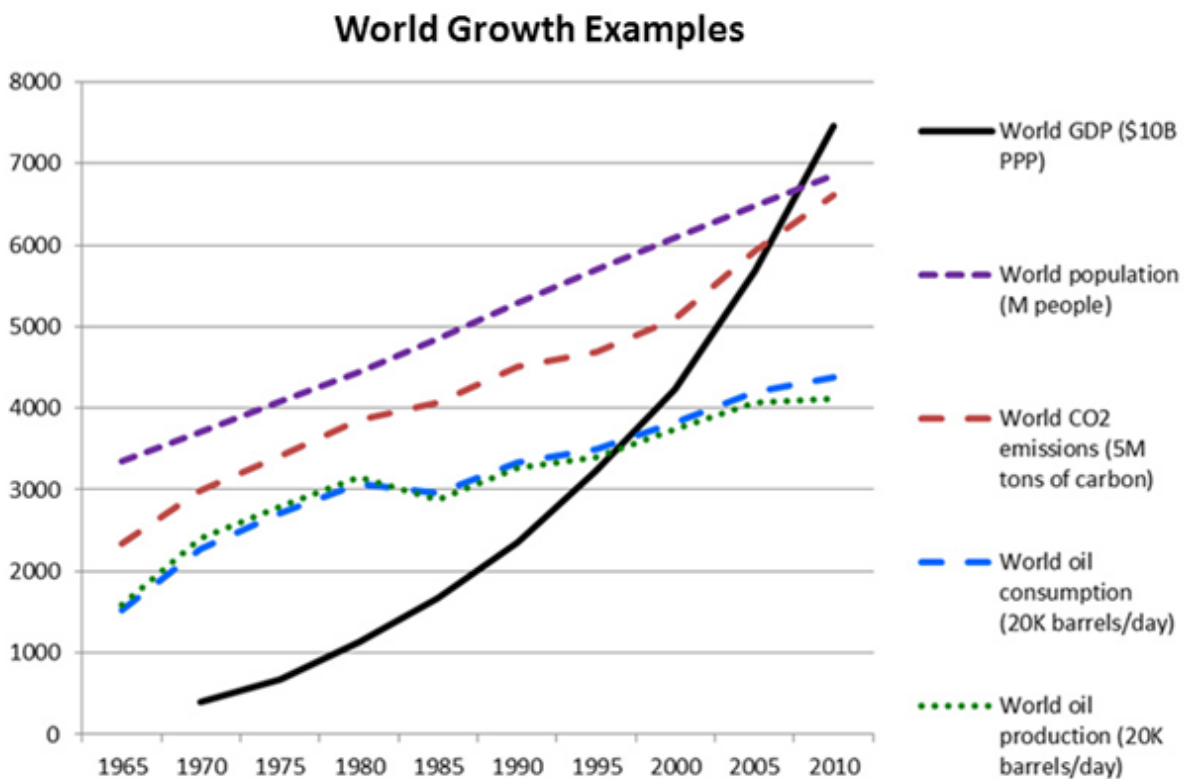


Figure 1: Growth rate of World GDP, population,  $CO_2$  emission, oil consumption and oil production as a function of time [1].

It is possible to meet the energy requirements of this rapid economic and population

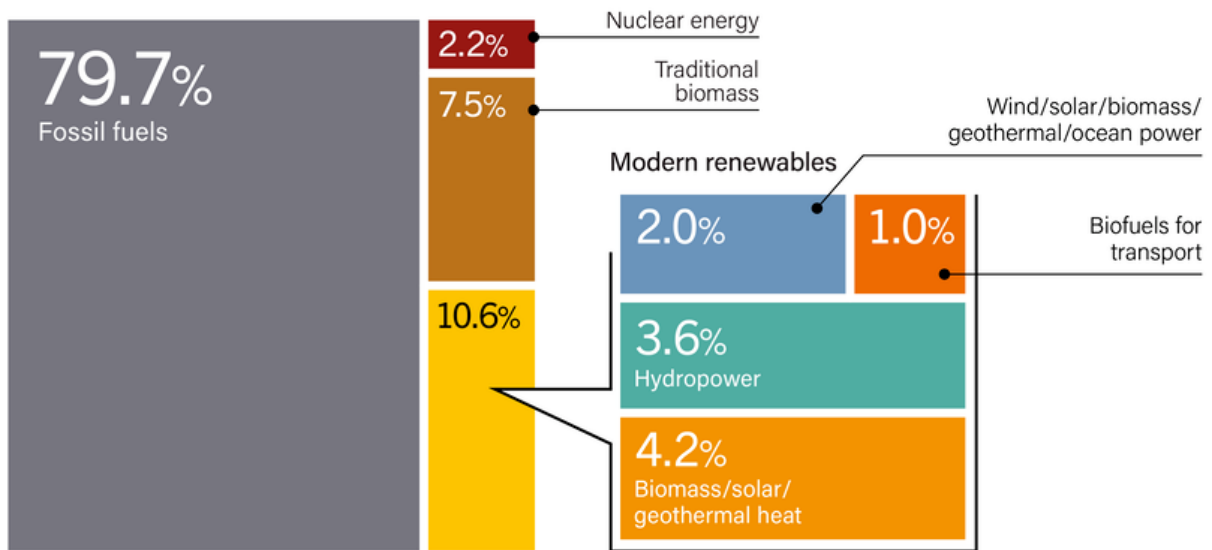


growth with the use of fossil fuels and nuclear power plants. However, the amount of waste and pollution resulting from their continued use will undoubtedly cause considerable damage to our habitat. As humans are struggling to manage the current amount of waste effectively, it is questionable how we could control it once it is doubled.

This waste problem along with the fact that fossil fuels are finite hints at an inspiring quest. We need to look at renewable energy sources for a better future.

Figure 2 shows the 2019 Global Status Report by the Renewable Energy Policy Network. We see that in 2017 only about 19% of the worlds total energy consumption was supplied by renewable sources, and only a fraction of 4.2% was supplied by solar energy. Considering that the sun supplies enough energy every minute to meet the world’s energy requirements for one year [15], 4.2% is quite a low number. In this dissertation we aim to

**Estimated Renewable Share of Total Final Energy Consumption, 2017**



Note: Data should not be compared with previous years because of revisions due to improved or adjusted data or methodology. Totals may not add up due to rounding.

Source: Based on OECD/IEA and IEA SHC.

**Figure 2: Distribution of energy production for the year 2017 [2].**

close the gap of knowledge required to develop new and innovative bio-hybrid solar energy harvesting techniques by climbing steps towards studying single molecules under the effect of an electric field, known as Stark spectroscopy, and how it could be varied to optimize their light harvesting capabilities.

Due to the high optical quality demand of the single molecule spectroscopy technique, a very specific thickness microscope slide is required. To apply an electric field over the sample at the time of measurement, the slide also has to be conductive. In bulk spectroscopy, transparent conducting oxide coated microscope slides can be bought, however, no slides of the required thickness for single molecule spectroscopy are available. In this research we ask, "can we synthesize our own transparent conducting thin films with sufficient quality for use in single molecule Stark spectroscopy?".

The synopsis of this dissertation is as follows:

## **Chapter 1**

In **chapter 1** the theory behind the workings of single molecule spectroscopy and the Stark effect were researched to gather a deeper understanding of these subjects.

## **Chapter 2**

This chapter is dedicated to semiconductors, with a literature review of the formation and existence of band gaps and other primary characteristics of semiconductors are investigated.

**Chapter 3**

First the theory of transparent conducting oxides (TCOs) is presented. The basis of this and what was learned in **Chapter 2** are then used to analyze the important properties of two candidate TCOs, tin oxide and zinc oxide.

**Chapter 4**

The three main experiments done during the period of this research project and the measurement techniques used to analyze the data are explained.

**Chapter 5**

The results obtained using the measurement techniques discussed in **Chapter 4** are exhibited for the three experiments and conclusions are drawn for each separate experiment.

**Chapter 6**

Conclusions are drawn focusing on the research project as a whole, current successes and failures are mentioned and future studies to reach the original goal are proposed.



# Chapter 1

## Single Molecule Spectroscopy and Stark Effect

### 1.1 Introduction

Before a Stark cell can be designed, it is necessary to understand the technique that will be extended upon, as well as to why it is necessary to use it. Spectroscopy is the study of how materials absorb and emit electromagnetic radiation. These absorption and emission properties are unique for each material and can hence be used for material and phase identification, among others. Analysis of the spectra of materials in bulk opens the possibility that results could be misinterpreted by ensemble averaging, which would lead to mechanisms being attributed incorrectly. It is also possible in some processes that happen sequentially that the specific dynamics or individual steps are lost as only the start and endpoints would be averaged. Single Molecule Spectroscopy (SMS) was invented to study the spectra of molecules individually and remove the drawbacks of ensemble averaging.

## 1.2 Single Molecule Spectroscopy

Figure 1.1 shows the setup for single molecule spectroscopy at the University of Pretoria.

Every step in this optical experiment has a very specific purpose as will be explained.

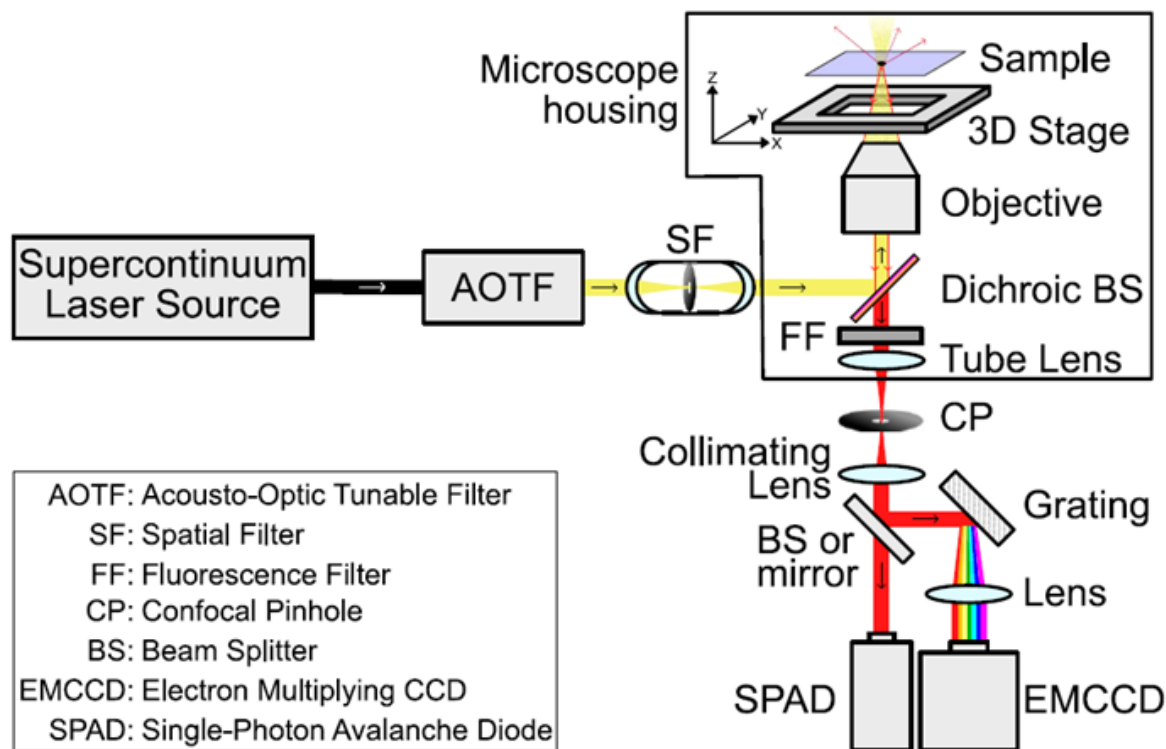


Figure 1.1: Illustration of the Single Molecule Spectroscopy setup that was to be used, showing the internal workings of the technique [3].

### Laser

The setup uses a supercontinuum laser, that is, a light source that is formed when a pump beam is acted upon by a collection of nonlinear processes that cause spectral broadening [16]. This is depicted in figure 1.2, where an 800 nm laser has been broadened to a white light supercontinuum, since the whole visible spectrum is contained within the continuum. This broadening is not always over hundreds of nanometers, as little as 60 nm has been

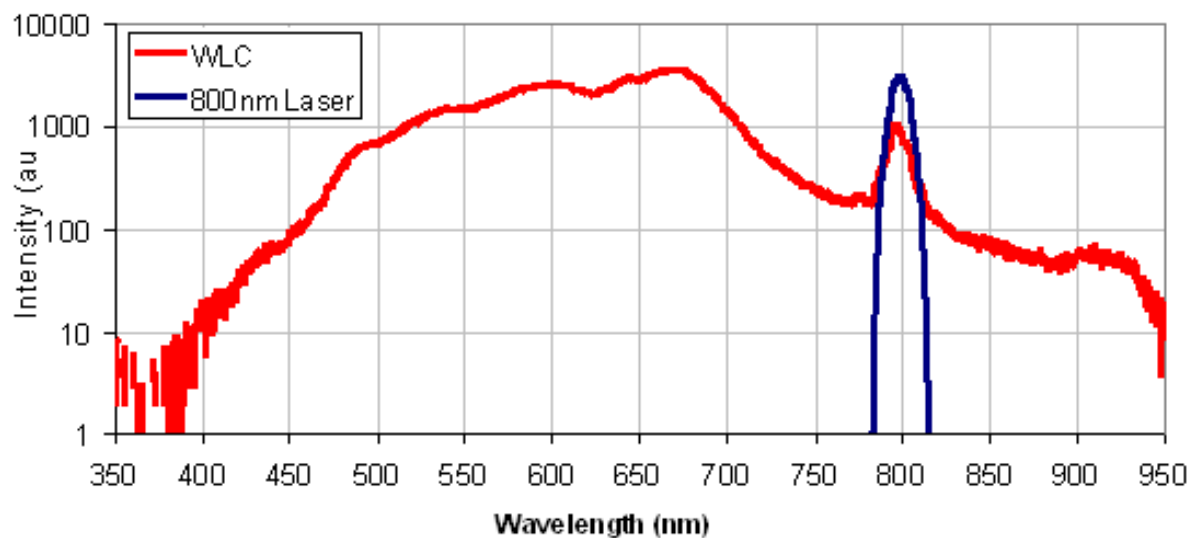


Figure 1.2: A supercontinuum spectrum that has been generated from an 800 nm laser pump in water [4].

classified as a supercontinuum [17].

The use of a filter alongside supercontinuum laser allows for precise control over a wide wavelength range for spectral measurements. It is also required for fluorescence lifetime measurements. [18]

### Acousto-Optic Tunable Filter

The filter used to control the light source as mentioned above, is an acousto-optic tunable filter (AOTF), also known as an acousto-optic modulator (AOM), allowing the modulation of a laser beam's wavelength, intensity and direction [19]. They do this through variation of the wavelength and amplitude of the sound waves traveling through the crystal. In more detail, sound waves traveling through the crystal can be thought of as creating a diffraction grating inside the crystal. The acoustic wave causes mechanical strain in the crystal, changing its permittivity and refractive index as a function of the acoustic wave properties. For constructive interference of the diffracted light to happen, one would need

$$n\lambda = \Lambda(\sin(\theta_i) + \sin(\theta_d)) \quad (1.1)$$

where we have  $n$  as an integer denoting diffraction order,  $\Lambda$  and  $\lambda$  as acoustic and optical wavelengths, respectively, and  $\theta_i$  and  $\theta_d$  the angles of the incident and diffracted light, respectively, with respect to the acoustic wave [20]. For conservation of momentum and energy, it can be shown that it is required that  $\theta_i = \theta_d$ , which would leave equation 1.1 as

$$\sin(\theta_d) = \frac{n\lambda}{2\Lambda} \quad (1.2)$$

From this equation we observe that different wavelengths of light will be scattered at different angles, and we can control the scattering angle by changing the wavelength of the acoustic wave. To select the wavelength band center of diffracted light, one needs to change the velocity and wavelength of the acoustic wave in the relationship

$$\lambda_c = \frac{\Delta n V}{f} \quad (1.3)$$

where  $\lambda_c$  is the wavelength band center,  $\Delta n$  is the birefringence of the crystal,  $f$  and  $V$  are the frequency and speed of the sound wave, respectively.

### Spatial Filter

Ideally a filter would produce a uniform Gaussian beam with just the Airy disk, which is the first order maximum of a diffraction pattern originating from a circular aperture, propagating in the required direction. Ideal systems are not possible however, so to "clean"



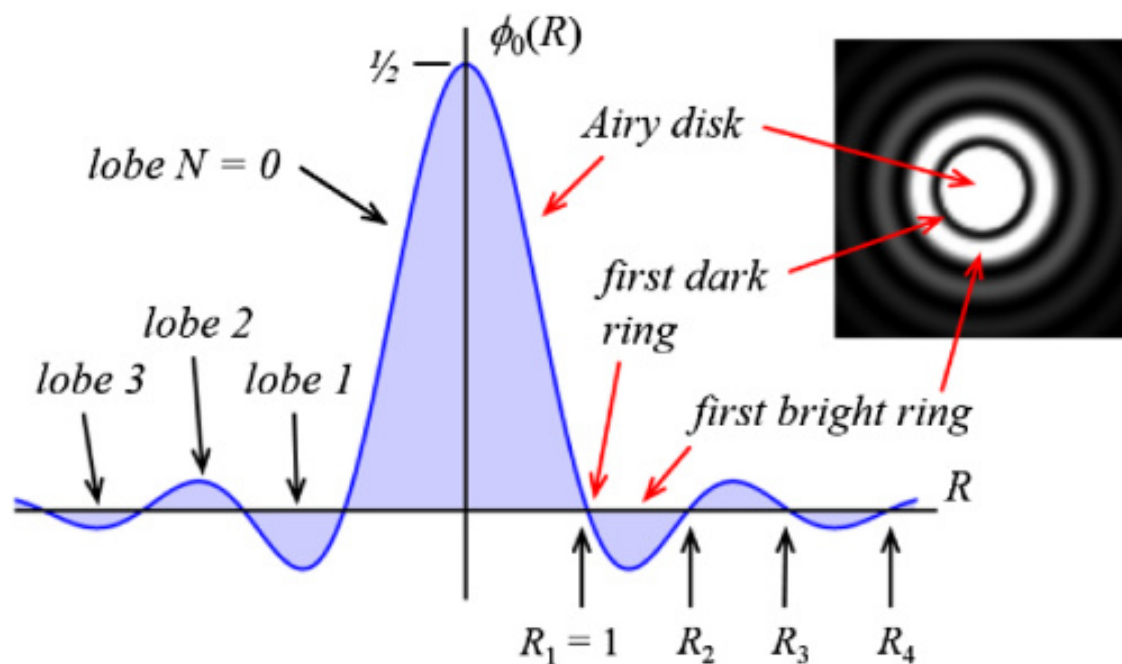


Figure 1.3: Two dimensional intensity pattern of light diffracted by a small circular aperture. The top right inset shows the different order maxima and minima with the Airy disk (first order maximum) in the center [5].

a beam of any aberrations from supercontinuum laser generation and the AOTF to be left with just the Airy disk, one uses a spatial filter. This filter is made to be only slightly larger than the Airy disk, whose radius is given by equation 1.4, such that all light not diffracted to the first order maximum will be cut off, leaving a uniform Gaussian intensity profile.

### Dichroic mirror

The phrase 'dichroic mirror' means two-coloured mirror and hints at different behavior for two different colours. In reality, a dichroic mirror behaves differently for two separate regions of the electromagnetic spectrum with a specific cutoff between them, reflecting any light with shorter wavelength than the cutoff wavelength and letting through light with a longer wavelength [21]. This is useful in fluorescence spectroscopy as the wavelength

of fluorescence emission from samples is longer than their required excitation wavelength, since some energy is lost in non-radiative transmission. In our experimental setup, a dichroic mirror reflects excitation light toward the microscope objective, while letting fluorescence light from the sample through to the detectors, as can be observed in figure 1.1.

### Objective

Excitation light reflected by the dichroic mirror travels to the objective of the microscope, which has the task of focusing the light. This focus largely determines the resolution of the measurement system which is described by the minimum distance  $r$ , at which individual points can be distinguished:

$$r = 0.61 \frac{\lambda}{n \sin \theta}. \quad (1.4)$$

It is known as the Rayleigh criterion [22] with  $r$  the distance between individual distinguishable points,  $\lambda$  the wavelength of the light,  $n$  the refractive index of the material the light is traveling in and  $\theta$  the semi-aperture angle of the lens. Here,  $r$  is the radius of the Airy disk of the light beam in the focal plane. There is a limit to the resolution, or how tight a beam of light can be focused, such that it cannot be focused to an infinitely small point. This is called the diffraction limit. Classically, this can be imagined as light traveling as a plane wave where each point on the wave front can be considered as a point source of a new circular wave front expanding isotropically, with their superposition resulting in a forward propagating wave. If this is disturbed by an edge, the point sources outside the edge will not be able to interfere with the point sources that got blocked by the edge and the superposition of the light would now appear to bend around the edge,

creating a diffraction pattern with different orders of minima and maxima.

Looking at equation 1.4 above, we realize that for a specific wavelength  $\lambda$ , the resolution is determined by  $n \sin\theta$ . This is known as the numerical aperture (NA) of an objective. The higher the NA of an objective, the smaller objects that can be distinguished individually. The maximum value for  $\sin(\theta)$  of one along with the refractive index for air of one results in the theoretical upper limit of 1.00 for the NA of dry objectives (in air). In practice, the highest obtainable NA (for dry objectives) happens at a semi aperture angle of approximately  $72^\circ$  (due to the diffraction limit mentioned before), since  $\sin(72^\circ) = 0.95$ . This limit has been overcome by use of oil immersion objectives, since oil's refractive index is higher than air's, the NA can be increased to achieve  $> 1.45$  for high end systems. By choosing oil with a refractive index similar to glass, one also reduces the amount of reflected light at the microscope glass to oil interface.

### **Confocal Pinhole**

A confocal plane is a secondary focal plane whose position is determined by the focal plane of the objective, or first focal plane, as well as its numerical aperture. This plane is on the opposite side of the dichroic mirror as can be seen on figure 1.1 , meaning lower energy fluorescence light originating from the sample will pass through it and be focused at the confocal plane.

If a pinhole is placed on this plane at the position such that light from the first focal plane passes through it, light originating from just before or just behind that plane will be blocked. This means that if you could confidently have a single molecule in the detection volume of the objective, any fluorescence from samples excited outside this detection volume would get blocked by the pinhole instead of passing through it, effectively ensuring

that the only light reaching the detectors comes from the fluorescence of the inspected sample.

Just after the confocal pinhole the light would go through a **collimating lens** creating a collimated beam, which is a beam of light where all rays propagate approximately parallel to each other with no divergence. This collimated beam will then pass through either a 50/50 beam splitter or get reflected/transmitted fully, dependent on which detection apparatus is required for the experiment.

In the available setup, the collimated beam resulting from the fluorescence of the sample is directed toward a detector dependent on what is to be studied. For time correlated single photon counting (TCSPC) a Single Photon Avalanche Diode (SPAD) is used, whereas for spectral measurements an Electron Multiplying Charge Coupled Device (EMCCD) is used.

### Single Photon Avalanche Diode

A p-n junction is made through the combination of a p-type and n-type semiconductor, where electrons from the n-type material and holes from the p-type material travel to the p-type and n-type material respectively. When this happens a space-charge region (SCR) forms, extending into the p- and n-type materials [23]. This separation of charge carriers in the SCR creates an electric field with direction from the n-type to the p-type material. This is the essence of a p-n junction and this potential difference is called the built-in potential,  $V_{bi}$  [23]. This property makes p-n junctions useful for current rectifying diodes, as it limits the flow and direction of current dependent on an externally applied voltage. A direct current (DC) voltage applied with the positive side on the p-type material would decrease the SCR and electric field such that current can flow across the p-n junction,

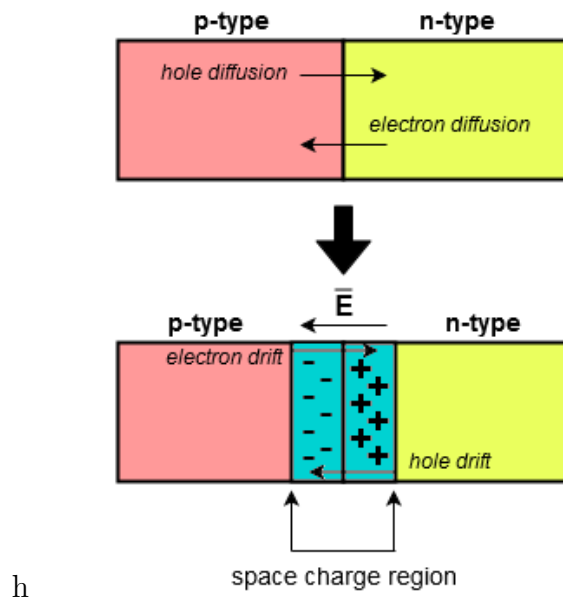


**Figure 1.4:** Migration of holes and electrons across the p-n junction causing formation of a space-charge region (depletion region).

called forward bias, and a voltage applied with the negative side on the p-type material would increase the SCR and the electric field and no current will be able to flow across the junction. The latter is called reverse bias. If a reverse bias voltage is large enough, carriers accelerated by the resultant electric field could have enough kinetic energy to overcome the ionization energy, or band gap, of the material, creating an electron-hole pair. These newly ionized carriers would also be accelerated by the electric field and obtain enough energy to create new free carriers [24].

A single carrier thus results in a chain reaction of charge carriers produced which reduces the SCR enough for a measurable current change until the external voltage can reintroduce the original SCR. Through this mechanism it is possible to measure single photons as their absorption would cause an “avalanche” resulting in a measurable current at a specific time. The main causes of the original free charge carrier generation in SPAD is either through thermal generation or the photoelectric effect [25], thus to reduce the

dark count (count of avalanche events that happened from non-photoelectric charge generation), the SPAD is cooled to well below 0° Celsius.

If spectral measurements need to be taken, the light will be directed toward the Electron Multiplying Charge Coupled Device (EMCCD).

### **Electron Multiplying Charged Coupled Device**

A Charge Coupled Device (CCD) uses a photoactive metal oxide semiconductor (MOS) interface for charge generation and accumulation. These charges are kept in small bins (order of  $\mu\text{m}$  by  $\mu\text{m}$ ) in arrays that are "read out" in a sequence, similar to a shift register, such that for each bin the charge is amplified and converted to a voltage that can be digitized to give useful information about the light that generated charge in each specific bin.

Electron Multiplying CCD's are used where the amount of light that hits the photoactive MOS interface is very low, such that too little charge is generated in the bin and the signal-to-noise ratio (SNR) is too high for reliable information to be recovered from the CCD. In these cases, an electron multiplying step is included in the operation between the shift register and charge amplification steps. Electron multiplication uses impact ionization, similar to an avalanche diode, to greatly increase the number of charges for each generated charge. The gain can be approximated by  $g \approx (1 + P)^N$  with  $P$  the gain probability at every stage of the register, and  $N$  the number of elements in the register. Even for small values of  $P$ , single input electrons can result in thousands of output electrons as  $N$  can be very large.

These bins cannot tell the difference in wavelength between different photons hitting them and thus it is necessary to split up the wavelengths before the bins if one would want to get, say, intensity data for specific wavelengths, as is the case for spectral measurements.

This is done through a diffraction grating.

### Diffraction Grating

In a diffraction grating all facets have the same angle to the normal of the grating. From

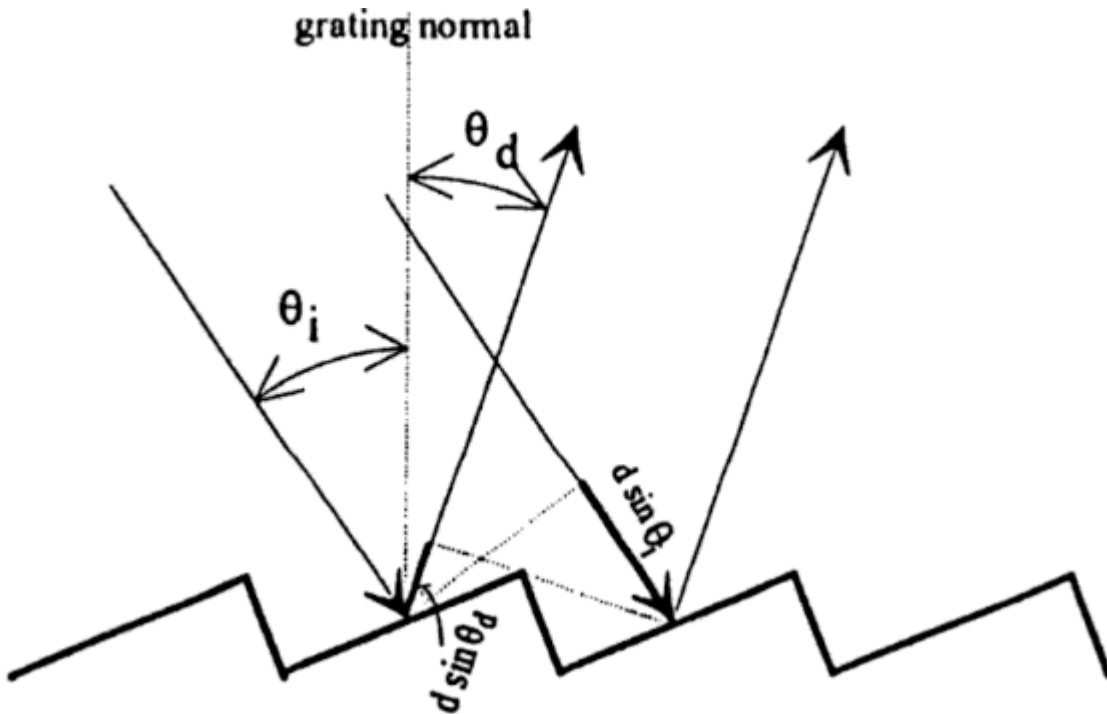


Figure 1.5: For a grating with facets separated by distance  $d$ , the path length difference between two rays hitting subsequent facets are given by  $d \sin \theta_i - d \sin \theta_d$  [6].

figure 1.5, it is observed that the geometrical path length difference between two rays scattered from subsequent facets separated by distance  $d$  will be  $d \sin \theta_i - d \sin \theta_d$  where  $\theta_i$  is the incident angle and  $\theta_d$  the diffracted angle relative to the normal of the grating. Only when this difference is equal to an integer multiple of the wavelength of the light will they be in phase and constructive interference take place, at all other angles there will be destructive interference. This interaction can be showcased by the grating equation

$$\sin\theta_d - \sin\theta_i = \frac{m\lambda}{d}, \text{ with } m = 0, 1, 2, \dots \quad (1.5)$$

From this equation we observe that different wavelengths will have different diffraction angles for the same incident angle, hence they will be separated spatially and can be directed toward different bin arrays in the CCD as required.

### 1.3 Stark Effect

The Stark effect is the splitting or shifting of spectral lines (emission or absorption) due to the presence of an externally applied electric field [7]. An electric field moves charged particles (holes and electrons) in opposite directions. For an electric field pointing from left to right as in figure 1.6, electrons in the field will be accelerated to the left.

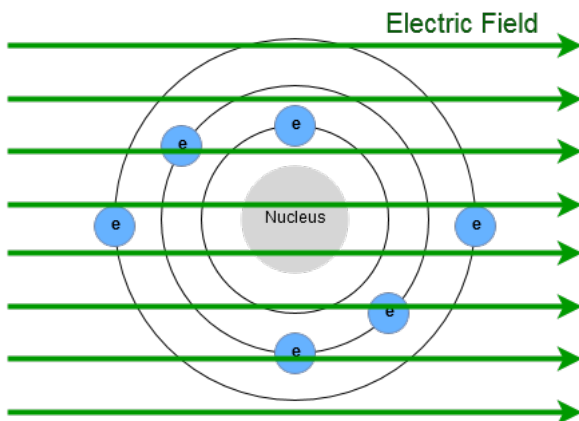


**Figure 1.6: An atom in the presence of an applied electric field.**

Since electrons have less binding energy as they move to shells further away from the nucleus, they will experience more dramatic movement due to the same electric field in the outer shells. Furthermore, depending on the immediate direction of the electron in its orbital, it will either be accelerated or decelerated (in the simple two dimensional



scenario depicted in figure 1.6). This will cause splitting of degenerate energy levels as electrons in the same Bohr model state (such as  $2s$  and  $2p$ ) would experience different acceleration/deceleration dependent on their immediate direction relative to the electric field, creating two new and separate energy levels. Figure 1.7 shows the spectral line splitting for helium, as the electric field increases to the bottom of the graph, the transition band splits into multiple bands as the electric field influences degenerate electrons in different ways as explained earlier.

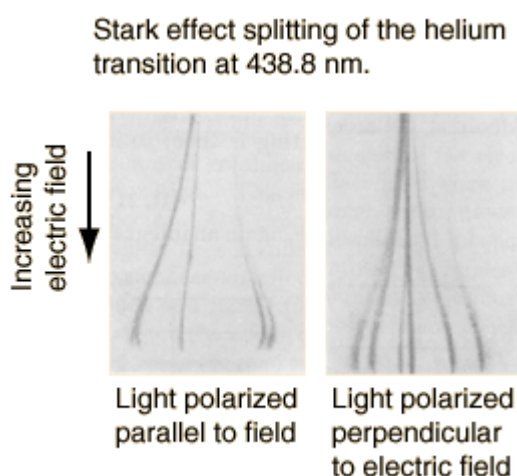


**Figure 1.7:** The splitting of helium transition at  $438.8nm$  due to the Stark effect [7].

Single molecule Stark spectroscopy is SMS with the sample under the effect of an electric field, which is achieved with a Stark cell (explained in Appendix A). SMS has been used to discover distinct dark states in the main light harvesting complex in plants (LHCII) [26]. Additional studies with SMS have shown a clear relationship between the non-photochemical quenching switch and the distinct dark states [27]. The samples (LHCII complexes) in these studies were chemically bound to a microscope glass cover slip. A similar SMS study that immobilized the LHCII complexes using an electrokinetic trap discovered a new type of dark state that was not present in studies where no electric field was present [28]. We hypothesize that the newly observed dark state is induced by

the electric field. One purpose of this project is realizing the possibility of testing this hypothesis.

Upon understanding the workings of SMS and the Stark effect, it is now necessary to move forward and investigate materials, in particular, semiconductors, as the forbidden band they possess allows us to use them as transparent conducting oxides (TCO), required for electric field generation without significant hindrance of optical capability of the SMS setup.

# Chapter 2

## Semiconductors

### Introduction

Materials are classified as conductors, semiconductors or insulators according to their electronic conducting properties. Conductors have valence electrons that are free to travel through the material, whereas insulators' valence electrons are tightly bound to their atoms.

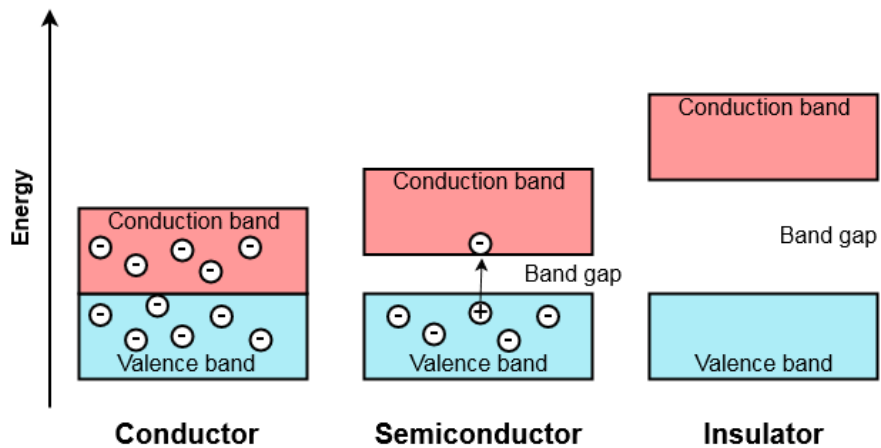


Figure 2.1: Classification of a material as a conductor, semiconductor or insulator based on its band gap.

Semiconductors vary in degree of conductivity based on their band gap. A material's band gap is the gap between the top of the valence band (highest occupied energy level) and the bottom of the conduction band (lowest unoccupied energy level). It is the energy required for an electron to break free from the valence band of its atom to the conduction band and move around freely in the lattice of the material. A semiconductor with a small band gap indicates a more conductive semiconductor than one with a wide band gap, as less energy is required for excitation across the band gap. The size of a semiconductor's band gap can be altered to some extent by doping the semiconductor.

## 2.1 Band Structure

### 2.1.1 Drude Model

The Drude model of electrical conduction was the first attempt of describing the flow of charge of a material using the idea of electrons flowing like a gas through it [29].

Several assumptions were made for this model:

- Electrons can only collide with ionic cores (considered stationary), they do not collide with each other.
- Electrons do not interact with each other or ionic cores (apart from collisions with ionic cores). In other words, electrostatic forces are ignored.
- Collisions are instantaneous and change only the electron velocity.
- Electron collisions happen with a probability of  $\tau$  per unit time.
- Thermal equilibrium of the electrons is achieved through collisions only.

This application of classical kinetic theory had some significant results, regardless of its failures. One of the most significant results of the model was an electronic equation of motion,

$$\frac{d\mathbf{p}(t)}{dt} = -\frac{\mathbf{p}(t)}{\tau} + \mathbf{f}(t), \quad (2.1)$$

where  $\mathbf{f}$  is a frictional damping term,  $\mathbf{p}$  the momentum of an electron,  $t$  the time and  $\tau$  the scattering probability. The other significant result was the linear relationship between the current density  $\mathbf{J}$  and the electric field  $\mathbf{E}$ ,

$$\mathbf{J} = \frac{ne^2\tau\mathbf{E}}{m_e}. \quad (2.2)$$

In equation 2.2  $n$  is the number density,  $e$  the constant for electronic charge and  $m_e$  the mass of an electron. This equation was obtained by finding a steady state solution ( $\frac{d\mathbf{p}(t)}{dt} = 0$ ) of equation 2.1, with the damping force  $\mathbf{f} = -e\mathbf{E}$ , then substituting the momentum into the equation for the current density due to electrons  $\mathbf{J} = -\frac{ne}{m_e}\mathbf{p}$ .

The Drude model predicts the electronic heat capacity to be significantly larger than it actually is, even at room temperature, it also fails to predict the thermal conductivity of materials as well as the ability for the Hall coefficient to be positive, and its dependence on the magnetic field.

The failures of the Drude model stem from the assumptions that the charge carriers in a material form and move like a classical ideal gas. Arnold Sommerfeld was the first to treat the charge carriers as quantum mechanical particles, leading to the model that is now known as the free electron- or Drude-Sommerfeld model.

### 2.1.2 Drude-Sommerfeld Model

In this model, the specific interactions between individual ionic cores and electrons are ignored, the ions only interact with the electrons as a mean potential throughout the crystal, acting only to maintain charge neutrality with the electrons. For this situation the one-dimensional Schrödinger equation for one electron is:

$$\left(\frac{-\hbar^2}{2m} \frac{d^2}{dx^2} + V_0\right)\psi(x) = E\psi(x). \quad (2.3)$$

In solving equation 2.3, we choose the origin  $E_0 = V_0$ , leaving us with:

$$\frac{-\hbar^2}{2m} \frac{d^2\psi(x)}{dx^2} = E\psi(x). \quad (2.4)$$

The problem is to solve this Schrödinger equation for a single electron trapped in a box of width  $a$ , subject to a mean potential  $V_0$ . Solving the Schrödinger equation for an electron in an infinite square well gives the solution for the energy dispersion of the electron as:

$$E = \frac{\hbar^2 k^2}{2m}, \quad (2.5)$$

where  $k$  is the wave vector of the electron [30]. Figure 2.2 showcases the energy dispersion relationship in  $k$ -space. It is a continuous band and will be the same for every material—not a very realistic depiction of materials science.

There can only be a specific amount of states,  $N$ , per unit volume of phase space. These states will occupy a corresponding amount in  $k$ -space.

We can describe the number of states,  $N$ , in  $l$ -dimensions with

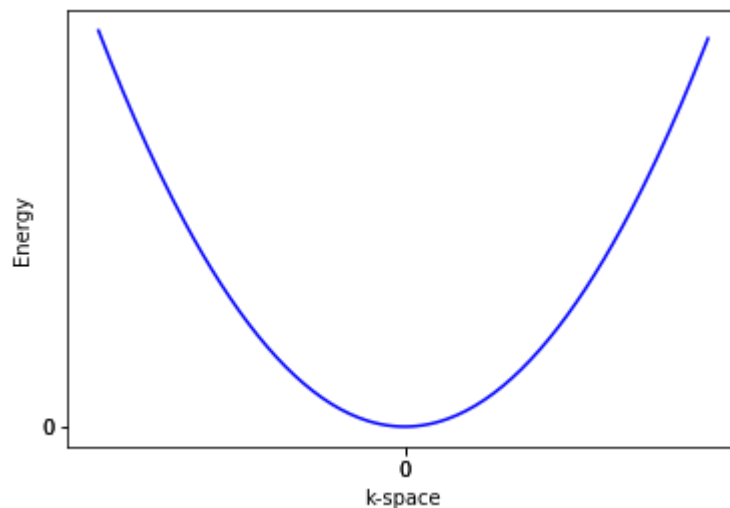


**Figure 2.2:** The energy of an electron as a function of its wave vector, the relation giving by  $E = \frac{\hbar^2 k^2}{2m}$ .

$$N = \left(\frac{1}{2\pi}\right)^l V_{kl} V_{rl}, \quad (2.6)$$

where  $V_{kl}$  is the volume in  $k$ -space and  $V_{rl}$  is the volume in real-space.

For three dimensions this becomes

$$N = \left(\frac{1}{2\pi}\right)^3 V_{k3} V_{r3}. \quad (2.7)$$

Suppose we are filling these states of a material by putting free electrons in one at a time at temperature  $T = 0$  K. The electrons will start filling the  $k$ -states of the metal at the lowest energy, but as more and more electrons are added, they will be forced to fill states of higher and higher energy. This is because of the Pauli Exclusion Principle, which states that two or more electrons (or any other half-integer spin particle, AKA fermion) cannot occupy the same state at the same time. Once all  $N$  electrons have been placed in the

metal, the  $k$ -space would be filled with a sphere of  $k$  vectors with

$$N = 2\left(\frac{1}{2\pi}\right)^3 \frac{4}{3}\pi k_F^3 V_{r3}. \quad (2.8)$$

Here  $k_F$  is the radius of the  $k$ -space sphere. The factor of 2 is included due to the spin half degeneracy of electrons, meaning each energy state is degenerate and can be filled by two electrons of opposite spins.

Using the number density  $n = N/V_{r3}$ , the previous equation can be rearranged to give

$$k_F = (3\pi^2 n)^{1/3}, \quad (2.9)$$

with electron energy

$$E_F = \frac{\hbar^2 k_F^2}{2m_e}. \quad (2.10)$$

The energy  $E_F$  is called the Fermi energy, which is the energy of the highest occupied energy state at absolute zero temperature.

The free electron model is a significant improvement on the Drude model in that it correctly predicts the temperature dependence of the electronic heat capacity, the relationship between the electrical and thermal conductivity known as the Wiedemann-Franz law, and the temperature independence of the electronic magnetic susceptibility. It still fails to distinguish between metals, semiconductors and insulators, and in determining the Hall coefficients of many metals, it fails to predict the dependence on the magnetic field and the possibility for the Hall coefficient to be positive.

The model predicts the energy dispersion of electrons to be  $E = \frac{\hbar^2 k^2}{2m}$ , which does not depend on the crystal size or shape and would be the same for every single material. The



failures of this model stems from ignoring the periodic potential of the crystal lattice.

### 2.1.3 Nearly-Free Electron Model

In the nearly-free electron model, the electrons are assumed to be subject to a small potential originating from the ionic cores. Due to the periodicity of these ionic cores in the crystal lattice, the potential is also periodic. It can be shown, using Bloch's theorem [31], that the translational symmetry in real space, with translation vectors  $\{\mathbf{T}\}$ , enforces translational symmetry in reciprocal space, with translation vectors  $\{\mathbf{G}\}$ . Bloch's theorem states that:

"The eigenstates of the one-electron Hamiltonian,

$$\mathbf{H} = -\frac{\hbar^2 \nabla^2}{2m} + \mathbf{V}(\mathbf{r}), \quad (2.11)$$

where  $\mathbf{V}(\mathbf{r}) = \mathbf{V}(\mathbf{r} + \mathbf{T})$  for all  $\mathbf{T}$  in a Bravais lattice, can be chosen to have the form of a plane wave times a function with the periodicity of the Bravais lattice" [31].

This periodicity implies that all the information will be contained in the primitive unit cell of the reciprocal lattice, called the first Brillouin zone.

This gives Schrödinger equation solutions of the form  $\psi_k(\mathbf{r}) = e^{i\mathbf{k}\cdot\mathbf{r}} v_{jk}$ , where  $v_{jk}$  is a function with the periodicity of the lattice.

Looking at the energy dispersion of the free electron model  $E = \frac{\hbar^2 \mathbf{k}^2}{2m}$  and adding the effect of the periodic translational symmetry of the lattice with reciprocal lattice vectors  $\{\mathbf{G}\}$  (but ignoring the periodic potential), we find

$$E(\mathbf{k}) = \frac{\hbar^2 \mathbf{k}^2}{2m} = \frac{\hbar^2 |\mathbf{k} + \mathbf{G}|^2}{2m} \quad (2.12)$$

for each  $\mathbf{G}$ .

This dispersion relationship results in the band structure observed in figure 2.3,

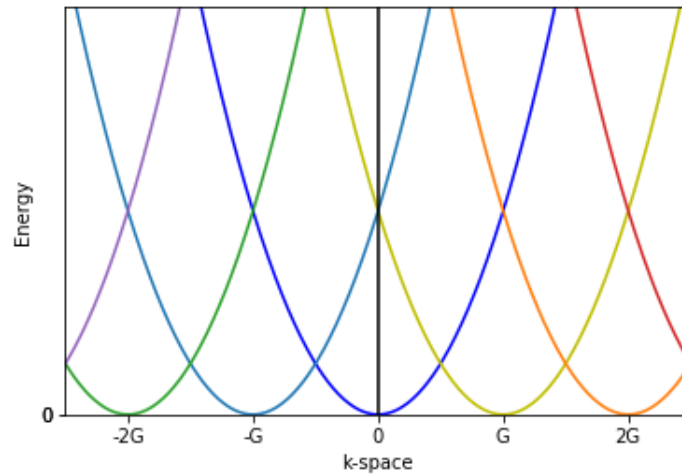


**Figure 2.3:** The energy dispersion of a periodic lattice with period reciprocal lattice vectors  $G$ , known as the repeated zone representation.

which showcases that any reciprocal lattice point can serve as the origin of equation 2.12, and that for any  $k$  there are many possible energy values. It is obviously not possible for an electron at any  $k$  to have multiple energies simultaneously. The significance of a  $k$  having multiple allowed energies stems from different bands, as electrons with the same  $k$  could be in different bands with different energies for the same  $k$ .

Since any reciprocal lattice point can serve as the origin of the representation in figure 2.3, the Brillouin zone contains all the possible energy values as a function of  $k$ . In graphical portrayals it is thus sufficient to only consider the first Brillouin zone as it contains all the system's information. This is called the reduced representation and is shown on the right of figure 2.4, where the effect of adding the small periodic potential of the lattice has been added to show how band formation happens in this model.

It is important to note that the reduced zone representation of energy as a function of

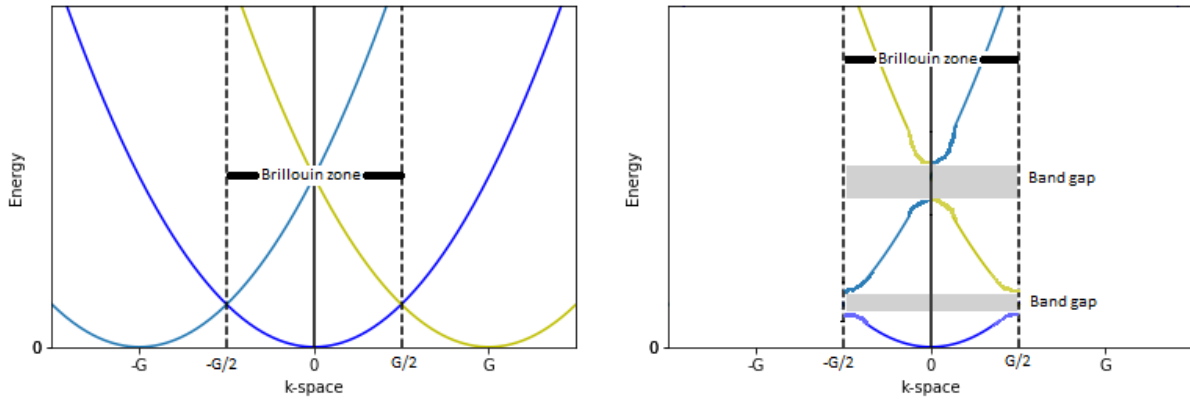


**Figure 2.4:** On the right are the bands that form due to energy dispersion relationships at the Brillouin zone center and one reciprocal lattice point away. The left image is without the effect of the small potential.

$k$  will vary dependent on the direction of  $k$  in the Brillouin zone. Figure 2.4 depicts the energy in only one direction.

### 2.1.4 Tight-Binding Model

Contrary to the nearly-free electron model, the periodic potential in the tight-binding model is large, keeping all electrons bound to their ionic cores and limiting the interactions of electrons with neighboring atoms in the solid. The result of this is that the atomic orbital of the ionic core that an electron belongs to, would be a good approximation for the wave function of said electron. The wave function of a solid can thus be approximated as the superposition of the wave functions, or orbitals, of its ionic cores.

For a simple case, consider two ionic cores close to each other with their  $1s$  orbital wave functions,  $\psi_1$  and  $\psi_2$  for one of their electrons each. There are two possible states of overlap, the bonding state ( $\psi_1 + \psi_2$ ) and anti-bonding state ( $\psi_1 - \psi_2$ ).

For the bonding state there is a probability for the electron to appear between the two

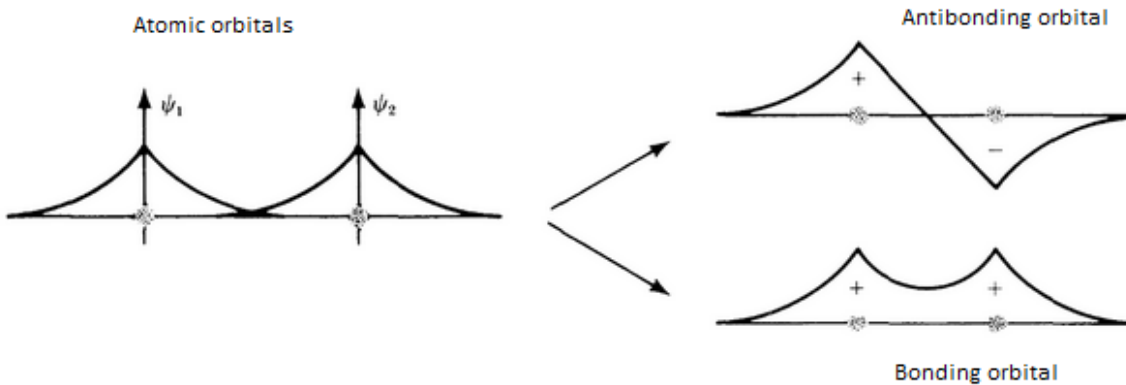


**Figure 2.5:** The atomic orbitals,  $\psi_1$  and  $\psi_2$ , of electrons tightly bound to ionic cores in their bonding and antibonding states [8].

ionic cores whereas for the anti-bonding state, the probability vanishes to the center point between the two ionic cores. This is portrayed in figure 2.5.

When  $N$  identical atoms are brought together their atomic orbitals overlap and each orbital splits up into  $N$  molecular orbitals each with a different energy, due to the Pauli exclusion principle as two atoms can not have the same quantum numbers. Since  $N$  is extremely large in solids, the molecular orbitals will be very closely spaced in terms of energy, and can be considered a continuous band. In the positions where these molecular orbitals form a chain of bonding orbitals the energies would be available, however, in the cases of anti-bonding orbitals, there will be band gaps of forbidden energies.

Figure 2.6 shows the band formation of the transition metal sodium as a function of interatomic spacing. It is observed that the overlap for core orbitals (such as  $1s$  electrons) only happens at short interatomic distance, whereas the outer orbitals ( $3s$  and  $3p$ ) experience overlap at much larger distances.

Upon understanding the reason for the existence of band gaps and how they form, the log-

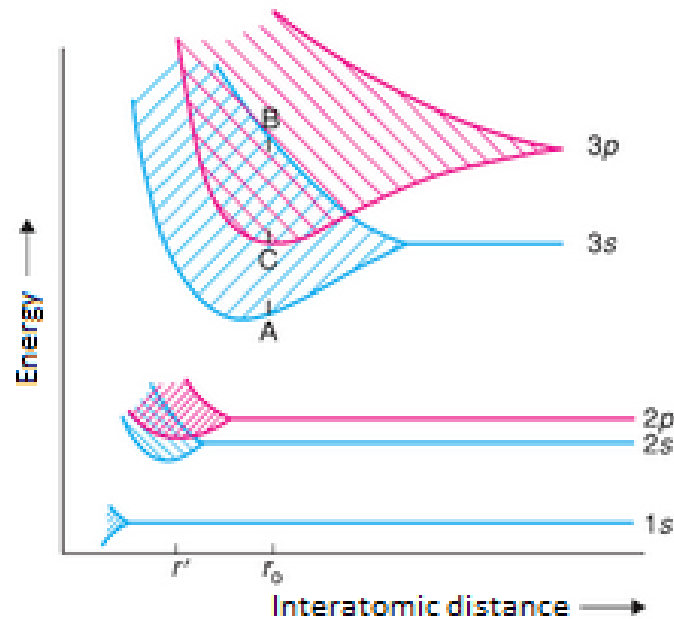


Figure 2.6: Energy of different electron states for increasing interatomic spacing, band overlap of bands for  $3s$  and  $3p$  orbitals at interatomic spacing  $r_o$ , when it is reduced to  $r'$ , there is band overlap for the  $2s$  and  $2p$  orbitals as well [9].

ical next step would be to study the influence of the band gap on materials and investigate how this could be used to our advantage.

## 2.2 Intrinsic and Extrinsic Semiconductors

### Intrinsic

All atoms that make up the material in an intrinsic semiconductor are of the type of the constituent atom/atoms that make up the semiconductor. In this case, electrons and holes always have the same carrier density ( $n = p$  with  $n$  electron carrier density and  $p$  hole carrier density), as any electron that obtains enough energy to get excited across the band gap will leave behind a hole. In other words, an electron-hole pair is always the result of

any excitation. The amount of charge carriers in intrinsic semiconductors is determined only by the properties of the matter that make up the material.

### Extrinsic

When impurity atoms are introduced into the lattice of semiconductors, they are said to be extrinsic. The process of introducing impurities is called doping. This can enhance the electronic capabilities of the material through extra extrinsic carriers introduced with either donor or acceptor doping. Doping changes a material to an n-type semiconductor, where electrons are the majority charge carriers, if the dopant is electron donating, or p-type semiconductor, with holes as majority charge carriers, if the dopant is electron accepting. This is explained in more detail in **section 2.5**.

## 2.3 Fermi Level

The Fermi level is the energy level at which there is a 50% probability for the state to be occupied at thermodynamic equilibrium. It is exactly in the middle of the band gap in intrinsic semiconductors and the energy at which this occurs at absolute zero temperature is called the Fermi energy,  $E_F$ , as briefly noted in **section 2.1.2**. The Fermi level is governed by two conditions: the "mass action law", which states that the product of electron and hole densities is constant at equilibrium, regardless of doping; and the "neutrality equation", which states that charge neutrality has to be maintained. As temperature rises, the Fermi level will move in order to conserve the number of particles and the charge neutrality, meaning the amount of states definitely occupied by electrons increases or decreases based on the material's properties. In extrinsic semiconductors, the Fermi level will move toward the conduction band edge for n-type semiconductors to maintain charge neutrality as the electron density  $n$  is higher than the hole density  $p$ , and in p-type semiconductors

it will move toward the valance band edge as the hole density is higher than the electron density.

The probability of an energy state  $E$  being occupied by an electron is given by the Fermi-Dirac distribution as they are fermions,

$$f(E) = \frac{1}{1 + \exp \frac{E-E_F}{kT}} \quad (2.13)$$

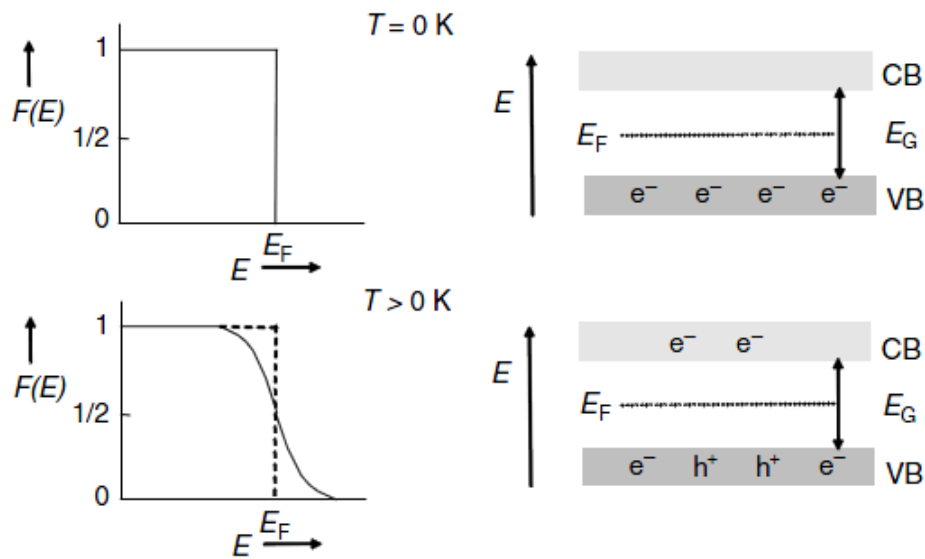


Figure 2.7: On the left is the Fermi-Dirac distribution function and on the right the Fermi level in the band gap at states  $T = 0 \text{ K}$  and  $T > 0 \text{ K}$

Figure 2.7 shows how this distribution changes from having  $f(E) = 1$ , meaning definitive occupation, at  $T = 0 \text{ K}$ , to having  $f(E) = 0.5$  when  $T > 0 \text{ K}$ . It is also observed on the right of figure 2.7 that regardless of the excitation of two electrons in the  $T > 0 \text{ K}$  case, the Fermi level stays in the center as the amount of *excited* electrons and holes are equal. If new electrons had been introduced through doping, the Fermi level would have shifted toward the conduction band and the Fermi energy in the distribution graph on the left of

figure 2.7 would have shifted to the right.

## 2.4 Defects

In a crystal lattice, each atom will ideally sit at its designated position with a crystal structure that is congruent throughout the material. Any deviations from this perfect form are considered defects or imperfections. These defects can occur during device fabrication as unwanted impurities contaminating the sample or intentional as dopants. Depending on the defect, an electronic energy state may be introduced into the band gap. This state is categorized as either a deep- or a shallow level energy state, where the words ‘deep’ and ‘shallow’ refer to their position relative to the band they can contribute to (conduction band for donors and valence band for acceptors). Shallow level energy states can be thermally ionized at room temperature due to their low binding energies, contributing extra charge carriers to their associated band. This makes them desirable defects in electronic semiconductor applications (dopants are also introduced to induce these types of energy states). Deep level states bind carriers much more tightly and in turn form localized states that tend not to contribute to free charge carriers in the material. They instead form an alternative recombination center inside the band gap with a lower energy requirement than normal recombination. This hinders the electronic conducting capability of materials. Deep level defects have use in some applications, such as fast switching devices, where the lower energy recombination centers can quickly remove minority carriers, increasing the efficiency by enhancing the switching speed of the device [32].

### 2.4.1 Point Defects

Point defects are defects in which the perturbation of the crystal lattice is localized to the origin of the defect, there is no influence on the crystal structure far from the defect site.



There exist various defects and also combinations of defects that are likely to occur.

### Vacancy Defect

A vacancy defect is when an atom is missing from its position in the periodic lattice. In ionic (or compound) semiconductors with constituent atoms  $A$  and  $B$ , a vacancy of atom  $A$  is often accompanied by one of atom  $B$ . This happens to maintain charge neutrality in the environment and is often called a Schottky defect.

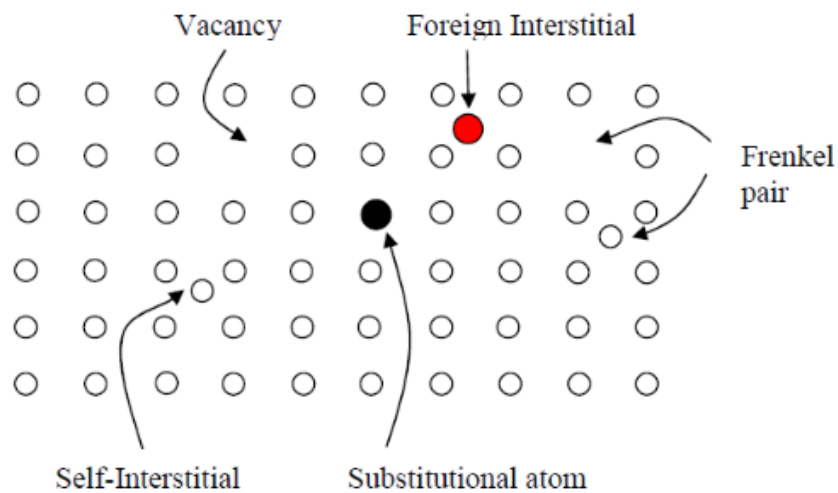


Figure 2.8: Showcase of the appearance of different defects in a crystal lattice.

### Interstitial Defect

When an atom, intrinsic or impurity, is positioned between lattice sites, *i.e.* at a normally unoccupied site, it is called an interstitial defect. These defects are generally energetically unfavorable, however there are exceptions, for example hydrogen in palladium [33].

### Frenkel Defect

A vacancy atom can sometimes be responsible for a nearby interstitial defect, this combination of a vacancy interstitial defect pair is called a Frenkel Defect.

### Substitutional Defect

Any material contains some impurities. They are often interstitial atoms, however depending on the impurity they can take a normal lattice position forming what is known as a substitutional defect.

### Antisite Defects

In a compound material with constituent atoms  $A$  and  $B$ , an antisite defect is when atom  $A$  is in the periodic lattice position of atom  $B$  and atom  $B$  is in the lattice position of atom  $A$ .

Figure 2.8 shows a visual representation of what some different defects would look like. A vacancy is always due to a constituent atom of the material not being present in the lattice and cannot form from a foreign (extrinsic) atom. They can form in different vacancy states dependent on the number of electrons present in the dangling bonds surrounding it. Each of these states would invoke a different perturbation on the crystal lattice. Interstitials can form either intrinsic- or extrinsically from foreign atoms or dopants. These atoms sit at sites that are not part of the regular lattice site, but rather squeezed in, creating a localized distortion in the lattice. Self-interstitials exist in low concentration in metal oxides as they usually have high formation energies. There are examples of low energy interstitial configurations like hydrogen in palladium as referenced before.

## 2.5 Doping

In practically all semiconductor devices, the sought-after electrical capability is achieved through doping with impurities that provide extrinsic carriers. These impurities belong to one of two categories: donors or acceptors.

Suppose a semiconductor constituent atom has a valency of  $V$ . A donor atom will have a valency of at least  $V+1$ . If this atom bonds into the host lattice it will still have an extra electron available. At  $T = 0$  K this electron will be localized to the donor atom with a binding energy less than the band gap of the host lattice. However, if the temperature is raised and the electron obtains energy above its ionization energy, it will be delocalized in the semiconductor and thus increase the charge carrier concentration. As the binding energy of donor electrons is less than the band gap, they will ionize into the conduction band faster than electrons from the host lattice.

An acceptor on the other hand, has a valency of at most  $V-1$  (with  $V$  still the valency of the semiconductor atom) and when trying to bond with the host lattice there will be insufficient electrons, resulting in a positively charged quasiparticle, called a hole, orbiting the ionic impurity. If the system obtains sufficient energy, this hole will be filled by a nearby electron, effectively moving the hole and also the charge throughout the material.



# Chapter 3

## Transparent Conducting Oxides

### 3.1 Introduction

Transparent conducting oxides (TCOs) are a special set of oxides which combine the abilities of high electrical conductivity and high transparency in the visible spectrum. They have a wide range of applications such as: transparent electrodes in solar cells, liquid crystal display (LCD) screens and touch screen technology [34], low-emissivity or 'smart' windows that reflect heat inward or outward depending on the climate (or customer's needs) [35], and transparent processing electronics.

The TCO characteristic properties are achieved by metal oxides with band gaps greater than the energy of light in the visible spectrum such that it does not get absorbed by the material. As visible light is the part of the electromagnetic wave spectrum in the wavelength range of 390 to 700 nanometers, the energy range corresponding to it is from 1.8 eV for red light, up to 3.1 eV for blue light, where these values were obtained using Planck's equation for the energy of a photon,  $E = \frac{hc}{\lambda}$ , with  $E$  the energy,  $h$  Planck's constant,  $c$  the vacuum speed of light and  $\lambda$  the wavelength. From this it is clear that

semiconductors with a band gap greater than 3.1 eV would be transparent. One would expect these semiconductors to have very low conductivity however, as there would not be significant charge generation from light.

K. Badeker was the first to produce a TCO in 1907 when a thin film of cadmium was sputtered and annealed in air [36]. Non-stoichiometric cadmium oxide formed in the annealing step due to oxygen vacancies, which resulted in penta-valent cadmium ions that formed defect energy levels with significantly less binding energy than the band gap of cadmium oxide. This material was unstable over time, as the intrinsic non-stoichiometry self-corrected over time as full oxidation occurred.

The main TCOs currently being used in industry are tin-doped indium oxide (ITO), fluorine-doped tin oxide (FTO), and aluminium-doped zinc oxide (AZO). These materials use extrinsic dopants to induce free carriers at device operating temperatures, resulting in more stable long-term products with less dependence on stoichiometry. Of these, ITO is by far the leading TCO material in industry as it still outperforms all other candidates. Due to the scarcity of indium in the earth's crust, it is becoming more and more expensive. This resulted in a 'race to replace' ITO [37], with research in other candidates increasing significantly.

## 3.2 Optical Properties

The band gap of a material is a fixed fundamental property of semiconductors. The optical band gap, however, can shift due to what is known as the Burstein-Moss effect [10]. In an intrinsic semiconductor, the optical band gap is equal to the fundamental band gap. Upon heavy doping the Fermi Level can shift into the conduction band, meaning the lower

energy states of the conduction band are occupied as shown in figure 3.1.

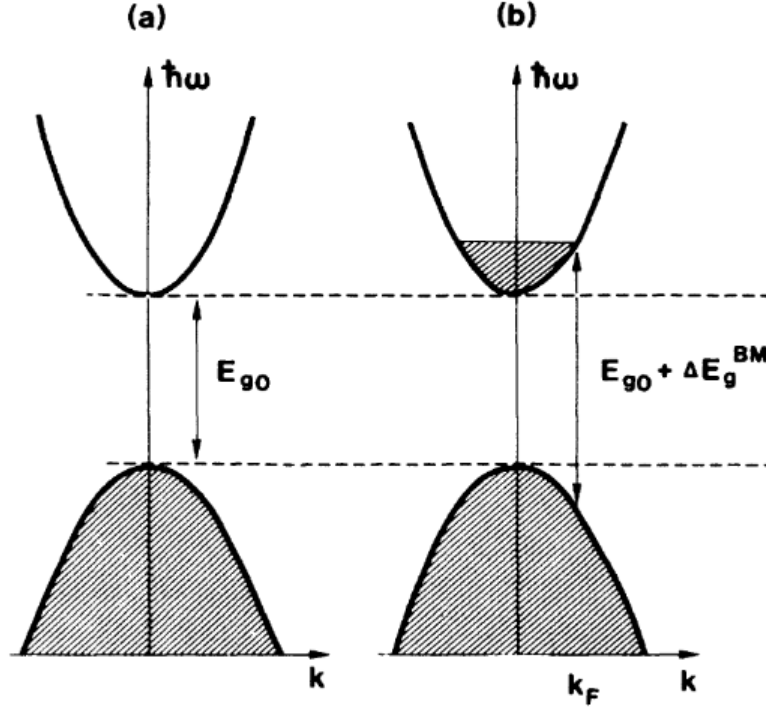


**Figure 3.1:** The optical band gap will increase with what is known as the Burstein-Moss shift as the Fermi level moves into the conduction band [10].

Since the optical band gap ( $E_{BG}^O$ ) is defined as the energy required for an electron from the valence band to be excited to the conduction band, and since the Pauli exclusion principle prevents electrons from occupying the same state, the optical band gap increases from the fundamental band gap ( $E_{BG}^F$ ) to  $E_{BG}^O = E_{BG}^F + E_{BG}^{BM}$  where  $E_{BG}^{BM}$  is defined as

$$E_{BG}^{BM} = \frac{\hbar^2 k_F^2}{2} \left( \frac{1}{m_e} + \frac{1}{m_h} \right), \quad (3.1)$$

with  $k_F$  the Fermi wave vector,  $m_e$  the effective electron mass in the conduction band and  $m_h$  the effective hole mass in the valence band.

Furthermore, upon heavy doping of TCOs, the light reflection is increased as both plas-

monic reflection off of free electrons as well as ionized impurity scattering increase with increasing doping concentrations. Plasmonic reflection is reflection of light due to plasma oscillations, (also known as Langmuir waves), which are oscillations of free electron clouds with respect to the positive ionic cores. Increasing the number of free electrons would thus increase the amount of plasmonic reflection.

### 3.3 Electrical Properties

Wide band-gap semiconductors, such as TCOs, are normally quite resistive in their intrinsic and stoichiometric forms. They are made conductive through either intrinsic defects to achieve significant non-stoichiometry, or through doping with suitable extrinsic materials as explained in **section 2.5**. Since conductivity is the movement of charge by carriers, it is possible to obtain the conductivity of a material,  $\sigma$ , by investigating the microscopic properties that govern these carriers' movement,

$$\sigma = \frac{1}{\rho} = e n_* \mu_* \quad (3.2)$$

where  $\rho$  is the resistivity of the material,  $e$  the electronic charge,  $n_*$  the density of the specific charge carrier (electron or hole) and  $\mu_*$  the mobility of the charge carrier determined by

$$\mu_* = \frac{e \tau}{m^*} \quad (3.3)$$

with  $\tau$  the average time between collisions and  $m^*$  the effective mass of the charge carrier. From equation 3.2 one can observe that the conductivity is directly proportional to the charge mobility and density, so to increase the conductivity of a TCO, it is necessary to increase either (or both) of these characteristics. To increase the charge carrier density



it is necessary to have a higher doping concentration. For a higher mobility the time between collisions has to be improved or effective mass has to be reduced. If the charge density is increased, the ionized impurity scattering centers will also increase, hindering the mobility by reducing the average time between collisions. There is thus a limit to the amount of doping that can be done without decreasing the mobility to a significant degree. As explained in **section 3.2** above, higher doping concentration also reduces light transmission in the visible range due to plasmonic reflection. Due to these drawbacks of high doping concentration, it is generally preferred to improve the mobility of the majority charge carrier of a material if its conductivity is to be improved.

Augustus Matthiessen developed a very good approximation for the mobility in semiconductors due to different scattering mechanisms. It states that the mobility of the material considering all scattering mechanisms can be approximated as the sum of the mobilities calculated for each individual scattering mechanism, as if no other were present,

$$\frac{1}{\mu_*} \approx \sum_N \left( \frac{1}{\mu} \right)_k \quad (3.4)$$

The main mechanisms influencing the mobility in semiconductors are the ionized impurity scattering  $\mu_i$ , grain boundary scattering  $\mu_g$  and lattice vibration scattering  $\mu_l$ . Also as the electron density increases, electron-electron scattering starts to become a significant factor in equation 3.3 [38].

### 3.4 Figure of Merit

Since the quality of a TCO is not determinable by one factor, a Figure of Merit (FoM) is commonly used to classify its quality. Haacke's FoM is defined as

$$FoM = \frac{T^{10}}{R_s} \quad (3.5)$$

where  $R_s$  is the sheet resistance in units of ohms per square, and  $T$  is the optical transmittance of the TCO at 550 nm.

## 3.5 Tin Oxide

### 3.5.1 Introduction

Tin dioxide is an inorganic compound which crystallizes in the rutile structure [39] shown by figure 3.2. This structure has a tetragonal unit cell, where a cubic crystal lattice has been stretched along one of the lattice vectors, resulting in a rectangular prism with a square base of length,  $a = 4.7374 \text{ \AA}$  and a height,  $c = 3.1864 \text{ \AA}$  not equal to  $a$  [40]. The coordination number, which is the number of immediate surrounding atoms, is 6 oxygen atoms for tin, and 3 tin atoms for oxygen.

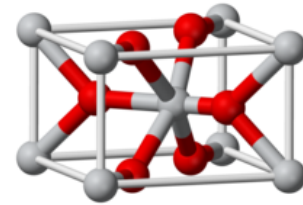


**Figure 3.2:** The rutile structure where, in this case, tin is denoted by the gray circles and oxygen the red ones.

Crystals preferring the rutile structure most commonly experience growth in the [001] direction, in other words, along the  $c$  axis. That direction is preferred as the lowest surface free energy is showcased by the [110] plane [41].

In its non-stoichiometric form, tin dioxide is generally considered an n-type semiconductor, with electrons as majority charge carriers [39]. The nature of its n-type conductivity will be explained further in the defects section. The semiconductor nature of the material and its band gap of 3.6 eV [42], suggest its use in opto-electronic applications, as explained in

Chapter 2.

The material properties of tin dioxide are being exploited for various applications. It was one of the first and is still the most used oxide in gas sensing applications. When tin dioxide is prepared in ceramic form and heated, upon rising concentration of a combustible gas, the reducing resistance can be measured and an alarm can be sound if a preselected current is measured.

It is also used as a transparent conducting electrode with ongoing research into its capability to replace the high cost indium tin oxide (ITO) as the market leader for TCO applications. The material is significantly more abundant in the earth's crust compared to indium and is thus a more cost effective long term solution. It also exhibits a greater thermal stability than ITO, hence it is preferable in any temperature dependent application.

For solar cell application, diffuse transmission is important as this property leads to the important phenomenon of light trapping whereas for low-emissivity window glass coating, this is an undesirable feature. This means that rough surfaces are generally preferred for solar cell applications and smooth surfaces for "smart" window applications (generally true for all TCOs).

### 3.5.2 Defects in SnO<sub>2</sub>

Stoichiometric tin oxide is highly resistive [43]. Intrinsic defects are responsible for its often observed n-type semiconductor behaviour. Undoped tin oxide with carrier density up to  $10^{20} \text{cm}^{-3}$  has been achieved [44]. It is widely believed that the main reason for

the n-type conductivity exhibited by tin oxide is due to oxygen vacancies in the lattice. There are examples of increasing conductivity with reduction of oxygen partial pressure in the growth conditions of tin oxide thin films in support of this theory [45, 46, 47]. As vacancies normally form deep levels in the band gap of semiconductors, it is unusual that it would contribute to n-type conductivity. It is also unlikely for oxides to be stable under such a high vacancy concentration that would allow high non-stoichiometry.

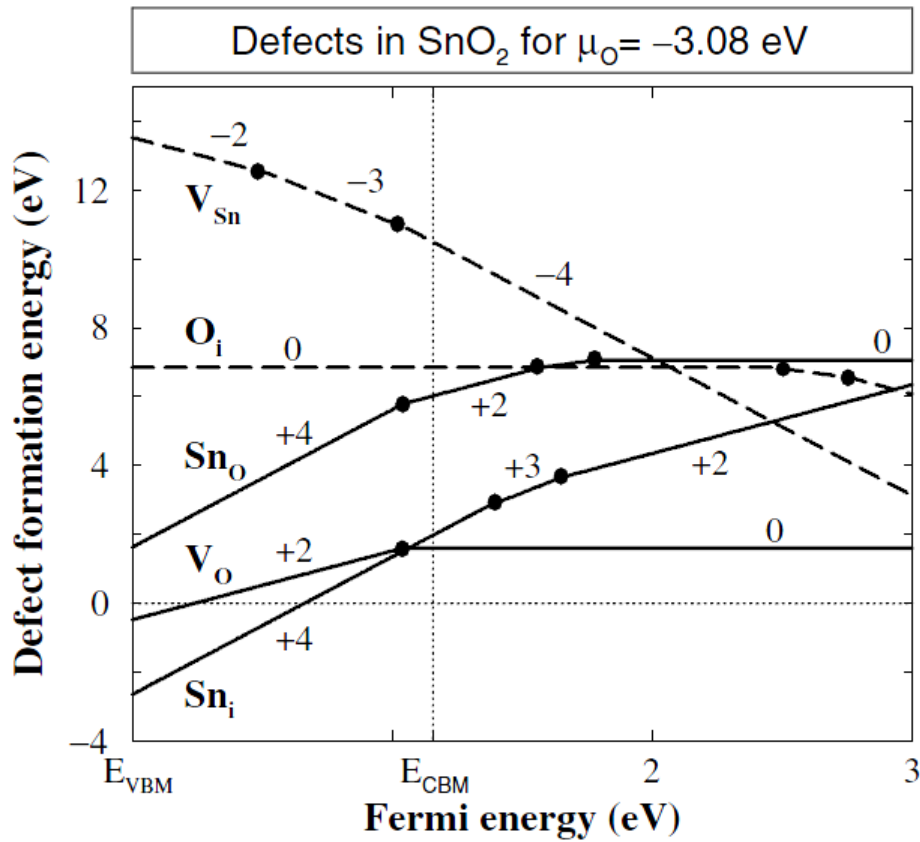


Figure 3.3: Formation energies of the different intrinsic defects in tin oxide as a function of the Fermi energy [11].

From figure 3.3 we observe that the formation energies of the tin interstitial,  $Sn_i$  and the oxygen vacancy  $V_O$  are negative when the Fermi energy is close to the valence band maximum. Consequently, these two defects will form spontaneously in p-type materials.

It can further be observed that  $Sn_i$  introduces a shallow donor level as the lowest defect transition level (from +4 to +3 charged state) lies within the conduction band and as such is fully ionized at device operating temperatures [48]. Conversely, the lowest defect transition level for the  $V_O$  (from +2 to neutral charged state) lies in the band gap and thus is ionized only for Fermi energies below this level.

As the Fermi energy rises more in figure 3.3, the formation energies of the acceptor intrinsic defects ( $V_{Sn}$  and  $O_i$ ) are lower. These defects would compensate the donor defects but due to their high formation energies in a realistic material they are unlikely to form.

The reasons for the low formation energy of the  $Sn_i$  defect are firstly that the outer electrons of  $SnO_2$  are weakly bound, and secondly that tin has two separate stable oxidation states, as is made obvious by the two forms of tin oxide  $SnO_2$  and  $SnO$  that exist. When  $SnO_i^{4+}$  forms, new bond lengths appear in the  $SnO_2$  crystal lattice similar to those found in the  $SnO$  lattice [11]. This dual valency of tin is responsible for its stability under high non-stoichiometric conditions, forming the basis for its high obtainable intrinsic n-type conductivity.

### 3.5.3 Doping

We are only interested in the conductivity and transparency of the material and we will thus only consider n-type doping, as p-type doping is still a new controversial field of study.

Tin oxide can be made conductive with electrons as majority charge carriers by 2 categories of extrinsic doping: pentavalent metals such as antimony substituting for tin, and halogens (fluorine, chlorine) substituting for oxygen. The decision of choosing a dopant is supported by understanding that tin oxide is an ionic compound with the valence band

being filled mostly through oxygen atom orbitals, and the conduction band being filled by the metal orbitals of tin.

Using the pentavalent metal doping option induces significant local perturbation in the lattice resulting in changes in the orbitals making up the conduction band, causing electrons in this band to scatter more frequently and reducing the electron mobility and consequently, the conductivity of the material in the process. Using a halogen dopant will mainly disturb the valence band orbitals and thus only slightly disturb the electrons present in the conduction band. Another important factor to consider when selecting a halogen dopant is its size relative to the constituent atom it will be substituting. Oxygen has an effective ionic radius of 1.40 Å [49], thus a halogen like chlorine with an ionic radius of 1.81 Å will distort the entire lattice around it and cause additional electron scattering due to its size. Theoretically, this would mean that fluorine would cause the least scattering as it has an ionic radius of 1.33 Å, close to oxygen, resulting in minimal lattice distortion. It has been shown that fluorine is one of the best suited dopants for tin oxide [50, 51, 52].

For the reasons explained in this section and the fact that fluorine doped tin oxide (FTO) is a heavily researched TCO for the race to replace ITO, it was selected as one of the metal oxides that will be considered for the thin film Stark cell.

## 3.6 Zinc Oxide

### 3.6.1 Introduction

Zinc oxide is an inorganic compound that crystallizes in a hexagonal wurtzite structure as pictured in figure 3.4 [53].

As can be seen, the wurtzite unit cell is a prism oriented vertically with lattice vectors  $a$  and  $b$  with  $a = b = 3.25 \text{ \AA}$  and the angle between them equal to  $60^\circ$ , defining the base of the prism. The height of the cell is defined by the vector  $c = 5.12 \text{ \AA}$  [54].

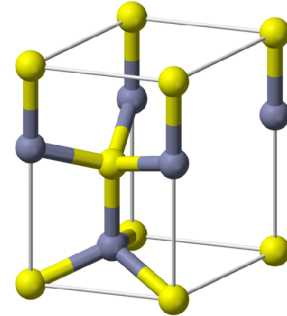


**Figure 3.4:** The wurtzite crystal structure that zinc oxide exhibits, here yellow is depicting oxygen ions and gray zinc ions.

The wurtzite structure lacks inversion symmetry, meaning there is no center point for which a reflection around that point would yield the same structure. Materials with this

property exhibit piezoelectricity and pyroelectricity, which is the accumulation of electric charge due to mechanical stress and temperature change, respectively.

Zinc oxide in its stoichiometric form behaves as a good insulator. With its preferred intrinsic defects the material becomes an n-type semiconductor with electrons as majority charge carriers [55]. The native defects responsible for the n-type conductivity are commonly believed to be zinc interstitials and oxygen vacancies [56]. The influence of defects on conductivity is still debated and will be explained in detail in **section 3.6.2**.

Similar to tin oxide, zinc oxide has a direct and wide band gap larger than the energy of visible light at  $3.37 \text{ eV}$  at room temperature [57], making it an appropriate candidate for opto-electronic applications. The large exciton binding energy of zinc oxide furthermore makes it very promising for specific optical applications [58]. Normally in a semiconductor, optical recombination of free electrons and holes gives rise to the emission of photons

at a continuum of energies, creating a broad energy range of photons. In the case of excitons, a bound state is formed at a specific energy that is approximately the same for all excitons in a material, depending on their kinetic energy. Optical recombination of these states would always result in emission of photons of approximately the same energy. This behaviour can be exploited for optically pumped lasing in zinc oxide [59].

The size of the exciton binding energy in zinc oxide at 60 meV [60] provides it with enough thermal stability to resist recombination at higher temperatures than most semiconductor materials. Zinc oxide is also a contender in the race to replace ITO as the main market TCO, as doping with aluminium delivers promising conductivity and zinc is a fairly common material in the earth's crust. Zinc oxide can also be used in gas sensing applications, as the presence of certain gases like trimethylamine, released by rotting foods, changes the electronic properties of zinc oxide in a measurable way [61].

If it is possible to grow ZnO (or any other TCO) as a p-type semiconductor, it could have many advantages in several electronic applications through the added possibility of ZnO p-n homojunctions, making transparent processing electronics such as transistors possible. This is a very desirable trait in industry! The method for growing p-type zinc oxide is complicated and not reliably reproducible. With zinc oxides' tendency to grow as an n-type semiconductor, it is rather difficult to obtain p-type doping. Even though the defects are suspected to not influence the n-type behaviour of the material to a large degree, they do have an impact as compensating centers in p-type zinc oxide [62]. Zinc oxide also does not have many candidates for doping to obtain shallow acceptors. The metal dopant candidates (Li, Na, K, Cu, Ag, Au) either form deep acceptors as substitutes or are too stable as interstitials to contribute to p-type conductivity [63]. Due to oxygen's high electron negativity, only nitrogen could be a suitable dopant to form shallow



acceptors. Zinc oxide doped with nitrogen has the most consistent reports of attempts to create p-type zinc oxide, but the absence of reports on stable p-n homojunctions of ZnO raises some doubts about the possibility of reliable p-type doping at this time.

### 3.6.2 Defects in ZnO

As any other TCO, in its stoichiometric form zinc oxide behaves as a strong resistor [64]. The intrinsic defects to consider for investigation of its non-stoichiometric n-type conductivity are the oxygen vacancy ( $V_O$ ), zinc interstitial ( $Zn_i$ ), zinc vacancy ( $V_{Zn}$ ), oxygen interstitial ( $O_i$ ) and the two antisites ( $Zn_O$  and  $O_{Zn}$ ) [65]. Deep level transient spectroscopy (DLTS) can be used to quantify these defects [66]. Similarly to tin oxide, the main culprit that was long believed to be responsible for its n-type conductivity is  $V_O$  [67]. However, it has been shown that  $V_O$  acts as deep donors forming energy states well inside the band gap such that the defect is not ionized at room (or device operating) temperature and thus cannot supply charge carriers for n-type conductivity [65].

Figure 3.5 shows the formation energies for the native defects in zinc oxide for *a*), zinc-rich, and *b*), oxygen-rich growth environments, respectively.  $V_O$  shows the lowest formation energy in the Zn-rich configuration. The defect transition level for change in charge from 2+ to neutral ( $\epsilon(2+/0)$ ) appears at 1 eV below the CBM, meaning that the neutral charge state is stable in n-type zinc oxide as the Fermi level will be above  $\epsilon(2+/0)$ . For a Fermi level near the VBM, the 2+ charge state is stable, hence it will operate as an unwanted compensating center in p-type zinc oxide. The concentration of the defect could be minimized by operating in an O-rich growth environment as this increases the formation energy of the defect.

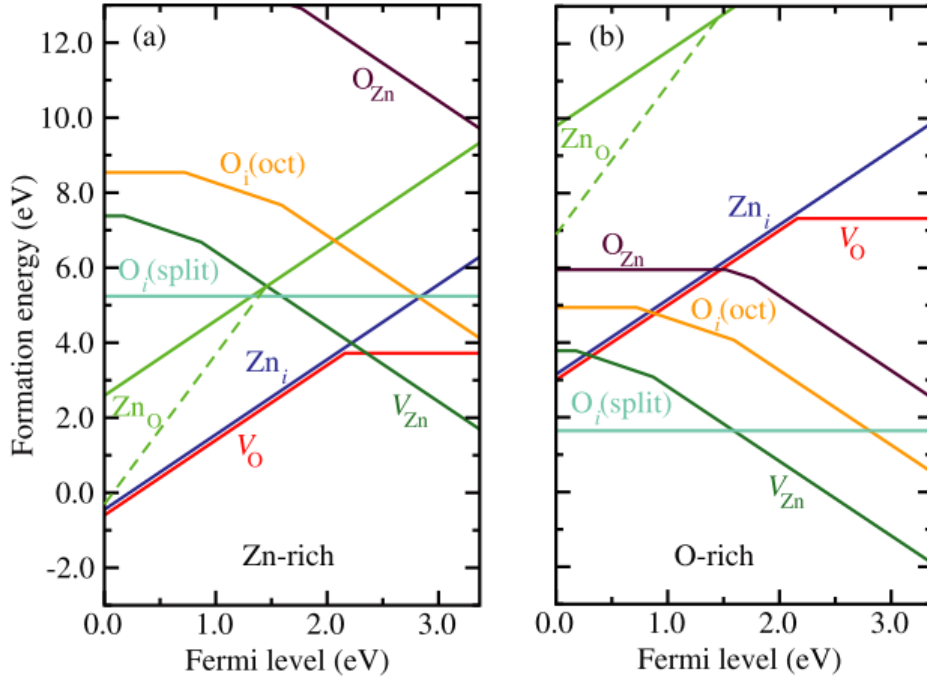


**Figure 3.5:** Formation energies of intrinsic defects in zinc oxide as a function of the Fermi level in a) a zinc rich and b) an oxygen rich growth environment [12].

We can also observe in Figure 3.5 that  $V_{Zn}$  has high formation energies in p-type materials. However, as the Fermi level shifts toward the conduction band the formation energy lowers. The  $V_{Zn}$  defect results in four oxygen dangling bonds, with a total of 6 electrons, which combine to form a doubly occupied state in the valence band, and three partially occupied states close to the VBM in the band gap with a total of 4 electrons. Thus  $V_{Zn}$  behaves as an acceptor as the three states close to the VBM can accept 2 more electrons. Since  $V_{Zn}$  has the lowest formation energy of defects in n-type zinc oxide, there will be a significant concentration of this defect acting as compensating centers toward n-type conductivity. This has been identified with positron annihilation measurements [68].

The  $Zn_i$  defect has a high formation energy in n-type zinc oxide for both oxygen- and

zinc-rich growth environments. This is in contrast to the formation energy of the tin interstitial which is low, as seen in **section 3.5**. This is because zinc does not have two separate stable oxidation states like tin has. The high formation energy of  $Zn_i$  when the Fermi level is approaching the CBM results in a low concentration of this defect in n-type zinc oxide, and it can thus not be responsible for n-type conductivity. Similarly to  $V_O$ ,  $Zn_i$  also experiences a reducing formation energy as the Fermi level approaches the VBM and is also a danger to p-type zinc oxide as a compensating center. This can be prevented by growing the material in an O-rich environment.

### 3.6.3 Doping

Similarly to tin oxide, we are only interested in donor doping.

#### Intentional Impurities

In order to induce n-type conductivity in zinc oxide, it is necessary to either dope with a group 3 element (B, Al, Ga, In) as they have an extra electron in their outer shell when compared to zinc oxide, or with a group 7 halogen which has an extra valence electron compared to the oxygen constituent atom. Both the aforementioned doping methods will induce shallow donor levels inside the band gap close to the CBM. For aluminium, 120 meV was obtained as the ionization energy alongside a low formation energy [69], leading to high obtainable carrier concentrations of approximately  $8 \times 10^{20} \text{cm}^{-3}$  [70].

The same considerations that applied to tin oxide for halogen doping apply here, thus fluorine is the best candidate for n-type doping, as explained previously. In zinc oxide, fluorine has a calculated ionization energy of 80meV alongside a low formation energy [69]. As the finally selected FTO preparation method used  $SnF_2$  as fluorine source instead of

the ammonium fluoride more commonly used for doping in zinc oxide, and the reagent required for aluminium doping was readily available, it was decided that aluminium doped zinc oxide (AZO) will be the TCO studied for potential Stark cell use.

### Unintentional Impurities

In **section 3.6.2**, it was showcased how the native defects could not be responsible for the observed n-type conductivity in undoped zinc oxide. This begs the question of what is responsible for it. Hydrogen has been drawing attention as the main culprit responsible for the n-type electronic properties of zinc oxide [71]. For practically all semiconductors, a hydrogen interstitial ( $H_i$ ) acts as an amphoteric impurity, that is, it changes its charge state dependent on the majority charge carrier of the material to always counteract conductivity. In other words, it is present as  $H^+$  interstitials in p-type and  $H^-$  in n-type semiconductors. It is thus very unusual that hydrogen is always present in the  $H^+$  state in zinc oxide, even in the n-type configuration. A  $H_i^+$  acts as a shallow donor close to the CBM that is ionized at room temperature. Furthermore, hydrogen can also act as an oxygen substitute ( $H_O$ ) which occurs in n-type zinc oxide in the positive charge state as a shallow donor with low formation energy, a trait that interstitial hydrogen also possesses [72]. Due to the low formation energies of these two forms of hydrogen defects in zinc oxide, and considering that hydrogen is present (intentionally or not) in most commonly used growth techniques (CVD, sputtering, spray pyrolysis, etc), it becomes apparent that these defects should be present in significant concentrations in as-prepared zinc oxide thin films.

# Chapter 4

## Experimental Work

### 4.1 Synthesis of Fluorine-doped Tin Oxide

As discussed in **Chapter 3**, the main purpose of this research project is to investigate the opto-electronic properties of various TCOs to determine their validity for use in a Stark cell. In this section, we discuss the synthesis of fluorine-doped tin oxide (FTO) in the study of its opto-electronic properties as a function of atomic fluorine doping percentage. This percentage was varied from 0% to 3% in steps of 1% for a total of 4 samples. Many more samples were made for optimization of fabrication procedure. Some of these findings are discussed in the appendices.

#### 4.1.1 Solution Preparation

The solution used to synthesize fluorine doped tin oxide thin films was prepared using tin(IV) chloride pentahydrate ( $SnCl_4 \cdot 5H_2O$  Sigma-Aldrich purity 98%), methanol, monoethanolamine (MEA) and tin fluoride ( $SnF_2$  Sigma-Aldrich purity 99%) as the tin source, solvent, stabilizer and fluorine source, respectively. For all doping percentages, the tin concentration was kept at 0.5 M with a 1:1 molar ratio to MEA. For each doping

percentage, a 20 ml solution was sufficient for sample preparation. The exact amounts of the reagents used were calculated using  $W = \frac{MAV}{1000}$ . Here  $W$  is the reagent amount in grams,  $M$  the concentration in mol per liter,  $A$  the molecular weight in  $g/mol$  and  $V$  the solution volume in  $ml$ . For liquid reagents, the denominator in the aforementioned equation is multiplied with the density of the reagent, resulting in  $W$  being obtained as a volume.

The tin source, solvent and stabilizer were magnetically stirred at 80 °C for 3 hours, the dopant was then added and the solution stirred for another 2 hours. The solution was then aged for 48 hours, covered with parafilm with several holes poked in.

### 4.1.2 Substrate Cleaning

Regular soda-lime microscope glass slides were used as substrates. They were cut in 2x1 cm as these dimensions were required for X-ray diffraction measurements. The substrates were degreased and cleaned with 5 minute sequential ultrasonic baths in acetone, methanol and deionized water. The substrates were then dried on a hotplate at 150 °C for 2 minutes and blown with nitrogen gas to remove any dust particles.

### 4.1.3 Deposition of thin film layers

Deposition of the thin film layers was done by spin coating technique. It was found that covering the entire surface of the substrate yielded the best uniformity of the films. The substrates were completely covered in the prepared solution and spun at 3500 rpm for 40 seconds. They were then dried on a hotplate at 150 °C for 3 minutes and left to cool to room temperature naturally. These steps were repeated to achieve a total of 5 layers per sample. The samples were then annealed in a Lindberg heavy duty furnace at 500 °C for

1 hour.

## 4.2 Synthesis of Zinc Oxide

Two distinct experiments were carried out with zinc oxide thin films. It was noticed that a different *Deposition of thin film layers* technique than the one described in **section 4.1.3** might cause a significant improvement in the quality of the films, thus before the opto-electronic properties study of aluminium doped zinc oxide (AZO), a comparative study was done to select the better procedure. Three pure zinc oxide samples were made with the old and new procedures, respectively, for a total of 6 samples in this study. This procedure is explained in **section 4.2.3**. It was not implemented for the FTO case due to time restrictions. The better procedure was selected to do the variation of opto-electronic properties as a function of aluminium doping percentage study. In order to derive more significant results from the data, a wider range of doping percentage, from 0% to 5% in steps of 1%, was used. For each percentage, three samples were prepared for a total 18 samples. The same *Solution Preparation* and *Substrate Cleaning* procedures, as described in **sections 4.1.1** and **4.1.2** respectively, were followed for both procedures, hence no differences are discussed in those subsections.

### 4.2.1 Solution Preparation

For synthesis of zinc oxide thin films the reagents zinc acetate dihydrate, isopropanol, MEA and aluminium nitrate nonahydrate were used as zinc source, solvent, stabilizer and aluminium (dopant) source, respectively. Similar to the FTO study, a 20ml solution was prepared for each doping percentage and the amounts were calculated in the same way.

The zinc source, solvent and stabilizer were magnetically stirred at 60 °C for 20 min-

utes, then the dopant was added and stirring continued for another hour. The solution was aged for 48 hours, similar to with FTO.

### 4.2.2 Substrate Cleaning

For the AZO studies, the substrate cleaning procedure was the same as for the FTO study, except that isopropanol was used instead of methanol in the middle ultrasonic bath step.

### 4.2.3 Deposition of thin film layers

As mentioned in the introduction of this section, two different procedures for deposition of thin film layers were used in a comparative study and the best one was used for the study of opto-electronic properties as function of doping percentage. These procedures will be referred to as *Procedure 1* and *Procedure 2* for the procedure used in FTO and the new procedure for which improvements in film quality were anticipated. *Procedure 1* is the same as described in **section 4.1.3**, except the annealing step was done for 30 minutes instead of 1 hour.

#### Procedure 2

The substrates were also completely covered with the prepared solution, spin-coated at 3500 rpm for 40 seconds, dried on a hotplate at 150 °C for 3 minutes, and left to cool to room temperature. The main difference in *Procedure 2* is that the samples are heat-treated (short annealing) between each layer instead of after the completion of all layers. Thus, before each new layer was made, the sample was heat-treated for 5 minutes at 500 °C, with a 10 minute anneal for the final layer.

It is believed that this could make a significant improvement in film quality as drying a spin coated film does not solidify the particles on the substrate in a significant or reli-



able way, *i.e.*, no crystallization or substrate-to-thin film interface could happen at drying temperature. It was thus hypothesized that upon addition of solution for each next layer, a significant amount of the dried particles could again be solubilised by the solvent, resulting in a new pseudo-solution of much greater concentration covering the substrate for spin coating. The number of solubilised particles would not be the same from sample to sample or from layer to layer and thus reproducibility of this procedure would not be high. Many additional problems or complications could arise from the greater concentration in the new pseudo-solution.

The 5 minute high-temperature annealing after each layer crystallized the previous deposited layer and formed a stable, new surface for the next layer. A significant increase in the crystalline quality of the films is expected for this new technique, even though the total anneal time is half that of *Procedure 1*.

## 4.3 Measurement Techniques

### Introduction

The samples' opto-electronic properties were then investigated to assess their viability as a TCO to be used in a Stark cell for single molecule Stark spectroscopy. Their optical properties were investigated with UV-visible spectrophotometry, electrical properties with the four point probe method, and morphology with scanning electron microscopy and X-ray diffraction (XRD). These methods and the data gathering procedure will be explained in this chapter.

### 4.3.1 X-ray Diffraction

The discovery of X-rays was an important step in the scientific field and has been largely used to study material properties in an effective manner. They are able to penetrate into materials due to their high energy and short wavelength, which is comparable to inter-atomic spacing. The wavelength range of X-rays is between  $10^{-8}m$  and  $10^{-11}m$  (or 0.01 nm to 10 nm).

X-ray diffraction (XRD) uses the unique material penetrating properties of X-rays to probe crystal lattices of materials and upon scattering *retrieve* data from the lattice that can be manipulated to obtain various characteristics about the material. The X-rays primarily interact with the electrons of the material to be investigated through either Thomson- (elastic) or Compton (inelastic) scattering. The rays of interest are those that were scattered elastically, since they have the same wavelengths and angles as the incident rays. This is vital for the law used to evaluate these rays, called Bragg's Law, expressed with the simple equation known as Bragg's equation:

$$n\lambda = 2d_{hkl} \sin \theta, \quad (4.1)$$

where  $n$  is the order of diffraction,  $\lambda$  the wavelength of the X-rays,  $d_{hkl}$  the distance between consecutive planes in the direction specified by the Miller indices  $hkl$  and  $\theta$  is the incident (and scattered) angle between the probed plane and the X-rays.

In this research project, a *Bruker D2 Phaser Powder X-ray Diffractometer* and the corresponding software were used for data collection. Prior to representation of the data in the studies on graphs, each sample's XRD measurements were baseline corrected. The same baseline was used for all measurements to ensure that important individual features were

not removed. It was created by the average of various XRD measurements of a reference substrate, as it was comparable to the official Bruker XRD software's suggested baseline to the samples. The suggested baseline was not used as it may remove some significant features.

With the data represented on graphs, the percentage crystallinity of each sample was determined by calculating the integrals of crystalline peaks and dividing them by the integral of the entire scanning angle ( $2\theta$ ):

$$\%Crystallinity = \frac{\text{Integral of crystalline peaks}}{\text{Integral over entire scanning angle}} * 100. \quad (4.2)$$

The full width at half maximum (FWHM) for each individual peak was obtained by fitting a Gaussian curve to the data with graphing software. Using the FWHM of different prominent peaks, the average crystal size was determined in two ways: the standard way is to take the average of the crystal sizes for each peak (plane orientation); additionally, in this study, the weighted average crystal size was determined by taking the relative size of the peaks (their area) into account. The latter method should be more accurate as the amount of crystals per orientation is considered.

Calculation of the lattice parameters for a hexagonal lattice is done by the equation:

$$\frac{1}{d_{hkl}^2} = \frac{1}{a^2} \left[ \frac{4}{3}(h^2 + k^2 + hk) + l^2 \left( \frac{a}{c} \right)^2 \right], \quad (4.3)$$

whereas for tetragonal rutile structure, the calculation is done by:

$$\frac{1}{d_{hkl}^2} = [h^2 + k^2 + l^2 \left( \frac{a}{c} \right)^2] \frac{1}{a^2}. \quad (4.4)$$

### 4.3.2 Four Point Probe

The four point probe, or four terminal sensing method, is a more precise electrical impedance measurement technique than the two probe ohmmeter. Instead of measuring the voltage on the same probes used to apply the current (like the ohmmeter), the four point probe uses two pairs of probes, to apply current and measure voltage respectively, in a straight line as figure 4.1 shows. A very precise current ( $I$ ) is passed through the outer two probes

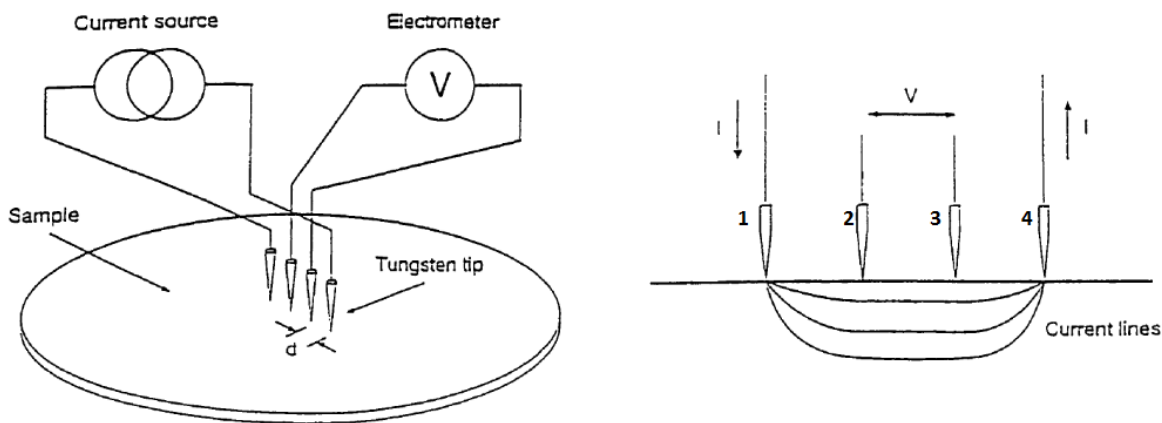


Figure 4.1: Representation of the four point probe setup. [13]

(1 and 4 in figure 4.1), while the inner pair (2 and 3) measures the resultant voltage ( $V$ ) over the interested area. The sheet resistance is then calculated with the equation:

$$R_s = k \frac{V}{I}, \text{ with } k = k_1 k_2 k_3 \quad (4.5)$$

where  $k$  is the combination of the correction factors  $k_1$ ,  $k_2$  and  $k_3$ . The  $k_1$  factor depends on the sample geometry and probe spacing compared to sample size, thus for a specific four point probe setup it has different values for every shape (circle, square, rectangle) and size of a sample. The samples used in this study were of dimensions  $25 \times 15 \text{ mm}^2$ , thus rectangles with a *length to width* ratio of 1.67, and a *width to probe spacing* ratio of 15, giving us a correction factor  $k_1 = 4.39$  [73]. As the thickness to probe spacing ratio is ex-

tremely small, the second correction factor is equal to unity, or  $k_2 = 1$ . The last correction factor is dependent on the temperature of the sample at the time of measurement. These measurements were all made in an air-conditioned lab at a temperature of approximately 26 °C giving  $k_3 = 1.02$ .

The electronic properties of the thin film material is an important parameter of a TCO. In this project, the resistivity,  $\rho$ , of samples is determined through the measured sheet resistance ( $R_s$ ) with the relationship

$$\rho = R_s t, \quad (4.6)$$

with  $t$  the thickness of the thin film. The sheet resistance has a physical unit  $\Omega$ , however, it is almost exclusively expressed as  $\Omega/\square$  (*Ohm per square*) from its relationship with the resistance of a bulk material with dimensions *length*( $l$ ), *width*( $w$ ) and *thickness* ( $t$ ):

$$\begin{aligned} R &= \frac{V}{I} \\ &= \rho \frac{l}{wt} \\ &= R_s \frac{l}{w} \end{aligned}$$

Thus the resistance of a sheet is shown by  $R_s$ , regardless of its size, provided the *width* and *length* are equal, *i.e.* provided it is a square [73].

### 4.3.3 UV-Vis Spectroscopy

Ultraviolet to visible spectroscopy, or UV-Vis spectroscopy, was used in this study to investigate the optical properties of the TCO thin films. This was done with a spectrophotometer. It compares the input intensity of light before ( $I_0$ ) and after ( $I$ ) it passes

through the sample and calculates the transmittance with the ratio  $I/I_0$ . From this, the absorbance of the sample can be calculated using the following equation:

$$A = 2 - \log \%T, \quad (4.7)$$

where  $A$  is absorbance and  $T$  the percentage transmittance. A *Cary 100 Bio UV-Visible series II spectrophotometer* was used. It uses a tungsten halogen visible light source and a deuterium arc ultraviolet source, having a total wavelength range of 190 nm to 900 nm. As figure 4.2 shows the source light passes through a monochromator and splits into two

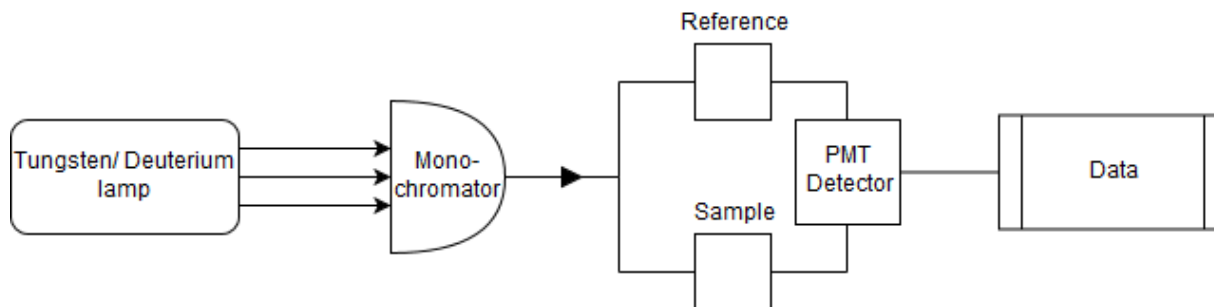


**Figure 4.2: Diagram of the ultraviolet to visible setup.**

beams, passing through the sample of interest and a clean soda-lime microscope slide reference substrate, allowing us to measure  $I_0$  and  $I$  simultaneously, ensuring we eliminate the effect of the substrate the thin films are coated on. It then reaches the photomultiplier tube (PMT) detector. The monochromator is responsible for stepping through the wavelength range using a diffraction grating, and the PMT to multiply the current produced by incident light, allowing for the detection of even individual photons.

Another important TCO characteristic that can be derived from the UV-Vis data is the optical band gap, or *Tauc gap*. Using the energy of the light,  $h\nu$ , with  $h$  Planck's constant and  $\nu$  the frequency of light, and the absorbance of the sample obtained with UV-Vis

spectroscopy, one can obtain a Tauc plot by plotting  $hv$  on the  $x$ -axis and  $(\alpha hv)^{1/n}$ , where  $\alpha$  is the absorption coefficient, on the  $y$ -axis. The absorption coefficient can be obtained with the Beer-Lambert law as  $\alpha = \ln(1/\%T)/t$ , where  $t$  is the thickness of the film. The band gap can then be obtained using the equation:

$$(\alpha hv)^{\frac{1}{n}} = C(hv - E_g), \quad (4.8)$$

where  $C$  is the proportionality constant of the linear fit of the Tauc plot,  $E_g$  is the optical band gap and  $n$  is defined by the nature of the transition, since both the studied TCOs in this study have direct band gaps of least energy,  $n = 1/2$ , giving  $(\alpha hv)^2 = C(hv - E_g)$ . From this equation we can deduce that:

$$(\alpha hv)^2 = 0 \text{ when } E_g = hv, \quad (4.9)$$

making it possible to determine the optical band gap from Tauc plots.

#### 4.3.4 Scanning Electron Microscopy

A scanning electron microscope (SEM) produces images of a sample by making use of the interactions between an electron beam and the sample. Information about the sample's morphology, composition, topology and crystallographic properties can be obtained by the different techniques contained within SEM. In this study, a *Zeiss Crossbeam 540 Field Emission Gun (FEG) SEM* setup was used to study the morphology of the samples. With this setup, the primary electron (PE) beam is formed by a Schottky type emitter held at a large negative potential relative to a nearby electrode. The electric field over the emitter induced by the negative potential lowers the surface barrier for electrons and causes an emission current. When the electron beam reaches the sample it interacts with it in

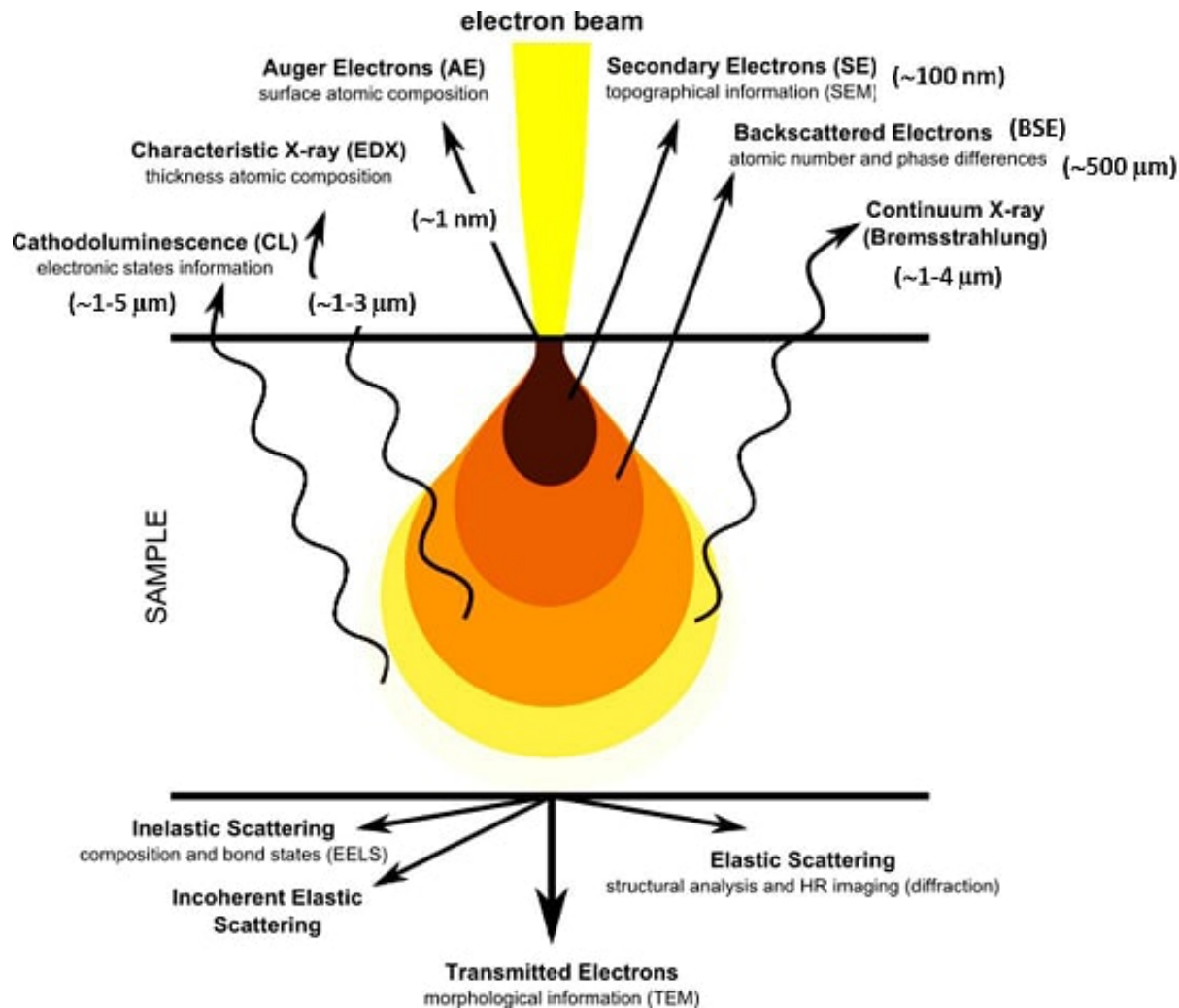


Figure 4.3: Diagram of the teardrop shaped interaction volume in SEM [14].

a teardrop shaped volume known as the interaction volume. This can be seen in figure 4.3. The two most common surface morphology probing signals are secondary electrons (SEs) and back scattered electrons (BSEs). SEs are kicked out of the atom by the PEs close to the surface of the sample and are used for high-resolution images of the sample surface, whereas back-scattered electrons are reflected deeper inside the sample by elastic scattering giving information about the element distribution inside the sample. The SE scanning mode was used in this work to study the surface morphology at high resolution. The continuous electron beam results in the collection of charge on the surface of non-



conductive samples, resulting in scanning faults and image artifacts. To ensure high resolution imagery, samples were coated with graphite to increase conductivity and grounded on a metallic sample holder to prevent accumulation. SEM was also used to determine the thicknesses of some films through cross-section imagery. It was the only option available for thickness determination in this project. The procedure for obtaining cross-section micrographs went as follows:

- Cut off a piece of the sample.
- Scratch a straight line in the middle of the opposite side of the thin film with a diamond or glass cutter.
- Place the small sample inside a liquid nitrogen bath (with the necessary protective gear) with the scratched line on a pivot point (like a seesaw).
- Apply pressure on both endpoints of the sample so as to snap it at the scratch.

There were not many opportunities to design and test this procedure, and approximately 70% of all attempts failed. The samples on metallic sample holders for normal SEM surface imaging and cross-sectional SEM can be seen in figure 4.4.

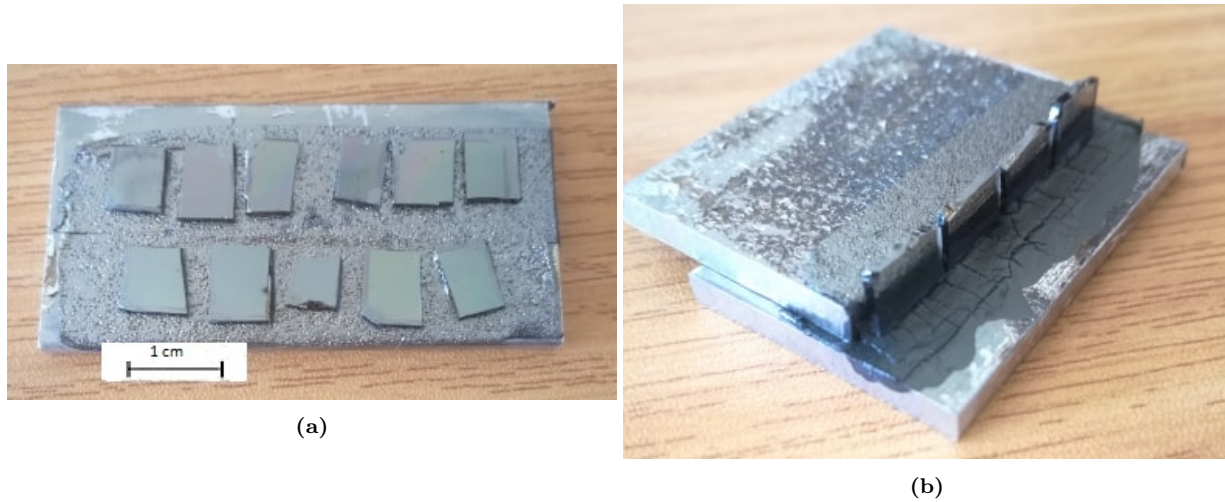


Figure 4.4: Small cuttings of samples immobilized on metallic plates with conductive sticky tape in (a) surface imaging and (b) cross-sectional imaging configurations

# Chapter 5

## Results and Discussion

### 5.1 Opto-Electronic Properties of Fluorine Doped Tin Oxide

#### 5.1.1 X-ray Diffraction

The XRD patterns of tin oxide at different levels of fluorine doping are shown alongside the standard powder diffraction file for tin oxide (PDF 00-041-1445) in figure 5.1. There is a large amorphous phase in the  $2\theta$  range of  $15^\circ - 37^\circ$ . The peaks of crystals growing on the [110], [101], [200] and [211] planes, corresponds to the  $26.61^\circ$ ,  $33.89^\circ$ ,  $37.95^\circ$  and  $51.78^\circ$   $2\theta$  positions of the standard PDF, respectively. We observed the peaks at  $26.29^\circ$ ,  $33.57^\circ$ ,  $37.63^\circ$  and  $51.46^\circ$ , thus they are shifted slightly to the left with respect to the PDF peaks. This is due to the effect of the doping on the lattice parameters of tin oxide. Preferred orientation was observed on the [110] plane, this is in accordance with the PDF of tin oxide, showcasing that a degree of crystallinity was achieved. In the 0%, 2% and 3% samples, no phases corresponding to the dopant are observed, indicating successful incorporation and even dispersion of the dopant into the material lattice. In the 1%

sample, however, the  $24.4^\circ$  phase of the fluorine PDF (PDF 00-072-0822) was observed. From this it can be deduced that the dopant was not dispersed evenly in the host lattice. This most likely happened due to insufficient heat, or too short cooking time during the solution preparation procedure described in **section 4.2.1**, resulting in an incomplete reaction.

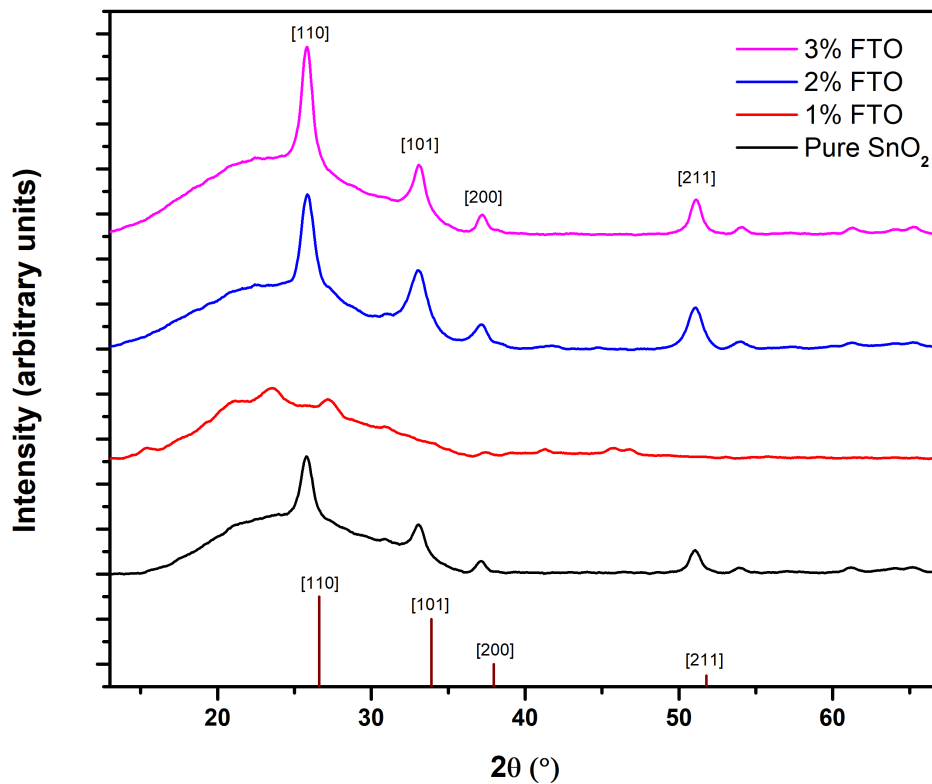


**Figure 5.1:** XRD of tin oxide at different doping levels, with the standard PDF of tin oxide (00-041-1445) at the bottom. The heights of the PDF peaks indicate the relative intensity

We observe preferred growth on the [110], [101] and [211] planes, with the [110] plane exhibiting the most preferential growth. This is in good agreement with what was found in the literature, as noted in **section 3.5.1**. From the data of the graph, the percentage

crystallinity, average crystal size and weighted average crystal size for each doping level were determined as described in **section 4.3.1** and are represented in table 5.1.

**Table 5.1: XRD data of tin oxide at different doping percentages**

Doping percentage (at%)	% Crystallinity	Average crystal size (nm)	Weighted average crystal size (nm)
0	39.58	9.45	5.87
1	25.15	3.62	3.28
2	34.82	6.12	6.24
3	32.49	11.34	8.78

Even though the prominent peaks experience an increase in intensity with increasing doping, as is observed in figure 5.1, table 5.1 shows that the percentage crystallinity decreased with doping, with exclusion of the 1% sample. This is because the amorphous phase also grew larger with doping due to substitution changing the coordination number, causing unsaturated bonds which distort the crystal lattice around them. The average crystal size changes radically from sample to sample even though these changes are not suggested by the diffractograms depicted in figure 5.1, apart from the 1% doping sample. We believe that this is due to the way in which the average crystal size is commonly determined, ignoring the number of crystals contributed by each peak. The weighted average crystal size, determined as explained in **section 4.4.1**, showcases more realistic deductions from the diffractograms, with the crystal size increasing as the crystal peaks become more intense. No shift was observed in the peaks' positions due to doping, hence the lattice parameters for all samples were equal with  $a = b = 4.827 \text{ \AA}$  and  $c = 3.226 \text{ \AA}$ . There is slight deviation to the researched lattice parameters of  $a = 4.7374 \text{ \AA}$  and  $c = 3.1864 \text{ \AA}$ . It was later discovered that this was due to the instrumental shift of the XRD data, corrected for in the following studies.

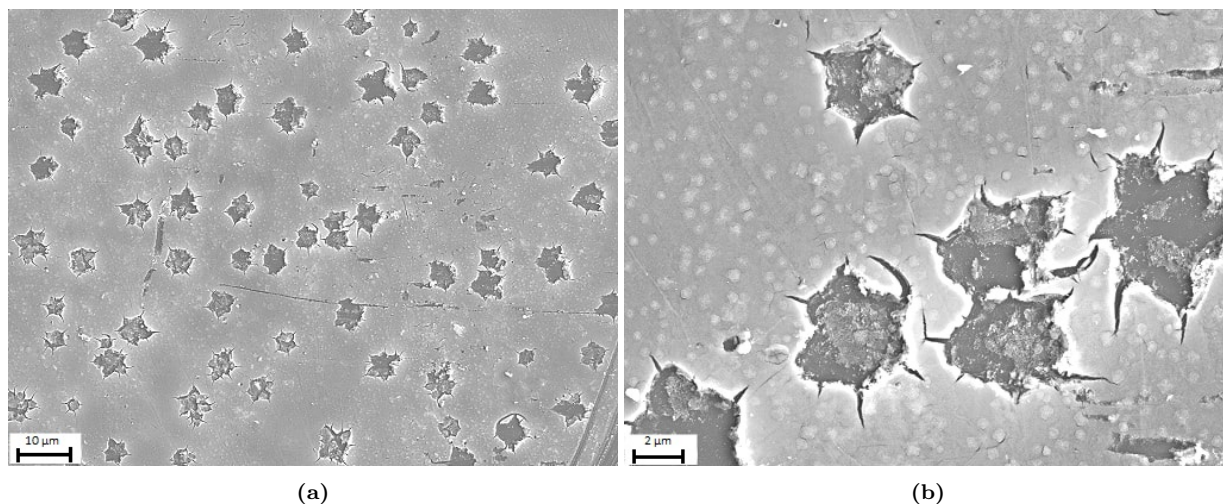


**Figure 5.2:** SEM micrographs of 1% fluorine doped tin oxide at (a)  $10\mu\text{m}$  and (b)  $2\mu\text{m}$  scale.

### 5.1.2 Scanning Electron Microscopy

It should be noted that the films appeared visibly dark of colour, with 0% and 1% samples appearing almost entirely blackened, as if they had burned. With a better idea of the structural properties of the samples, it was necessary to do SEM to investigate the darkness and morphology of the films. The SEM results obtained of the 1% sample are shown in figure 5.2. Whereas XRD showed an amorphous structure with no significant peaks, the electron micrographs show an amorphous film covering the surface with various holes. They appear to have formed from upwards bursting of something beneath the film. We suspect that this was due to unsatisfactory preparation of the solution, as explained before. It is likely that solvent was trapped beneath the film and caused these holes during the annealing step.

Figure 5.3 shows a wide image of the undoped, 2% and 3% doped samples. We observe a significant amount of agglomeration into clusters of tin in the undoped sample, with it covering almost the entire surface of the film. The density of the tin clusters is lower in the 2% sample and they are generally smaller as well as more uniform compared

to the undoped sample. The density and average size of the clusters decrease further for the 3% sample. This explains the increase in crystallinity with increasing doping percentage observed in XRD in figure 5.1. Furthermore, doping is known to inhibit the process of nucleation and growth [74].

Zooming in between the clusters to a nanometer scale, we observe that the agglomeration density is similar for the smaller particles, which is to be expected as the rate of agglomeration would be relatively constant everywhere on each film. Agglomerated clusters can clearly be seen in the undoped sample. The initial stages of agglomeration, with individual crystals visible inside the clusters, are observed for the 2% sample, with almost no agglomeration visible for the 3% sample.

### 5.1.3 Ultraviolet to Visible Spectroscopy

As noted in **section 5.1.2**, the films appeared dark and it is expected that the transmittance would therefore not be sufficient for TCO applications. The obtained UV-vis spectroscopy results are depicted in figure 5.5. We observe that the undoped and 1% doped samples have extremely low transmittance, with an average of 10%.

The 2% and 3% samples have significantly higher transmittance with an average of approximately 50% and 60%, respectively. However it is unclear from these results alone whether that is sufficient for TCO applications, the figure of merit is determined in the conclusion of this experiment. There is a sharp decrease in the transmittance as the wavelength decreases, until a trough at 290 nm, followed by a sudden increase to form a 'peak' between 290 nm and 230 nm. It was found in literature that this is a common finding and

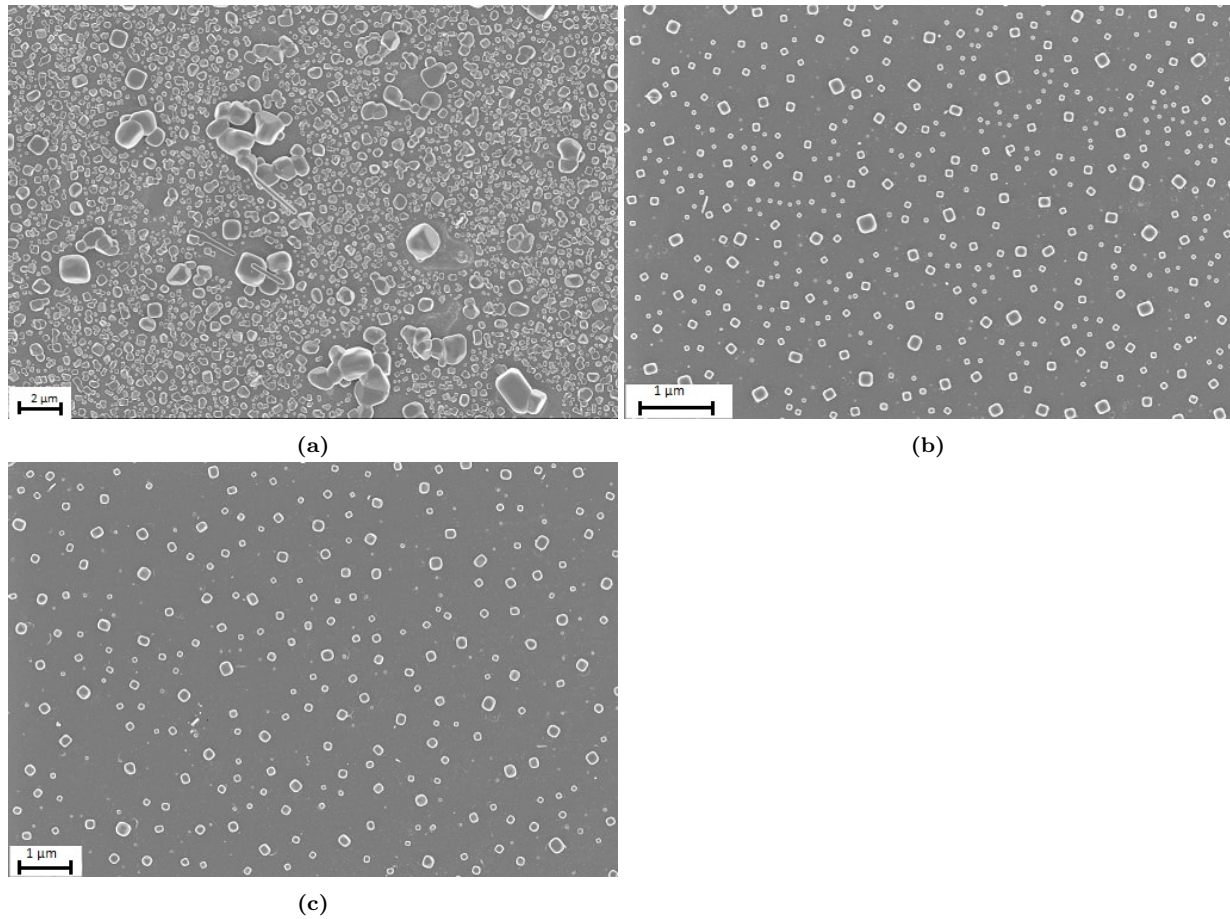
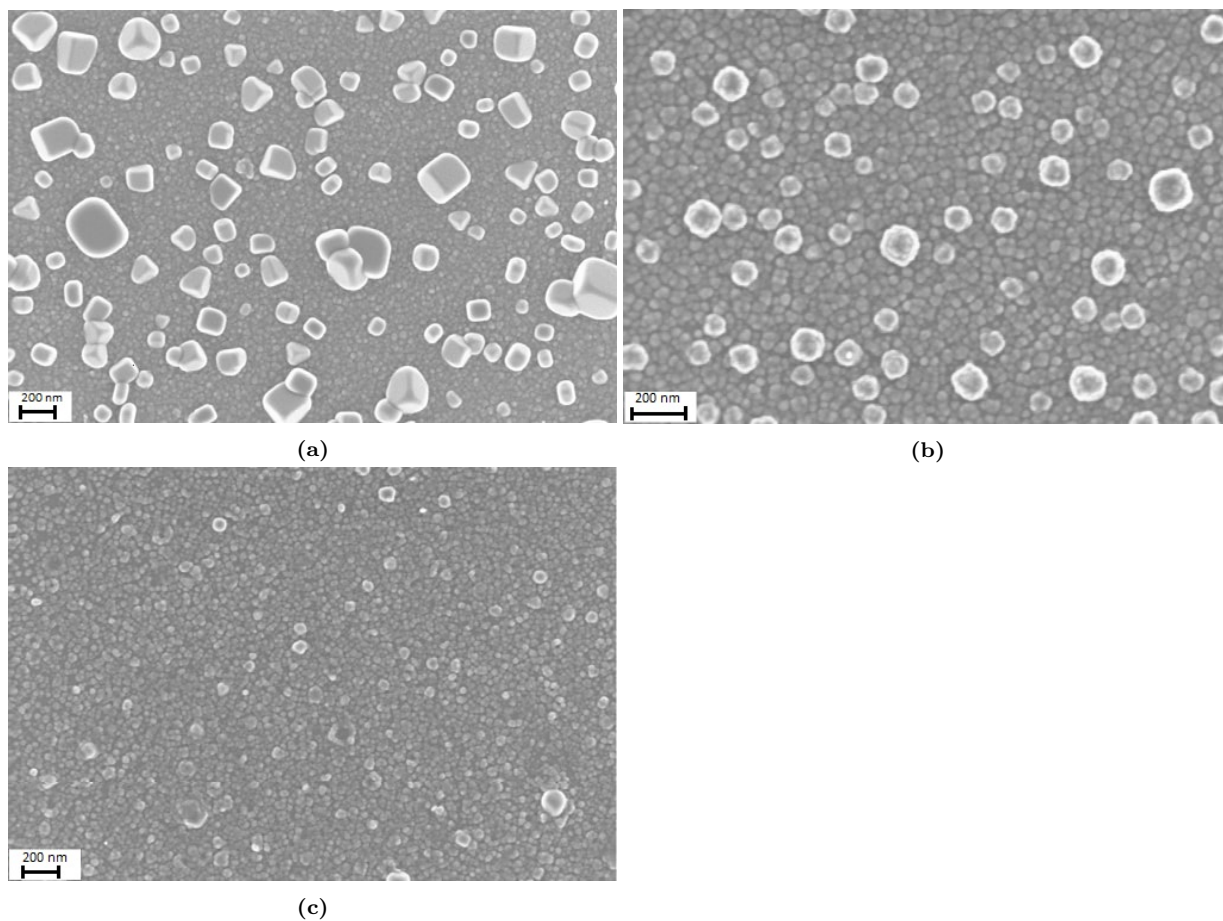


Figure 5.3: SEM micrographs of tin oxide for the (a) undoped (b) 2% and (c) 3% doped samples at micrometer scale)





**Figure 5.4:** SEM micrographs of tin oxide for the (a) undoped (b) 2% and (c) 3% doped samples at nanometer scale.

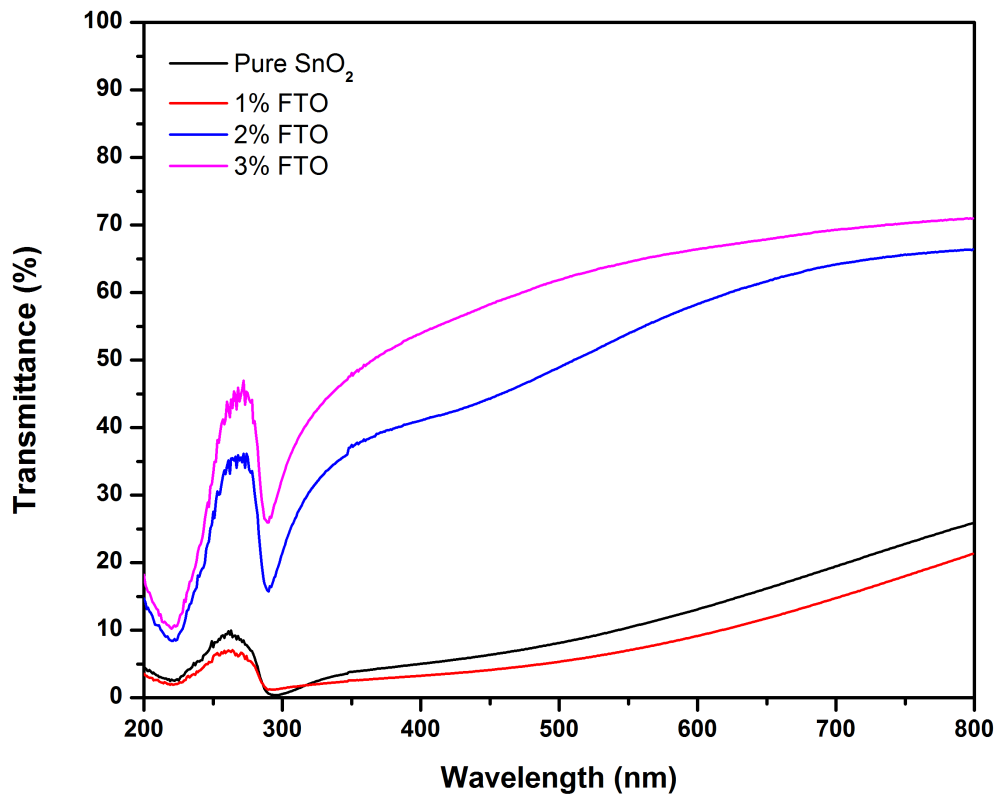


Figure 5.5: UV-Vis spectroscopy of tin oxide at different fluorine doping percentages(at%)

that the first trough in the 290 nm region corresponds to the absorption band edge of the material [75, 76]. It has been found that a dip in this position corresponds to an optical band gap of approximately 3.83 eV. Figure 5.6 is a Tauc plot considering only the 2% and 3% samples, as a different scale was required for the 0% and 1% samples, these can be seen in figure 5.7. Least squares linear fits of the high energy part of the Tauc plots gave the values for the optical band gaps of the 2% and 3% samples as 3.85 eV and 3.87 eV respectively. A band gap value of 3.74 eV was extrapolated for the 0% sample and the 1% sample's high energy part was deemed as not straight enough to make an accurate linear fit.

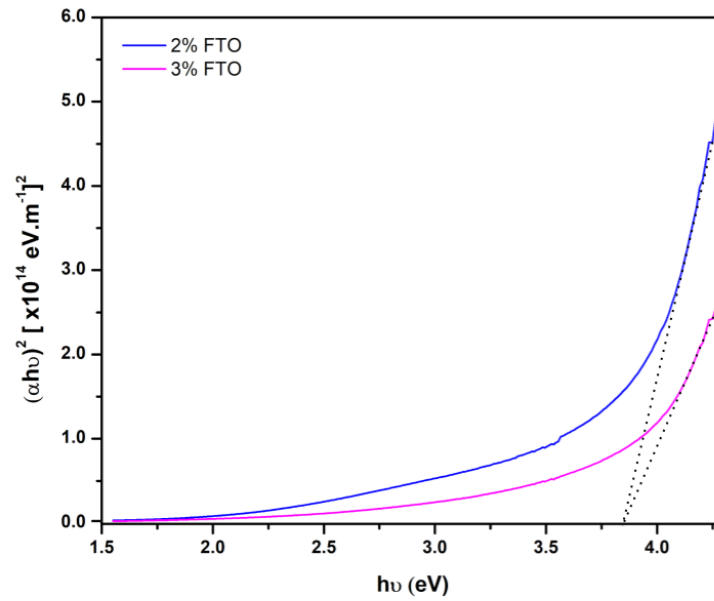


Figure 5.6: Tauc plots of tin oxide at 2% and 3% fluorine doping percentages

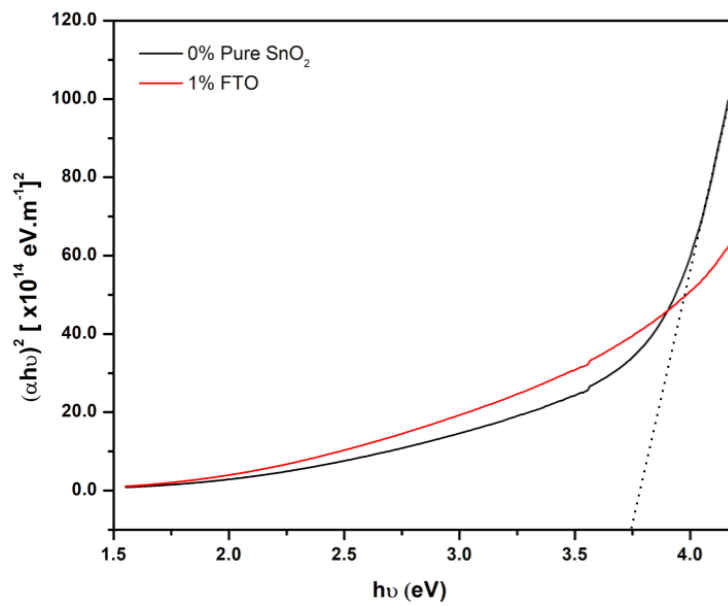


Figure 5.7: Tauc plots of tin oxide at 0% and 1% fluorine doping percentages

### 5.1.4 Four Point Probe

It should be noted that the thickness was approximated as 500 nm since no cross-sectional image could be obtained successfully. In figure 5.8 the resistivity of the undoped, 2% and 3% samples are exhibited. The 1% sample was omitted as its resistivity was overrange of the measurement equipment. The insulating nature of the 1% sample is attributed to the unsuccessful doping of fluorine, as well as its amorphous nature. The undoped sample's resistivity was quite different from measurement to measurement at different locations of the sample, and an average of  $389.57 \Omega.cm^{-1}$  was obtained. For the 2% and 3% samples, there was significantly less variance in measurements at different locations on each sample, and average resistivities were determined to be  $0.37 \Omega.cm^{-1}$  and  $0.55 \Omega.cm^{-1}$ , respectively. The significant decrease in resistivity noticed for the 2% and 3% samples is attributed to the increased charged carriers contributed by the dopant, fluorine.

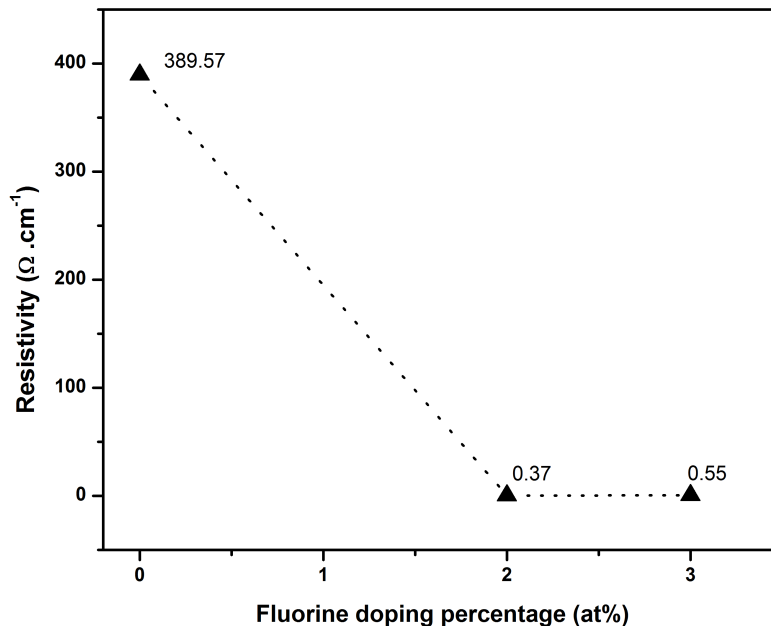


Figure 5.8: Four point probe of tin oxide at different doping levels

### 5.1.5 Conclusion

FTO was successfully, but not optimally, synthesized by sol-gel spin coating, as confirmed by the XRD results showing preferred orientation of crystals growing on the [110] plane and a large amorphous phase from  $15^\circ$  to  $37^\circ$ . The crystallinity decreased with increasing doping due to lattice distortion from substitution sites, whereas the weighted average crystal size increased with increasing doping, most likely due to the decreased agglomeration with increasing doping as observed in SEM. The agglomeration is attributed to tin clustering caused by too high solution concentration, whereas the reduction in agglomeration with doping is probably caused by the smaller ionic radius of fluorine ( $F^{-1}$   $r = 1.33 \text{ \AA}$  and  $O^{-2}$   $r = 1.41 \text{ \AA}$ ) reducing the strain and allowing better crystallization. A polycrystalline morphology was observed between agglomerations at the nanometer scale. The band gaps of 3.85 eV and 3.87 eV obtained for the 2% and 3% samples correspond well to the value of 3.6 eV found in literature. The resistivity decreased from  $389.57 \Omega.cm^{-1}$  for the undoped sample to  $0.37 \Omega.cm^{-1}$  and  $0.55 \Omega.cm^{-1}$  for the 2% and 3% samples, respectively. This is due to introduction of allowed shallow states by the donor (fluorine) in the band gap close to the conduction band, resulting in increased charge carriers (electrons in this case) as these states are thermally ionized at room temperature. The figure of merit obtained for the most impressive sample (the 2% sample) is  $1.25 \times 10^{-6}$ , which is not good enough for use in TCO applications with high end TCOs having a FoM of approximately  $1.06 \times 10^{-2}$ . The main priority in further work should be to increase the transparency, since highly transparent films are required for single molecule Stark spectroscopy applications.

## 5.2 Opto-Electronic Properties of Aluminium Doped Zinc Oxide

### 5.2.1 X-ray Diffraction

Two samples of each doping percentage were measured. The XRD results of each percentage considered in this section are the average of both samples. Figure 5.9 shows the full diffractograms of all doping levels stacked on top of one another, with the standard PDF of zinc oxide included at the bottom. Due to the size of the prominent peaks, it is hard to observe any other features in this figure, figure 5.10 gives a better view of observed features for each diffractogram. Preferred crystal orientation on the [002] plane is observed at all doping levels, indicating growth in the  $c$ -axis direction perpendicular to the substrate surface, similar to what was reported in several other studies with zinc oxide synthesis from solution [77, 78, 79]. Figure 5.10 contains a single diffractogram to showcase that other features were observed in the data. These peaks did not show significant change due to doping. The peaks had average positions of  $31.65^\circ$ ,  $34.33^\circ$ ,  $36.15^\circ$  and  $72.59^\circ$ , corresponding to the [100], [002], [101] and [004] planes, respectively. The peaks were shifted slightly compared to the standard PDF peaks at  $31.77^\circ$ ,  $34.42^\circ$ ,  $36.25^\circ$  and  $72.56^\circ$ . The shift is attributed to the change in lattice parameter due to doping, observed in table 5.2. These findings are in good agreement with the PDF file for zinc oxide (PDF 00-036-1451). These peaks have been indexed to the hexagonal wurtzite crystal structure of zinc oxide. No dopant phases are present in any of the samples, indicating that it was successfully introduced into the lattice.

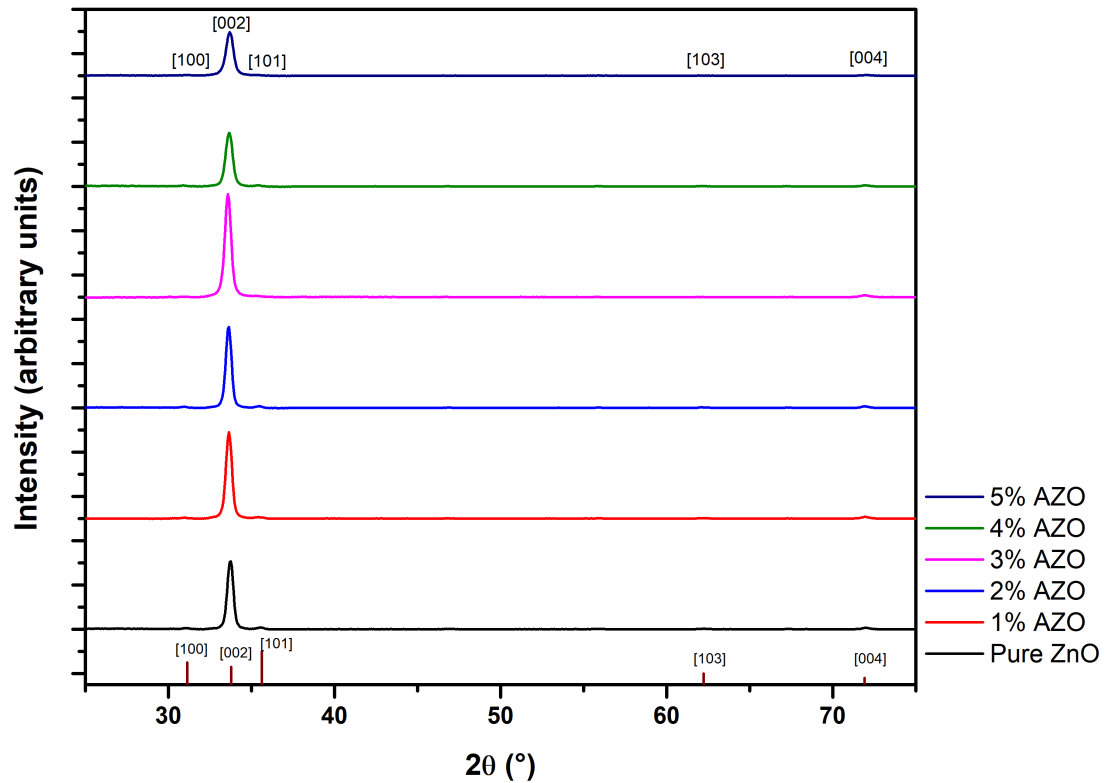


Figure 5.9: XRD of zinc oxide at different atomic aluminium doping percentages, with the standard PDF peaks of zinc oxide included at the bottom.

As it is difficult to compare the sizes of the peaks in figure 5.9, a separate graph was made to show the prominent peaks as a function of doping percentage. This can be seen in figure 5.11. An increase in the [002] peak size of the samples is apparent from 0% up to 3% aluminium doping percentage, after which it decreases substantially for the 4% and 5% percentages.

The intensity of these peaks represents the amount of crystallites found growing on the [002] plane. An increase in this intensity thus represents either increased overall crystallinity of the film (as this peak greatly overshadows all other observed peaks) or increased

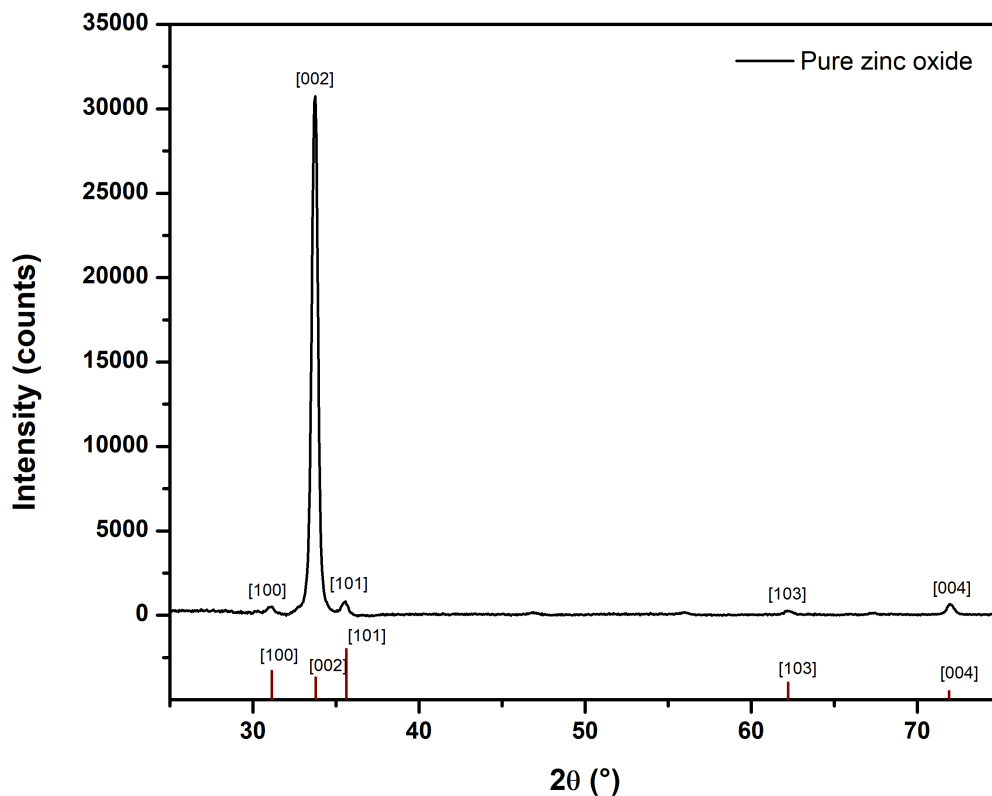


Figure 5.10: XRD of pure zinc oxide, with the standard PDF peaks of zinc oxide included at the bottom.

thickness of the film (increased total amount of crystallites). The thickness of the films were studied with cross-sectional SEM and the findings can be seen in **section 5.2.2**. The peak position, lattice spacing, lattice parameters and FWHM for each doping level are represented in table 5.2.

The percentage crystallinity and average crystal size for each doping percentage were determined as described in the introduction of **section 5.1.1** and are displayed in table 5.3. According to table 5.3 the percentage crystallinity was quite high, starting at 80.27% for the undoped sample and surprisingly increased with doping up to 84.07% for the 3%



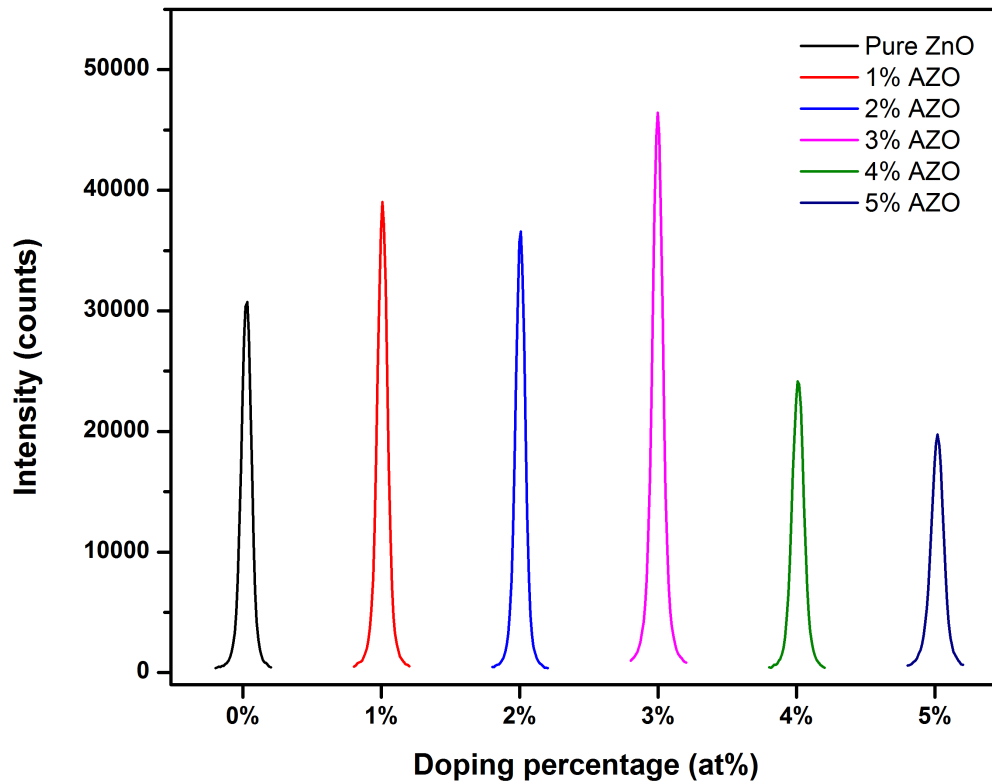


Figure 5.11: Prominent peaks of XRD of zinc oxide at different doping levels

Table 5.2: XRD characteristics of the [002] prominent peak of zinc oxide at different aluminium doping percentages

Doping percentage (at%)	Peak position (°)	Lattice spacing (Å)	Lattice parameters (Å)		FWHM (°)
			a	c	
0	34.4265	2.605	3.248	5.208	0.4285
1	34.3128	2.613	3.258	5.225	0.4249
2	34.3128	2.613	3.259	5.224	0.4070
3	34.2559	2.618	3.260	5.226	0.4437
4	34.3128	2.613	3.260	5.222	0.4956
5	34.3696	2.609	3.256	5.214	0.5195

**Table 5.3: Percentage crystallinity and average crystal size of zinc oxide at different aluminium doping percentages**

Doping percentage (at%)	% Crystallinity	Average crystal size (nm)	Weighted average crystal size (nm)
0	80.27	17.91	20.05
1	83.55	17.08	20.16
2	81.17	18.10	21.02
3	84.07	13.06	19.07
4	79.10	17.69	17.57
5	74.80	13.42	16.47

sample. As the doping increased further, the crystallinity started to decrease down to 79.10% and 74.80% for the 4% and 5% samples, respectively.

At low percentages, the dopant introduces itself into the lattice substitutionally without reducing the crystallinity, as observed with increasing percentage crystallinity up to three percent aluminium doping. The increase in lattice parameters showcased in table 5.2 is attributed to the strain caused by lattice distortion due to change in coordination number leaving unsaturated bonds. The difference in ionic size between Zn ( $r_{Zn^{2+}} = 0.74 \text{ \AA}$ ) and Al ( $r_{Al^{3+}} = 0.54 \text{ \AA}$ ) also increases the lattice distortion and strain.

At high percentages, the decrease in crystallinity is due to excessive doping disturbing the lattice in various ways: the superposition of the distortion caused by substitutional doping centers hinders crystallization; segregation of aluminium oxide from zinc oxide attempting to form a different crystal structure; increased electron carrier concentration from extra valency doping shifts the Fermi energy toward the conduction band and lowers the formation energies of intrinsic defects as shown in figure 3.5. We observe in Figure 5.12 the initial decrease followed by a steady increase of peak breadth (FWHM) due to

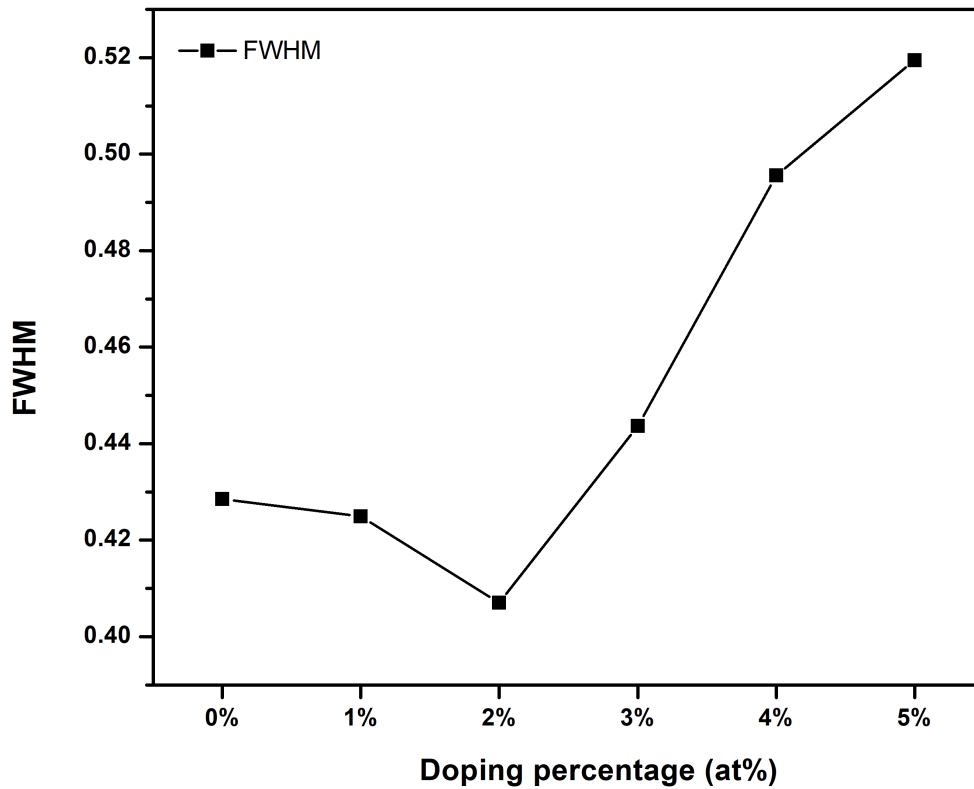


Figure 5.12: Full width half maximum (FWHM) of the prominent peak [002] of zinc oxide at different doping levels

the above-mentioned effects as a function of the doping percentage.

The average crystal size is observed to vary significantly with doping percentage in table 5.3. We believe that this is an unrealistic depiction of what happens physically as the contributions from smaller peaks (approximately 6% of prominent peak for all smaller peaks combined) are considered equal to the contribution of the prominent peak. Only a slight variation in the crystal size is observed for the weighted average crystal size column: it increases from 20.05 nm for the undoped sample to 20.16 nm and 21.02 nm for the 1% and 2% samples, respectively. The average crystal size reduces for the last three

samples with sizes of 19.07 nm, 17.57 nm and 16.47 nm for the 3%, 4% and 5% samples, respectively.

### 5.2.2 Scanning Electron Microscopy

The SEM micrographs at 100 times magnification shown in figure 5.14 exhibit the polycrystalline morphology one would expect to see from the highly crystalline XRD results. The average size of the crystals appears to be relatively similar for undoped, 1% and 2% samples. A reduction in this size is observed for the 3% sample, along with increased density. The reduced focus makes it hard to reliably determine anything significant in the 4% and 5% doping samples. Slight agglomeration was observed in all films at varying concentrations. The undoped, 4% and 5% samples had an extremely low amount, whereas the 1%, 2% and 3% samples had about one noticeable agglomeration per micrograph (at 100 times magnification).

## 5.2. OPTO-ELECTRONIC PROPERTIES OF ALUMINIUM DOPED ZINC OXIDE 101

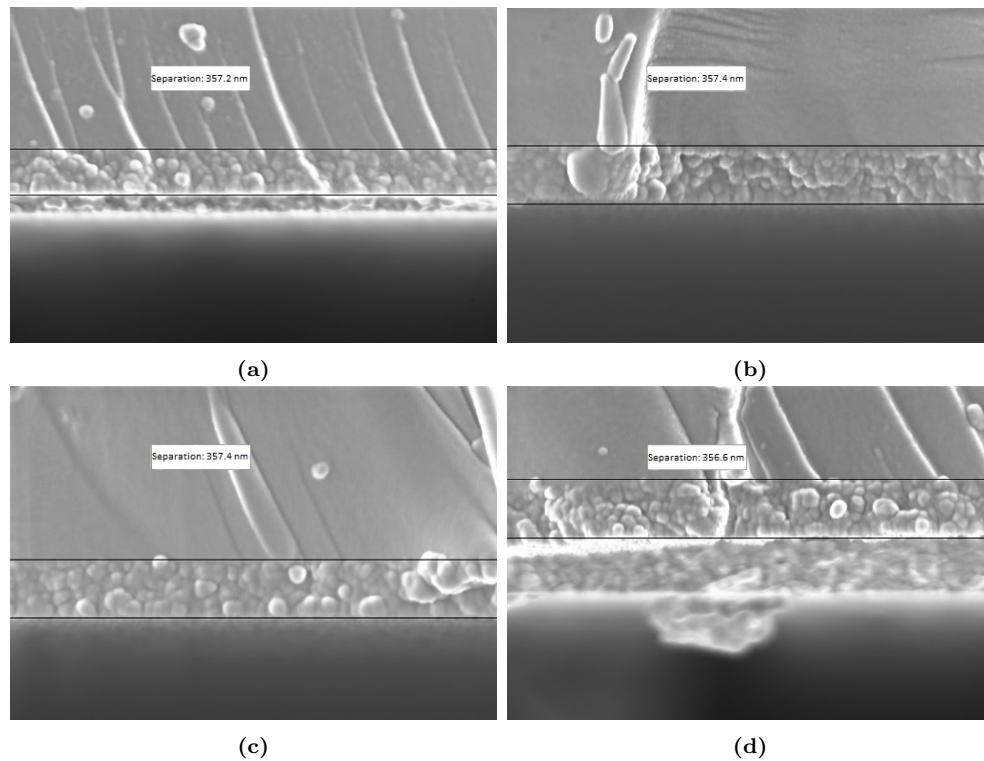


**Figure 5.13:** Cross-section images of the (a) undoped, (b) 1% doped, (c) 3% doped and (d) 4% doped samples

After two separate sessions on the actual samples, we were able to obtain cross-sectional micrographs for the undoped, 1%, 3% and 4% samples. Regrettably, no reliable results could be obtained for the 2% and 5% samples. We observe in figure 5.13 that all films had approximately the same thickness, thus the films experienced no significant variation in thickness due to doping. The average thickness was determined to be  $357 \pm 1$  nm.

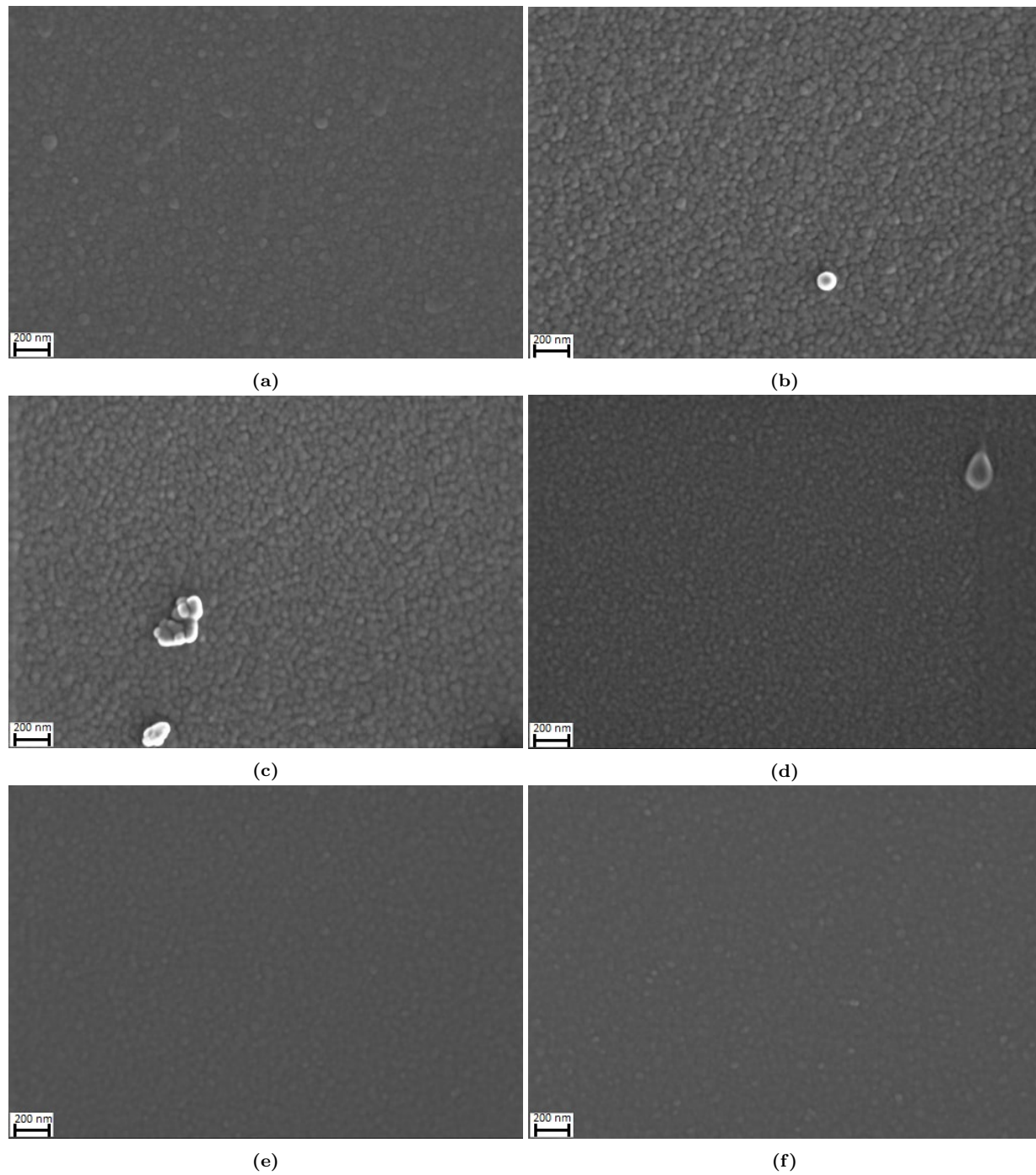


**Figure 5.14:** SEM micrographs of zinc oxide for the (a)undoped, (b)1% doped, (c) 2% doped, (d) 3% doped, (e) 4% doped and (f) 5% doped samples

### 5.2.3 Ultraviolet to Visible Spectroscopy

Similarly to the XRD results, the average of the UV-Vis spectra of the two samples for each doping percentage was used. These are depicted in figure 5.15. The films are all observed as being highly transmitting, with the average transmittance varying between 75 and 80 percent in the visible. The high transmittance is a direct consequence of the wide band of zinc oxide and the high crystallinity observed in XRD.

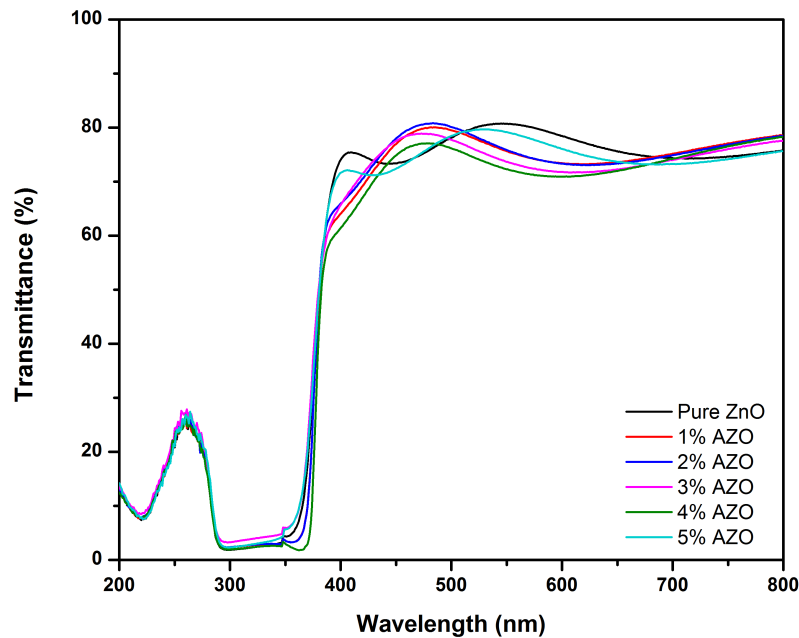


**Figure 5.15:** UV-Vis spectroscopy of zinc oxide at different aluminium doping percentages (*at%*)

From right to left, the spectra have a few regions of interest: in the first region from 800 to 500 nanometers, the transmittance is fairly stable; in the 500 to 350 nanometer range, the transmittance decreases steeply to almost zero, due to the optical band gap; from 350 to 290 nanometers, full absorption of light happens; finally, in the 290 to 220 nanometer

range, a small transmittance 'peak' similar to the one in the tin oxide study is observed. A slight reduction in transmittance is observed as the doping is increased, especially close to the optical band gap region as discussed above. This is caused by the donor introduced shallow states in the band gap as they require less energy to be absorbed.

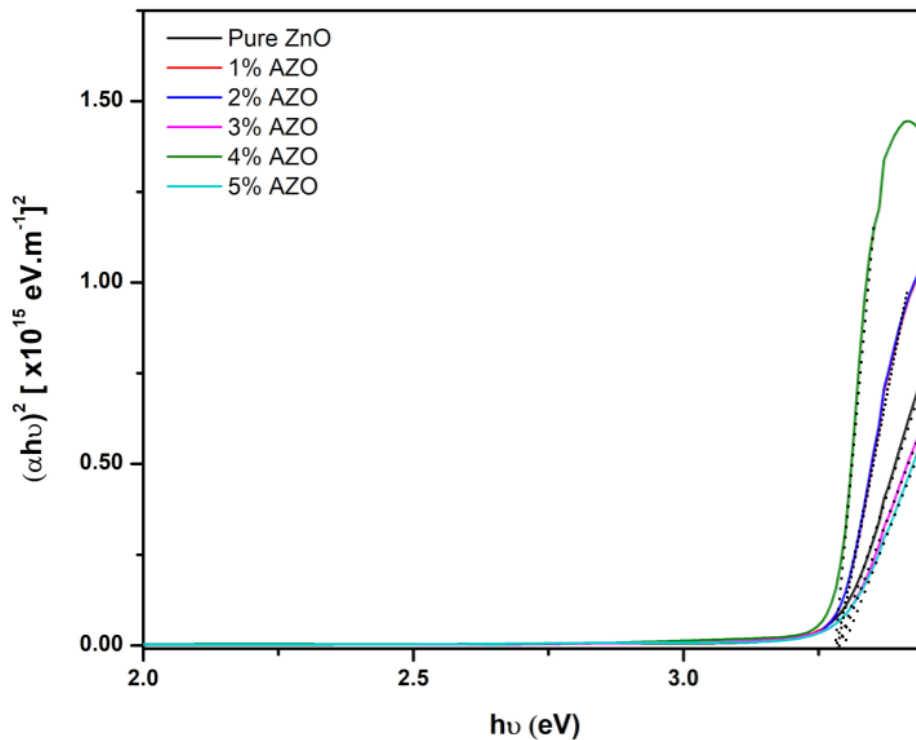


Figure 5.16: Tauc plot of zinc oxide at different aluminium doping percentages(at%)

Using the averaged data of figure 5.15, a Tauc plot was drawn and is shown in figure 5.16. Least-square linear fits of the high energy part of the graphs were made to derive the optical band gaps as a function of atomic doping percentage. The results are displayed in table 5.4. The undoped sample has a band gap of 3.288 eV, in good agreement with the 3.37 eV value found in literature. A decrease in this band gap is observed for the 1%,



2% and 4% samples, as expected due to the shallow donor states. Alternatively, the 3% and 5% samples showcased an increase in the optical band gap. For the 3% sample, this was probably due to increased scattering caused by the higher density of crystal grains observed in SEM, whereas for the 5% sample, it was most likely due to increased ionized impurity scattering centers and plasmonic reflection, as explained in **sections 3.2 and 3.3**.

**Table 5.4: Optical band gap of zinc oxide at different atomic doping percentages**

Doping percentage (at%)	Optical band gap (eV)
0	3.288
1	3.285
2	3.285
3	3.294
4	3.280
5	3.292
Average	3.2873

#### 5.2.4 Four Point Probe

Figure 5.17 shows the resistivity of zinc oxide at different aluminium doping percentages, again averaged over two samples for each doping percentage. A linear decrease in resistivity is observed from  $27.79 \Omega.cm^{-1}$  for the undoped sample to a minimum of  $8.61 \Omega.cm^{-1}$  for the 2% sample, it stays relatively similar for the 3% sample and then rapidly increases for the 4% and 5% samples. The initial decrease in resistivity is attributed to the increase in charge carriers (electrons in this case) provided by the increasing doping percentage, introducing shallow states inside the band gap close to the conduction band,

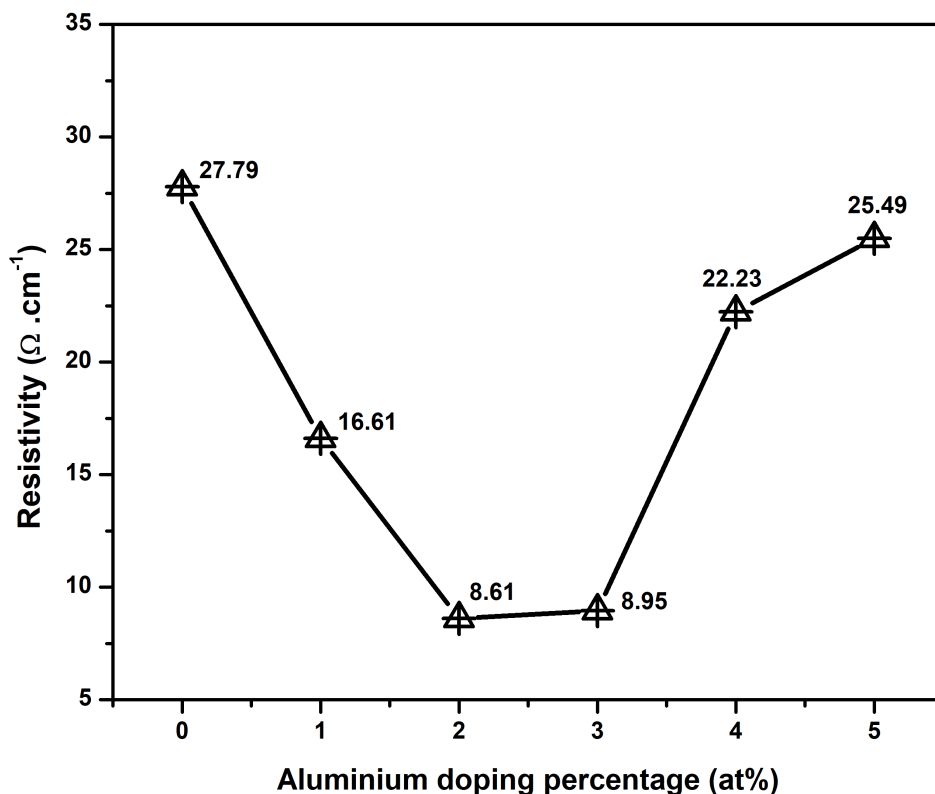
**Resistivity of AZO as a function of aluminium doping percentage**

Figure 5.17: Resistivity of zinc oxide at different aluminium doping percentages(at%)

which are ionized at room temperature. The increase in resistivity can be explained by the reduced mobility of charge carriers, caused by excessive doping disturbing the crystal lattice as seen in XRD. This increases the amount of ionized impurity scattering centers and reduces the average time between collisions in **equation 3.3**. An increase in electron density also results in increased electron-electron scattering.

The very similar optical band gap across all samples but relatively large change in resistivity for the same samples emphasizes the importance of charge carrier mobility in thin film TCOs. The increased crystallinity results in better mobility due to reduced probability of scattering of carriers.

### 5.2.5 Conclusion

Zinc oxide thin films were successfully synthesized with aluminium doping at zero to five percent, as confirmed by XRD agreement with zinc oxide PDF and the band gap correspondence to literature. The best TCO properties were exhibited by the 2% aluminium doped sample, with a high transmittance in the visual spectrum (80%) and a resistivity of  $8.61 \Omega.cm^{-1}$ . These values give a figure of merit of  $1.17 \times 10^{-6}$ , compared to approximately  $1.06 \times 10^{-2}$  for high end commercial TCOs. The synthesized thin films are thus not yet good enough for use as TCO in a Stark cell and further experimentation has to be done to decrease the resistivity. Annealing of films has shown to have a significant impact on the crystalline and resistive properties of thin films [80] and is the logical next step towards a commercial standard TCO. The annealing environment has also been shown to contribute to better resistivity [81]. Optimization of the synthesis procedure can also help decrease resistivity as we have seen that all preparation steps have an impact on the structural and optical properties of thin films [81].

## 5.3 Deposition of Layer Procedure Effect on Zinc Oxide

### 5.3.1 X-ray Diffraction

In figure 5.18 we observe the XRD diffractograms of three samples made with *procedure 1* and *2* on the left and right, respectively. In both cases, preferred crystal orientation is observed on the [002] plane, with *procedure 2* exhibiting significantly greater intensity of the prominent peak.

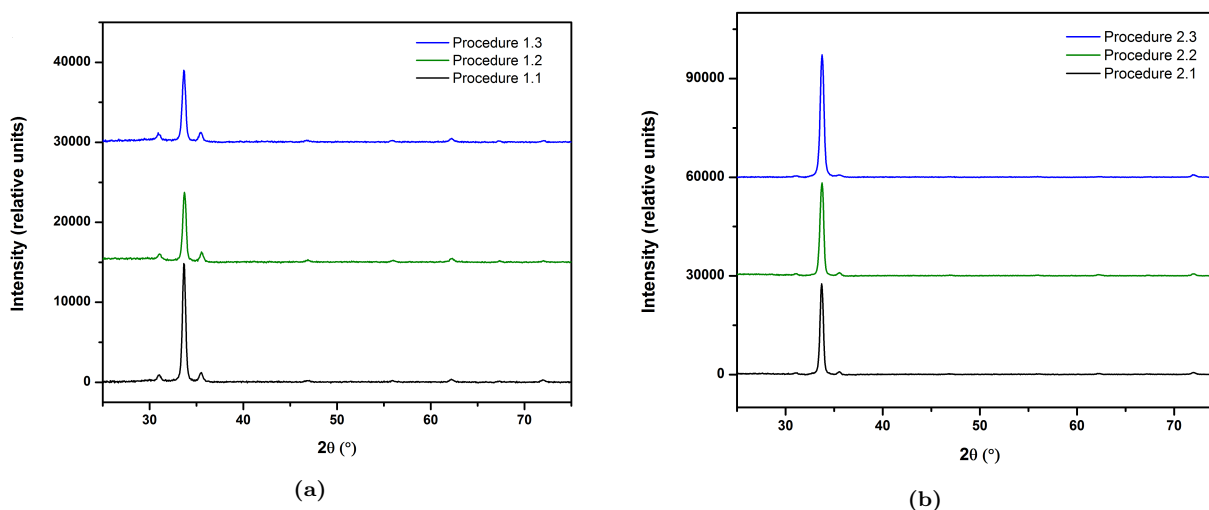


**Figure 5.18:** Xrd of zinc oxide for samples made with the (a) procedure 1 and (b) procedure 2.

The location of the peaks was the same for all samples. Consequently, all samples' lattice parameters were equal at  $a = 5.208 \text{ \AA}$  and  $c = 3.248 \text{ \AA}$ . Similar to the study on aluminium doped zinc oxide, smaller peaks were observed on the [100], [101] and [004] planes, with slight features on the [102], [110], [103] and [112] planes. This is in excellent agreement to the PDF file for zinc oxide (PDF 00-036-1451), with no outside phases or contaminants detected. For better size comparison, the prominent peaks of all samples for each fabrica-

tion procedure were plotted and are showcased in figure 5.19.

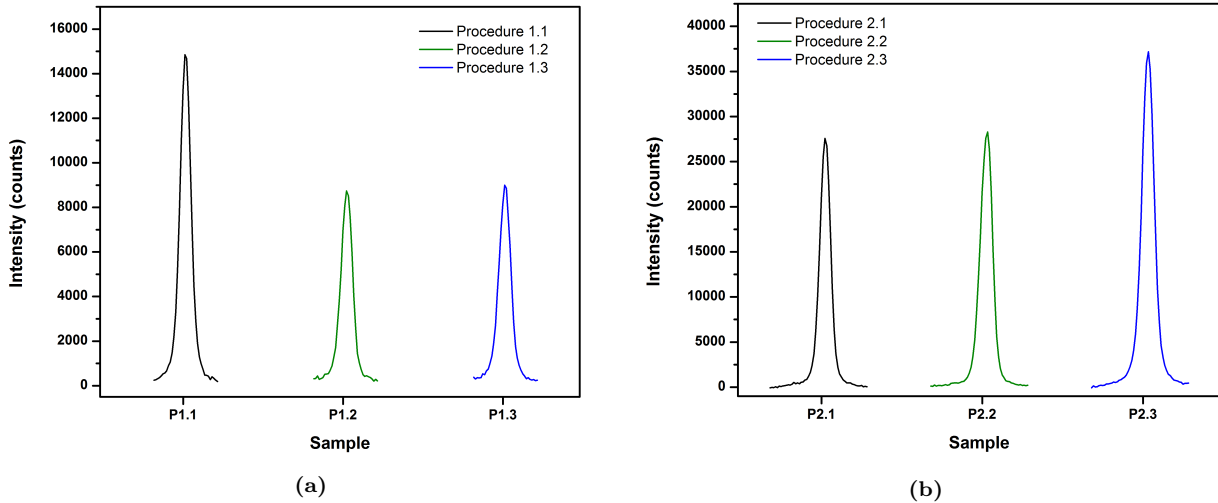


Figure 5.19: XRD of the prominent peaks for samples prepared with (a) *procedure 1* and (b) *procedure 2*.

The average intensity of the prominent peaks for samples fabricated with *procedure 2* was determined to be approximately three times as high as with *procedure 1*. In table 5.5 the

Table 5.5: Percentage crystallinity and average crystal size of zinc oxide at different aluminium doping percentages

Sample	% Crystallinity	Average crystal size (nm)	Weighted average crystal size (nm)
P 1.1	67.84	18.26	20.94
P 1.2	61.72	16.99	18.97
P 1.3	61.91	17.25	18.77
Average	63.823	17.500	19.300
P 2.1	77.63	19.81	21.93
P 2.2	78.89	17.75	19.37
P 2.3	83.16	15.01	19.11
Average	79.893	17.523	20.137

average percentage crystallinity was determined to be 63.83% and 79.89% for *procedure 1* and *2* respectively, showing significantly higher crystallinity for samples prepared with

*procedure 2*. The weighted average crystal size of *procedure 2* samples is also slightly higher at 20.137 nm compared to 19.300 nm for *procedure 1* samples.

### 5.3.2 Scanning Electron Microscopy

Figure 5.20 exhibits the highly ordered polycrystalline morphology of the films obtained with both fabrication procedures. *Procedure 1* samples on the left ( $a - c$ ) are observed as slightly less uniform than *procedure 2* samples on the right ( $d - f$ ), with slight deviations visible in samples ( $a$ ) and ( $c$ ). No clear difference in crystal sizes can be proclaimed from the figure.

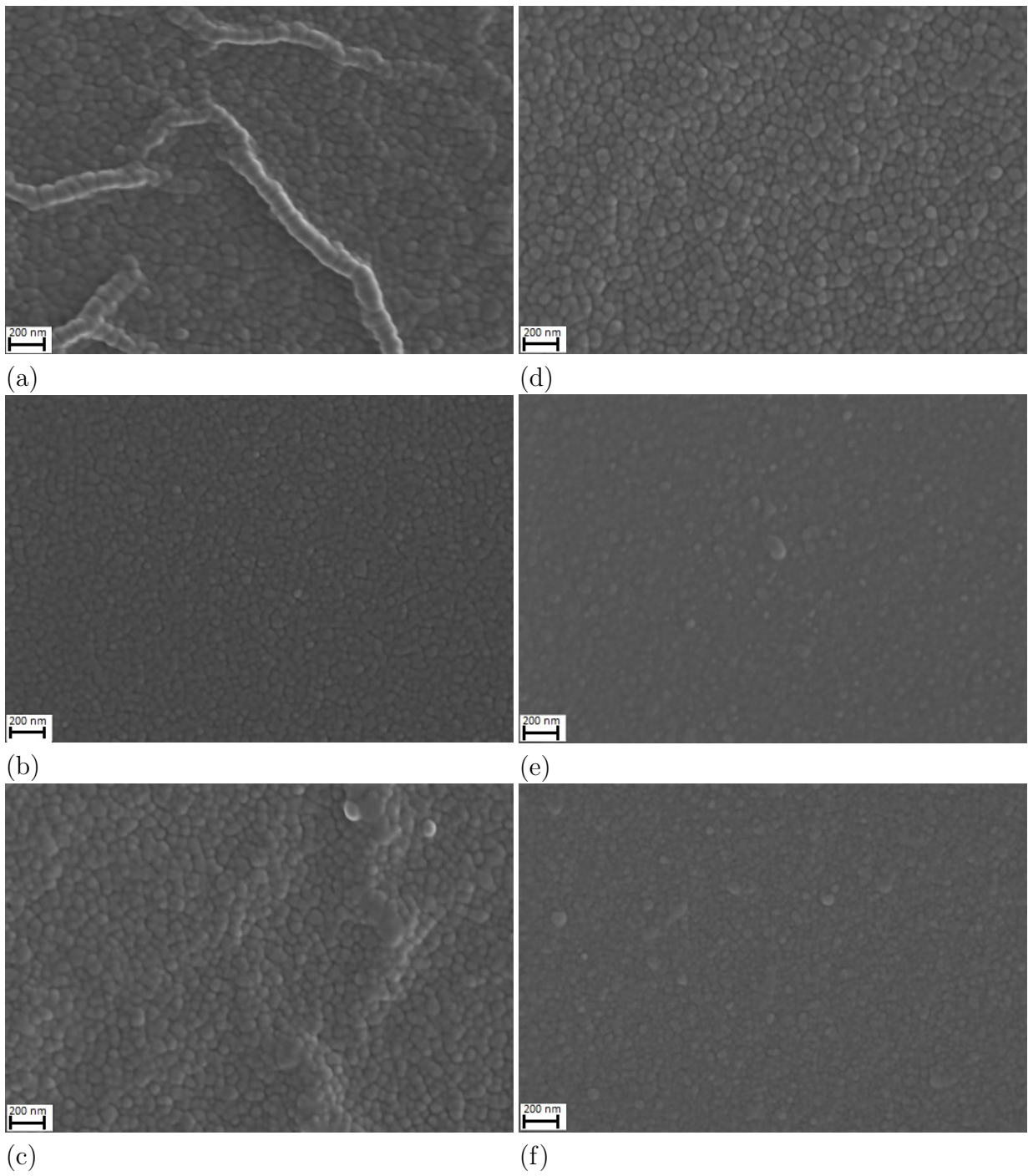


Figure 5.20: SEM micrographs of samples obtained with the (a-c) procedure 1 and (d-f) procedure 2.

### 5.3.3 Ultraviolet to Visible Spectroscopy

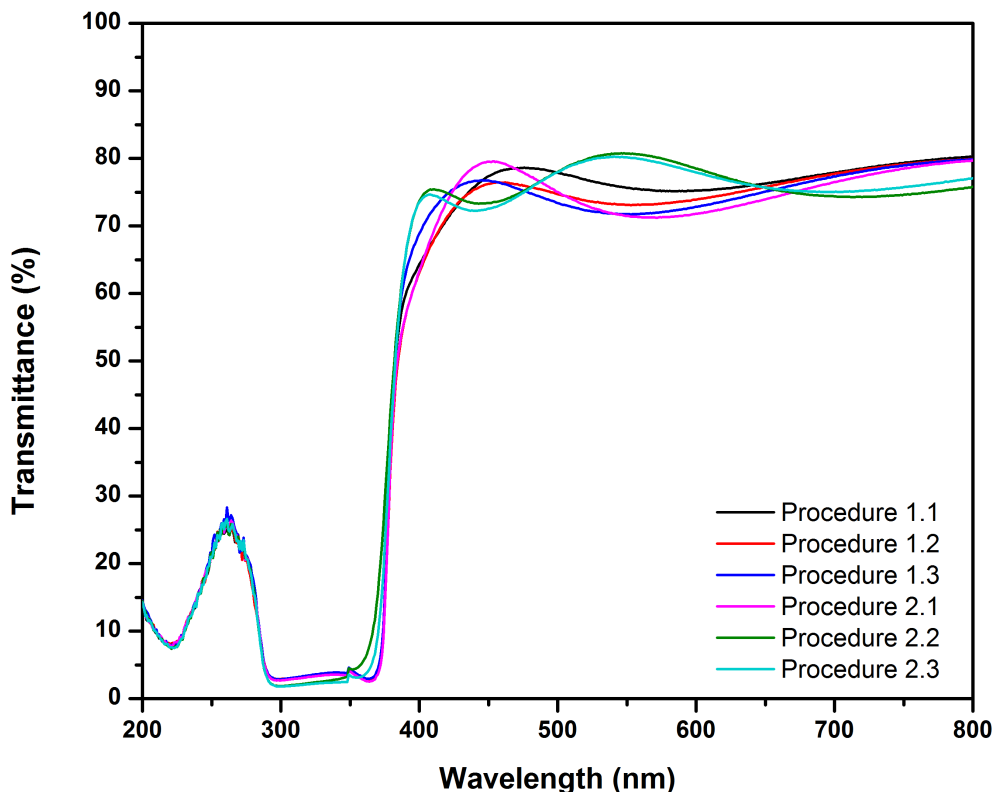


Figure 5.21: UV-Vis spectroscopy of zinc oxide at different aluminium doping percentages(at%)

The UV-Vis spectra of the samples obtained with fabrication procedures 1 and 2 are presented in figure 5.21. Four distinct regions can be observed from right to left: from 800 nm to 450 nm, all samples exhibit high ( $> 70\%$ ) transmittance; in the 450 nm to 350 nm region, the transmittance rapidly decreases as the light now has enough energy to be absorbed and excite electrons across the band gap into the conduction band; from 300 nm to 290 nm, almost all light is absorbed by the samples and a transmittance of  $< 5\%$  is observed; in the last region, from 290 nm to 200 nm, a small transmittance peak is present



similar to what was observed in the fluorine doped tin oxide and aluminium doped zinc oxide studies' UV-Vis spectra.

It appears that the higher order of crystallinity observed in the XRD of *procedure 2* samples does not relate to significantly increased transparency, as the transparency is relatively similar for all samples across the measured spectrum and the higher transparency varies for different regions of the spectrum. *Procedure 2* samples 2 and 3 also have a slightly different shape than the rest of the samples. This has been observed in various other studies but is never acknowledged or explained [82, 78, 80]. Tauc plots were constructed

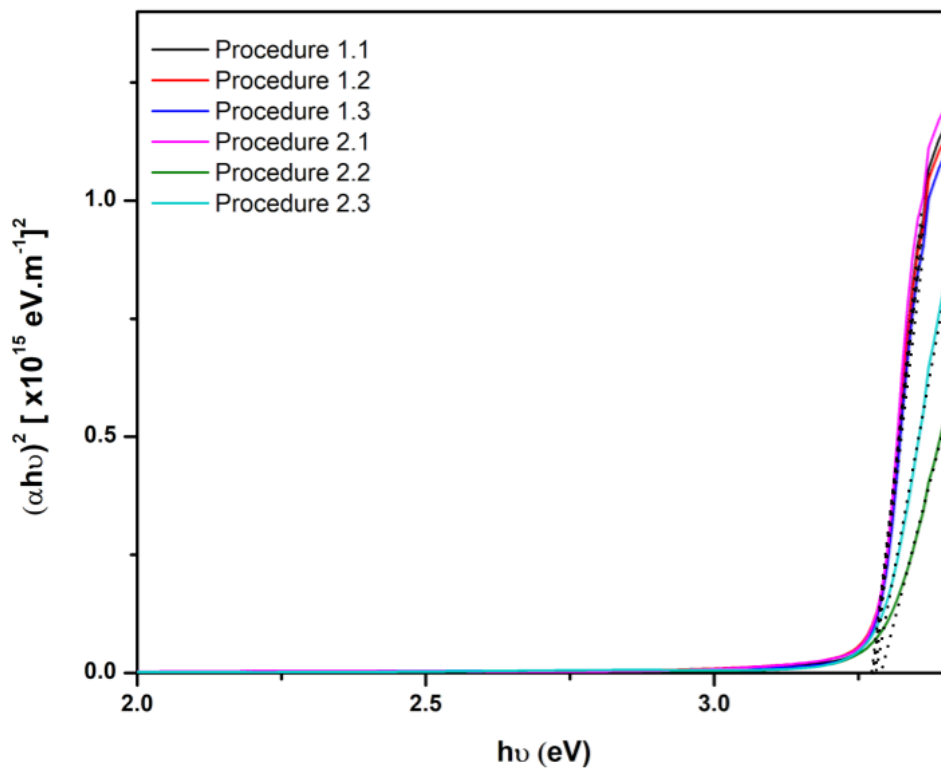


Figure 5.22: Tauc plots of zinc oxide at different aluminium doping percentages(at%)

from the UV-Vis spectroscopy data and are shown in figure 5.22. Least-square linear fits

of the high energy part of the different plots were done with graphing software to obtain the optical band gaps of the various samples. These estimated values are shown in table 5.6. We observe that the band gap values for the *P 1.1*, *P 1.2*, *P 1.3* and *P 2.1* samples are all extremely similar, with slightly higher values for the *P 2.2* and *P 2.3* samples. We believe that the observed change in band gap for the last two samples is due to the unexplained different shape their UV-Vis spectra had near the absorption band edge. The average optical band gaps of 3.2783 eV and 3.2843 eV obtained for *procedure 1* and 2 respectively indicate that there is no significant optical advantage to either procedure.

**Table 5.6: Optical band gap of zinc oxide for different fabrication techniques**

Sample	Optical band gap (eV)
P 1.1	3.278
P 1.2	3.278
P 1.3	3.279
Procedure 1 average	3.2783
P 2.1	3.277
P 2.2	3.290
P 2.3	3.286
Procedure 2 average	3.2843

### 5.3.4 Four Point Probe

All samples fabricated with *procedure 1* produced overrange voltage data on the four point probe instrument, meaning that the samples are highly resistive (minimum of approximately  $390 \Omega.cm^{-1}$ , as this was the highest value I obtained during my various experiments). *Procedure 2* samples had resistivities of  $28.13 \Omega.cm^{-1}$ ,  $38.45 \Omega.cm^{-1}$  and  $16.79 \Omega.cm^{-1}$  for sample 1, 2 and 3, respectively, resulting in an average of  $27.790 \Omega.cm^{-1}$ .

### 5.3.5 Conclusion

Synthesis of zinc oxide thin films was successfully achieved with both *procedure 1* and *2*, as confirmed by the XRD data that were consistent with standard powder diffraction files (PDFs) for zinc oxide. The different procedures had no significant effect on the crystal orientation as all films showed preferential growth on the [002] plane. Prominent peaks measured from samples of *procedure 2* had greater intensity when compared to samples of *procedure 1*, culminating in greater calculated crystallinity for *procedure 2* samples.

Higher quality of *procedure 2* films is also suggested by the SEM micrographs, with more deviations present in *procedure 1* samples. The *deposition of layer procedure* had no significant impact on the optical properties of the films, with the observed difference in the UV-Vis spectra explained by the shape anomaly. *Procedure 2* samples had a significantly lower resistivity than *procedure 1* samples, with *procedure 1* samples having at least fourteen times higher resistivity. The resistivity difference can be explained by the reduced scattering in increased crystallinity samples, as well as the better fusion between layers allowed by *procedure 2*.

In conclusion, *procedure 2* is significantly more advantageous for TCO production when compared to *procedure 1*, since the optical properties are similar, however *procedure 2* exhibits better electronic properties.



# Chapter 6

## Conclusion

In this research project, we aimed to close the gap towards the possibility of doing single molecule Stark spectroscopy on various samples, mainly light harvesting complex II (LHCII) of plants. This would hopefully shed light on newly observed dark states observed when LHCII is immobilized with an electrokinetic trap and would also indicate whether some spectral states occur due to the presence of charge-transfer states or radical states.

Stark spectroscopy requires an optically transparent Stark cell, for which transparent conducting oxides (TCOs) have to be used. Due to the optical requirements of the single molecule spectroscopy (SMS) setup, a specific microscope slide thickness is necessary, of which no commercial TCO version was available. We decided to make our own TCO with the top options being indium tin oxide (ITO), fluorine doped tin oxide (FTO) and aluminium doped zinc oxide. Since indium is an expensive material with weak thermostability, the second most popular commercial TCO, FTO, was selected for the first TCO synthesis attempt.

In the *Opto-Electronic Properties of Fluorine Doped Tin Oxide* study in **section 5.1**

we could only produce low optical quality (blackish) films. They were confirmed to be FTO by X-ray diffraction's (XRD) agreement to the powder diffraction file (PDF) for tin oxide, as well as the average band gap correlation to literature at 3.860 eV. From SEM micrographs we learned that the low optical quality was caused by agglomeration of tin on the surface of the films due to too high tin concentration in the spin coating solution. The films had good resistivity with a minimum of  $0.37 \Omega.cm^{-1}$ , however, the low transmittance observed with UV-Vis spectroscopy at 500 nm resulted in a figure of merit (FOM) not suitable for TCO applications.

In the *Opto-Electronic Properties of Aluminium Doped Zinc Oxide* study in **section 5.2** we successfully synthesized aluminium doped zinc oxide (AZO), as confirmed by XRD's agreement to zinc oxide's PDF and the average calculated band gap's correlation to literature at 3.2873 eV. SEM and UV-Visible spectroscopy showcased polycrystalline morphology and good optical quality respectively. The resistivity was positively influenced by doping as desired, however the minimum resistivity of  $8.61 \Omega.cm^{-1}$  resulted in a FOM too low for TCO applications, but better than the FOM obtained in the FTO study.

In the *Deposition of Layer Procedure Effect on Zinc Oxide* study in **section 5.3**, zinc oxide was successfully synthesized with *procedure 1* and *procedure 2*, as confirmed by XRD's agreement to zinc oxide's PDF and average band gap's correlation to literature. No significant variation in optical properties due to different deposition of layer procedures was observed. On the contrary, *procedure 2* exhibited significantly lower resistivity, and is thus more suited for low cost spin coating fabrication of TCOs.

"Can we synthesize our own transparent conducting thin films with sufficient quality for use in single molecule Stark spectroscopy?". The FOMs obtained in the studies were not

sufficient for use in Stark SMS applications, however, there is definite progress toward the required level. Additionally, the three studies we did in this research project suggested many adjustments that can be made in future work to improve the quality of the films. Reducing the tin concentration of the tin oxide solution and using *procedure 2* to deposit the thin films should have a significant impact on both the transparency and resistivity of FTO. Annealing of films has been observed to reduce the resistivity to a significant degree. A second annealing treatment in a gaseous environment such as nitrogen [81] and hydrogen [83] has also shown to reduce the resistivity substantially. Combining *procedure 2* with various post annealing treatments is thus a very promising possibility.





# Appendix

## Stark Effect and the Stark Cell

The beginning of my Master's research project was spent learning about Single Molecule Spectroscopy and extending the technique to include the capability of studying the Stark effect. The first step of this was designing or choosing an existing Stark cell.

A Stark cell is the name given to the sample holder that has all the necessary components to apply the desired electric field over your sample at the time of measurement without hindering the optical capability of the measurement technique to the extent that the results are not usable. In other words, the Stark cell has to consist of glass slides coated with a material that has high optical transparency and high electrical conductivity. It is possible to achieve this with only one coated slide as there is the option of using a metal plate as the far side plate as no light needs to pass through it.

### Separator Design

Since it is required to suspend LHCII samples on a glass slide through coating with poly-L-Lysine (PLL), the simplest solution would be to use the PLL coating and liquid carrying the LHCII's as the insulating layer required for the electric field. This simple plan comes with a couple of drawbacks: the thickness between the two electrodes would not be accu-

rately determinable or controllable; the two electrodes might come into contact at some point resulting in a circuit short; it would be hard to reliably reproduce the exact same measuring conditions for subsequent samples.

As the aforementioned Stark cell did not seem very appealing due to its drawbacks, some other designs were made/looked at:

For one cell, a circular cut of teflon as a spacer with a gap in the middle was proposed. It would rest on the front electrode with the back electrode on top and the sample dispensed in the middle. The drawback of this method is that teflon becomes extremely brittle and fragile at thicknesses less than 1 mm and a spacing of 1 mm would require a very large voltage to be applied in order to create an electric field with desired strength of 1 MV/cm, for instance:

$$E = \frac{V}{d}$$

$$V = Ed \text{ using } d = 1\text{mm and } E = 1\text{MV/cm}$$

$$V = 100\text{kV}$$

It is possible to get this required voltage down to 0.66x100kV by designing a 1 mm thick teflon square such that the electrodes can fit inside it and attaching the back electrode to a material wide enough to rest on the spacer with the back electrode suspended inside it. This allows the gap between the electrodes to be reduced by double the thickness of the glass slides, 0.17mm. Reducing this gap even further would be trivial as one could simply add more uncoated glass slides between the material and the final coated slide.

Another method considered to reduce the gap between the plates was to put the coated side of the glass slides on the outside, or rather, facing away of the sample sandwiched in the middle. This would create a gap of approximately double the thickness of the slides,

previously mentioned to be 0.17 mm, at 0.34 mm, reducing the required voltage even further to  $0.34 \times 100\text{kV}$ .

This would be possible as a dielectric only influences the electric field inside of it.

(note for Abrie: reference (check) <http://bolvan.ph.utexas.edu/vadim/Classes/15s/dielectrics.pdf>)

If an electric field is applied between two parallel plates, with the field flowing from the positively- to the negatively charged plate, a dielectric placed in this electric field becomes polarized, with positive charge carriers collecting at the negative plate, and the negative charge carriers collecting at the opposite side. This creates an internal electric field that cancels out a portion of the external field, reducing the field strength inside (and only inside) the dielectric. The amount by which a specific dielectric reduces an electric field is a material property known as relative permittivity,  $\kappa$ .

After doing some more research, a few papers were discovered where double sided sticky tape is solely used as a spacer. This can reduce the space between the electrodes to the scale of microns, resulting in a significant reduction in the voltage required to apply a desirable electric field.



# Bibliography

- [1] K Higgins. Economic growth and sustainability - are they mutually exclusive, 2013.
- [2] Renewable Energy Policy Network. Global status report, 2019.
- [3] J.L. Botha. *Using single molecule spectroscopy to study fast photoprotective processes in plants*. PhD thesis, University of Pretoria, 2016.
- [4] Nonlinear optics white light continuum. <http://www.nlo.hw.ac.uk/node/8>. Accessed: 2018-09-10.
- [5] I. Gris-Sánchez, D. Van Ras, and T. A. Birks. The Airy fiber: an optical fiber that guides light diffracted by a circular aperture. *Optica*, 3(3):270–276, Mar 2016.
- [6] E.G. Loewen and E. Popov. *Diffraction Gratings and Applications*. Optical Science and Engineering. Taylor & Francis, 1997.
- [7] J S Foster. Some leading features of the Stark effect. *Journal of the Franklin Institute*, 209(5):585–624, 1930.
- [8] W.A. Harrison. *Electronic Structure and the Properties of Solids: The Physics of the Chemical Bond*. Dover Books on Physics. Dover Publications, 2012.
- [9] A.R. West. *Solid State Chemistry and its Applications*. Wiley, 2014.
- [10] Bo E Sernelius, K-F Berggren, Z-C Jin, I Hamberg, and CG Granqvist. Band-gap tailoring of ZnO by means of heavy Al doping. *Physical Review B*, 37(17):10244, 1988.
- [11] Çetin Kılıç and Alex Zunger. Origins of coexistence of conductivity and transparency in SnO<sub>2</sub>. *Physical Review Letters*, 88(9):095501, 2002.
- [12] Anderson Janotti and Chris G Van de Walle. Native point defects in ZnO. *Physical Review B*, 76(16):165202, 2007.

- [13] Christian Leth Petersen, Francois Grey, and Peter Boggild. Multi-point probe, January 29 2008. US Patent 7,323,890.
- [14] Scanning electron microscope. [https://en.wikipedia.org/wiki/Scanning\\_electron\\_microscope](https://en.wikipedia.org/wiki/Scanning_electron_microscope). Accessed: 2018-06-26.
- [15] Askari Mohammad Bagher, Mirzaei Mahmoud Abadi Vahid, and Mirhabibi Mohsen. Types of solar cells and application. *American Journal of optics and Photonics*, 3(5):94–113, 2015.
- [16] V V Grigor'yants, V I Smirnov, and Yu K Chamorovskiĭ. Generation of wide-band optical continuum in fiber waveguides. *Soviet Journal of Quantum Electronics*, 12(7):841, 1982.
- [17] H Takara, T Ohara, T Yamamoto, H Masuda, M Abe, H Takahashi, and T Morioka. Field demonstration of over 1000-channel DWDM transmission with supercontinuum multi-carrier source. *Electronics Letters*, 41(5):270–271, 2005.
- [18] C Dunsby, PMP Lanigan, J McGinty, DS Elson, J Requejo-Isidro, I Munro, N Galletly, F McCann, B Treanor, Björn Önfelt, et al. An electronically tunable ultrafast laser source applied to fluorescence imaging and fluorescence lifetime imaging microscopy. *Journal of Physics D: Applied Physics*, 37(23):3296, 2004.
- [19] DJ McCarron. A guide to acousto-optic modulators. *Internet: <http://massey.dur.ac.uk/resources/slcornish/AOMGuide.pdf>*, 2007.
- [20] E. I. Gordon. A review of acoustooptical deflection and modulation devices. *Appl. Opt.*, 5(10):1629–1639, Oct 1966.
- [21] J.R. Lakowicz. *Principles of Fluorescence Spectroscopy*. Springer US, 2007.
- [22] Lord Rayleigh F.R.S. Xxxi. investigations in optics, with special reference to the spectroscope. *The London, Edinburgh, and Dublin Philosophical Magazine and Journal of Science*, 8(49):261–274, 1879.
- [23] Bart Van Zeghbroeck. Principles of semiconductor devices. *Colorado University*, 34, 2004.
- [24] Edward M.D. Fisher. Principles and early historical development of silicon avalanche and Geiger-Mode photodiodes. In Nikolay Britun and Anton Nikiforov, editors, *Photon Counting*, chapter 1. IntechOpen, Rijeka, 2018.
- [25] S. Cova, M. Ghioni, A. Lacaita, C. Samori, and F. Zappa. Avalanche photodiodes and quenching circuits for single-photon detection. *Appl. Opt.*, 35(12):1956–1976, Apr 1996.

- [26] Tjaart PJ Krüger, Cristian Iliaia, Leonas Valkunas, and Rienk van Grondelle. Fluorescence intermittency from the main plant light-harvesting complex: sensitivity to the local environment. *The Journal of Physical Chemistry B*, 115(18):5083–5095, 2011.
- [27] Tjaart PJ Krüger, Cristian Iliaia, Matthew P Johnson, Alexander V Ruban, Emmanouil Papagiannakis, Peter Horton, and Rienk van Grondelle. Controlled disorder in plant light-harvesting complex ii explains its photoprotective role. *Biophysical journal*, 102(11):2669–2676, 2012.
- [28] Gabriela S Schlau-Cohen, Hsiang-Yu Yang, Tjaart PJ Krüger, Pengqi Xu, Michal Gwizdala, Rienk Van Grondelle, Roberta Croce, and WE Moerner. Single-molecule identification of quenched and unquenched states of LHCII. *The Journal of Physical Chemistry letters*, 6(5):860–867, 2015.
- [29] P. Drude. Zur Elektronentheorie der Metalle. *Annalen der Physik*, 306(3):566–613, 1900.
- [30] D.J. Griffiths. *Introduction to Quantum Mechanics*. Cambridge University Press, 2016.
- [31] N.W. Ashcroft and N.D. Mermin. *Solid State Physics*. HRW international editions. Holt, Rinehart and Winston, 1976.
- [32] Anders Hallén and Mietek Bakowski. Combined proton and electron irradiation for improved GTO thyristors. *Solid-state electronics*, 32(11):1033–1037, 1989.
- [33] Y. Sakamoto, H. Tanaka, F.A. Lewis, X.Q. Tong, and K. Kandasamy. “uphill” hydrogen diffusion effects of hydrogen interstitial strain gradients in palladium and palladium alloys. *International Journal of Hydrogen Energy*, 21(11):1025 – 1032, 1996.
- [34] Brian G Lewis and David C Paine. Applications and processing of transparent conducting oxides. *MRS bulletin*, 25(8):22–27, 2000.
- [35] Ivar Hamberg and Claes G Granqvist. Evaporated Sn-doped  $\text{In}_2\text{O}_3$  films: Basic optical properties and applications to energy-efficient windows. *Journal of Applied Physics*, 60(11):R123–R160, 1986.
- [36] K Badeker. *Annals of Physics*, 22:749, 1907.
- [37] Akshay Kumar and Chongwu Zhou. The race to replace tin-doped indium oxide: Which material will win? *ACS Nano*, 4(1):11–14, 2010. PMID: 20099909.
- [38] David Ferry. *Semiconductor transport*. CRC Press, 2000.
- [39] Matthias Batzill and Ulrike Diebold. The surface and materials science of tin oxide. *Progress in surface science*, 79(2-4):47–154, 2005.

- [40] Adrian A Bolzan, Celesta Fong, Brendan J Kennedy, and Christopher J Howard. Structural studies of rutile-type metal dioxides. *Acta Crystallographica Section B*, 53(3):373–380, 1997.
- [41] D. A. H. Hanaor, W. Xu, M. Ferry, and C. C. Sorrell. Abnormal grain growth of rutile  $\text{TiO}_2$  induced by  $\text{ZrSiO}_4$ . *Journal of Crystal Growth*, 359:83–91, November 2012.
- [42] J Robertson. Electronic structure of  $\text{SnO}_2$ ,  $\text{GeO}_2$ ,  $\text{PbO}_2$ ,  $\text{TeO}_2$  and  $\text{MgF}_2$ . *Journal of Physics C: Solid State Physics*, 12(22):4767, 1979.
- [43] C Terrier, JP Chatelon, R Berjoan, and JA Roger. Sb-doped  $\text{SnO}_2$  transparent conducting oxide from the sol-gel dip-coating technique. *Thin solid films*, 263(1):37–41, 1995.
- [44] Hans Hartnagel, AL Dawar, AK Jain, and Cand Jagadish. *Semiconducting transparent thin films*. Institute of Physics Bristol, 1995.
- [45] Hisahito Ogawa, Masahiro Nishikawa, and Atsushi Abe. Hall measurement studies and an electrical conduction model of tin oxide ultrafine particle films. *Journal of Applied Physics*, 53(6):4448–4455, 1982.
- [46] Bertil Stjerna, Claes G Granqvist, Agneta Seidel, and Lennart Häggström. Characterization of rf-sputtered  $\text{SnO}_x$  thin films by electron microscopy, Hall-effect measurement, and Mössbauer spectrometry. *Journal of applied physics*, 68(12):6241–6245, 1990.
- [47] KB Sundaram and GK Bhagavat. High-temperature annealing effects on tin oxide films. *Journal of Physics D: Applied Physics*, 16(1):69, 1983.
- [48] C Stampfl, CG Van de Walle, D Vogel, P Krüger, and J Pollmann. Native defects and impurities in InN: First-principles studies using the local-density approximation and self-interaction and relaxation-corrected pseudopotentials. *Physical Review B*, 61(12):R7846, 2000.
- [49] Robert D Shannon. Revised effective ionic radii and systematic studies of interatomic distances in halides and chalcogenides. *Acta crystallographica section A: crystal physics, diffraction, theoretical and general crystallography*, 32(5):751–767, 1976.
- [50] KL Chopra, S Major, and DK Pandya. Transparent conductors—a status review. *Thin solid films*, 102(1):1–46, 1983.
- [51] F Simonis, M Van Der Leij, and CJ Hoogendoorn. Solar energy mater. 1, 221 (1979). *CrossRef—CAS— Web of Science® Times Cited*, 36.



- [52] Roy G Gordon. Method of depositing electrically conductive, infra-red reflective, transparent coatings of stannic oxide, March 27 1979. US Patent 4,146,657.
- [53] J.L.G. Fierro. *Metal Oxides: Chemistry and Applications*. Chemical Industries. CRC Press, 2005.
- [54] Chennupati Jagadish and Stephen J Pearton. *Zinc oxide bulk, thin films and nanostructures: processing, properties, and applications*. Elsevier, 2011.
- [55] Norbert H Nickel and Evgenii Terukov. *Zinc Oxide-A Material for Micro-and Optoelectronic Applications: Proceedings of the NATO Advanced Research Workshop on Zinc Oxide as a Material for Micro-and Optoelectronic Applications, held in St. Petersburg, Russia, from 23 to 25 June 2004*, volume 194. Springer Science & Business Media, 2006.
- [56] David C Look, Joseph W Hemsley, and JR Sizelove. Residual native shallow donor in ZnO. *Physical review letters*, 82(12):2552, 1999.
- [57] A. Mang, K. Reimann, and S. Rübenacke. Band gaps, crystal-field splitting, spin-orbit coupling, and exciton binding energies in ZnO under hydrostatic pressure. *Solid State Communications*, 94:251–254, April 1995.
- [58] PD.G. Thomas. The exciton spectrum of zinc oxide. *Journal of Physics and Chemistry of Solids*, 15(1):86 – 96, 1960.
- [59] D. C. Reynolds, D. C. Look, and B. Jogai. Optically pumped ultraviolet lasing from ZnO. *Solid State Communications*, 99:873–875, September 1996.
- [60] A Mang, K Reimann, et al. Band gaps, crystal-field splitting, spin-orbit coupling, and exciton binding energies in ZnO under hydrostatic pressure. *Solid state communications*, 94(4):251–254, 1995.
- [61] H. Nanto, H. Sokooshi, and T. Usuda. Smell sensor using zinc oxide thin films prepared by magnetron sputtering. In *TRANSDUCERS '91: 1991 International Conference on Solid-State Sensors and Actuators. Digest of Technical Papers*, pages 596–599, June 1991.
- [62] Anderson Janotti and Chris G Van de Walle. Oxygen vacancies in ZnO. *Applied Physics Letters*, 87(12):122102, 2005.
- [63] Eun-Cheol Lee and K. J. Chang. Possible *p*-type doping with group-I elements in ZnO. *Phys. Rev. B*, 70:115210, Sep 2004.

- [64] M Labeau, P Rey, JL Deschanvres, JC Joubert, and G Delabouglise. Thin films of high-resistivity zinc oxide produced by a modified cvd method. *Thin Solid Films*, 213(1):94–98, 1992.
- [65] Anderson Janotti and Chris G Van de Walle. Fundamentals of zinc oxide as a semiconductor. *Reports on progress in physics*, 72(12):126501, 2009.
- [66] JC Simpson and James F Cordaro. Characterization of deep levels in zinc oxide. *Journal of Applied Physics*, 63(5):1781–1783, 1988.
- [67] Sol E Harrison. Conductivity and Hall effect of ZnO at low temperatures. *Physical Review*, 93(1):52, 1954.
- [68] F. Tuomisto, K. Saarinen, D. C. Look, and G. C. Farlow. Introduction and recovery of point defects in electron-irradiated ZnO. *Phys. Rev. B*, 72:085206, Aug 2005.
- [69] S. B. Zhang, S.-H. Wei, and Alex Zunger. Intrinsic n-type versus p-type doping asymmetry and the defect physics of ZnO. *Phys. Rev. B*, 63:075205, Jan 2001.
- [70] Jianhua Hu and Roy G Gordon. Textured aluminum-doped zinc oxide thin films from atmospheric pressure chemical-vapor deposition. *Journal of Applied Physics*, 71(2):880–890, 1992.
- [71] Chris G. Van de Walle. Hydrogen as a cause of doping in zinc oxide. *Phys. Rev. Lett.*, 85:1012–1015, Jul 2000.
- [72] Anderson Janotti and Chris G Van de Walle. Hydrogen multicentre bonds. *Nature materials*, 6(1):44, 2007.
- [73] Resistivity theory. <https://www.mdc-europe.com/resistivity-theory-and-data-correction-coefficients-depen>  
Accessed: 2019-03-15.
- [74] DW Zeng, CS Xie, BL Zhu, R Jiang, X Chen, WL Song, JB Wang, and J Shi. Controlled growth of zno nanomaterials via doping sb. *Journal of Crystal Growth*, 266(4):511–518, 2004.
- [75] Ali Reza Razeghizadeh, Lila Zalaghi, Iraj Kazeminezhad, and Vahdat Rafee. Effects of sol concentration on the structural and optical properties of SnO<sub>2</sub> nanoparticle. *arXiv preprint arXiv:1502.00219*, 2015.
- [76] Suvra Sarkar and Sougata Patra. Optical characterization of tin oxide thin films synthesized by DC sputtering. *Transactions of the Indian Institute of Metals*, 61(2-3):207–209, 2008.

- [77] A El Manouni, FJ Manjón, M Mollar, B Marí, R Gómez, MC López, and JR Ramos-Barrado. Effect of aluminium doping on zinc oxide thin films grown by spray pyrolysis. *Superlattices and Microstructures*, 39(1-4):185–192, 2006.
- [78] Benny Joseph, PK Manoj, and VK Vaidyan. Studies on preparation and characterization of indium doped zinc oxide films by chemical spray deposition. *Bulletin of Materials Science*, 28(5):487–493, 2005.
- [79] K Krunk, O Bijakina, V Mikli, T Varema, and E Mellikov. Zinc oxide thin films by spray pyrolysis method. *Physica Scripta*, 1999(T79):209, 1999.
- [80] Rodrigo F Silva and Maria ED Zaniquelli. Aluminium-doped zinc oxide films prepared by an inorganic sol-gel route. *Thin Solid Films*, 449(1-2):86–93, 2004.
- [81] Masashi Ohyama, Hiromitsu Kozuka, and Toshinobu Yoko. Sol-gel preparation of transparent and conductive aluminum-doped zinc oxide films with highly preferential crystal orientation. *Journal of the American Ceramic Society*, 81(6):1622–1632, 1998.
- [82] Rina Pandey, Shavkat Yuldashev, Hai Dong Nguyen, Hee Chang Jeon, and Tae Won Kang. Fabrication of aluminium doped zinc oxide (AZO) transparent conductive oxide by ultrasonic spray pyrolysis. *Current Applied Physics*, 12:S56–S58, 2012.
- [83] AF Aktaruzzaman, GL Sharma, and LK Malhotra. Electrical, optical and annealing characteristics of ZnO: Al films prepared by spray pyrolysis. *Thin solid films*, 198(1-2):67–74, 1991.